UNIVERSIDADE ESTADUAL DE CAMPINAS
Faculdade de Engenharia Elétrica e de Computação

João Pedro Aguiar dos Santos

Dynamics of solvated ions in supercapacitor electrodes under compression and low temperature conditions

Dinâmica de íons solvatados em eletrodos de supercapacitores sob compressão e condições de baixa temperatura

Campinas

2022

João Pedro Aguiar dos Santos

Dynamics of solvated ions in supercapacitor electrodes under compression and low temperature conditions

Dinâmica de íons solvatados em eletrodos de supercapacitores sob compressão e condições de baixa temperatura

Dissertation presented to the School of Electrical and Computer Engineering of the University of Campinas in partial fulfillment of the requirements for the degree of Master in Electrical Engineering, in the area of Electronics, Microelectronics and Optoelectronics.

Dissertação apresentada à Faculdade de Engenharia Elétrica e de Computação da Universidade Estadual de Campinas como parte dos requisitos exigidos para a obtenção do título de Mestre em Engenharia Elétrica, na Área de Eletrônica, Microeletrônica e Optoeletrônica.

Supervisor: Prof. Dr. Cesar José Bonjuani Pagan

Este trabalho corresponde à versão final da dissertação defendida pelo aluno João Pedro Aguiar dos Santos, e orientada pelo Prof. Dr. Cesar José Bonjuani Pagan.

Campinas

2022

Ficha catalográfica
Universidade Estadual de Campinas
Biblioteca da Área de Engenharia e Arquitetura
Rose Meire da Silva - CRB 8/5974

Sa59d

Santos, João Pedro Aguiar dos, 1995-
Dynamics of solvated ions in supercapacitor electrodes under compression and low temperature conditions / João Pedro Aguiar dos Santos. – Campinas, SP : [s.n.], 2022.

Orientador: Cesar José Bonjuani Pagan.
Dissertação (mestrado) – Universidade Estadual de Campinas, Faculdade de Engenharia Elétrica e de Computação.

1. Energia - Armazenamento. 2. Supercapacitores. 3. Dupla camada elétrica. 4. Caracterização eletroquímica. 5. Eletrodos de carbono. I. Pagan, Cesar José Bonjuani, 1962-. II. Universidade Estadual de Campinas. Faculdade de Engenharia Elétrica e de Computação. III. Título.

Informações para Biblioteca Digital

Título em outro idioma: Dinâmica de íons solvatados em eletrodos de supercapacitores sob compressão e condições de baixa temperatura
Palavras-chave em inglês:
Energy - Storage
Supercapacitors
Electric double layer
Electrochemical characterization
Carbon Electrodes
Área de concentração: Eletrônica, Microeletrônica e Optoeletrônica
Titulação: Mestre em Engenharia Elétrica
Banca examinadora:
Cesar José Bonjuani Pagan [Orientador]
Hudson Giovani Zanin
Gustavo Doubek
Data de defesa: 28-03-2022
Programa de Pós-Graduação: Engenharia Elétrica

Identificação e informações acadêmicas do(a) aluno(a)
- ORCID do autor: https://orcid.org/0000-0002-4237-978X
- Currículo Lattes do autor: http://lattes.cnpq.br/0605457778078806

COMISSÃO JULGADORA - DISSERTAÇÃO DE MESTRADO

Candidato(a): João Pedro Aguiar dos Santos RA: 262734

Data de defesa: 28 de Março de 2022

Título da Dissertação (Inglês): "Dynamics of solvated ions in supercapacitor electrodes under compression and low temperature conditions"

Título da Dissertação (Português): "Dinâmica de íons solvatados em eletrodos de supercapacitores sob compressão e condições de baixa temperatura"

Prof. Dr. Cesar José Bonjuani Pagan (Presidente, FEEC/UNICAMP)
Prof. Dr. Hudson Giovani Zanin (FEEC/UNICAMP)
Prof. Dr. Gustavo Doubek (FEQ/UNICAMP)

A Ata de Defesa, com as respectivas assinaturas dos membros da Comissão Julgadora, encontra-se no SIGA (Sistema de Fluxo de Dissertação/Tese) e na Secretaria de Pós-Graduação da Faculdade de Engenharia Elétrica e de Computação.

To my parents, Dacelia Rodrigues Aguiar dos Santos and Raimundo Moreira dos Santos.

Acknowledgements

The acknowledgments will be written in Portuguese.

Aos meus pais, Dacelia e Raimundo, por serem meu porto seguro, pela educação, valores transmitidos e, principalmente, por sempre acreditarem no meu potencial.

Ao meu orientador Prof. Cesar Pagan pela orientação, confiança, amizade, conhecimento transmitido, por me ajudar a superar limitações pedagógicas e contribuir na minha formação como cientista. Da mesma forma eu agradeço o Prof. Hudson Zanin pela orientação, apoio, confiança, amizade e por oportunizar que eu realizasse a parte da pesquisa na BREnergies, fatores fundamentais na minha formação enquanto pesquisador.

Ao professor Leonardo de Morais da (UFVJM) pelas orientações, sugestões, correções, críticas e inestimáveis contribuições, que vão muito além do conhecimento técnico.

A todos os meus colegas da BREnergies. Sem vocês o mestrado não seria possível. A contribuição a partir de treinamentos, auxílio com a parte experimental, escrita científica, confecção de figuras, análise e interpretação de dados, sugestões, entre outros é imensurável. Assim, fica aqui meu agradecimento ao Prof. Rubens Maciel, Prof. Gustavo Doubek, Prof. Reinaldo Teofilo, Prof. Alfreds Peterlevitz, Rodolfo Fernandes, Fábio Antunes, Cássio Almeida, Francisca Oliveira, Rafael Vicentini, Manuel Pinzón, Fernando Rufino, Renato Beraldo, Bruno Freitas, Carla Real, Tharles Ribeiro, Willian Nunes, Carlos Júnior, Edson Junior, Rodrigo Costa, Lenon Costa, Erick Santos, Raissa Venâncio, Murilo Amaral, João Pedro Jenson e Syra Mubarac.

Ao pós-doutorado João Ota, pela amizade, correções, críticas, sugestões e conhecimento compartilhado.

Aos meus amigos, por sempre estarem ao meu lado, acreditarem em mim e por deixarem a vida mais leve.

À Giseli, por compartilhar a vida comigo, acreditar em mim, sempre estar do meu lado, e todo o amor.

A todos funcionários terceirizados e concursados da Unicamp que, de alguma forma, contribuiram com a minha formação.

A todos aqueles que acreditaram em mim, me apoiaram ou me ajudaram de alguma forma antes ou durante o mestrado.

À UNICAMP, à Agência Nacional do Petróleo, à Shell e ao povo brasileiro pela oportunidade e pelo suporte financeiro.

"Liberation is a praxis: the action and reflection of men and women upon their world in order to transform it."
(Paulo Freire)

"It is better to conquer yourself than to win a thousand battles. Then the victory is yours. It cannot be taken from you."
(Buddha)

"Nothing in life is to be feared; it is only to be understood."
(Marie Curie)

Abstract

Supercapacitors (SCs) are high-power energy storage devices with ultra-fast charge/discharge properties. SCs using concentrated aqueous-based electrolytes can work at low temperatures due to their intrinsic properties, such as high freezing point depression and robustness. Besides, compressing supercapacitor (SCs) electrodes is essential for minimizing ions' distance travel, faradaic reactions, overall ohmic resistance, and improving the energy storage characteristics. Studies that incorporate ion dynamics into SC electrodes under compression and low-temperature are still rare. So, the goal of the present Dissertation goal is to present the ion dynamics of different aqueous electrolytes in electrodes under compression and low-temperature to track electrochemical and structural changes under mechanical and thermal stress. The effect of temperature and compression was investigated using electrochemical, physical-chemical, structural, and Raman spectroscopy under dynamic polarization conditions. The results demonstrated that ion dynamics are affected by the compression and are driven mainly by the electrolytes features, such as ionic radii, hydrated ion size, number of water molecules in the solvation shell, and ionic conductivity. When the electrode is compressed until the micropores match in dimensions with the electrolyte's hydrated ion sizes, the formation of a superionic state is induced, increasing the capacitance by more than 160%. In addition, the Working Voltage Window (V) increased $\sim$ 50%, while the specific capacitance (C) decreased $\sim$ 20% when the temperature was reduced from 298 to 263 K. As a result, the specific energy ($\mathrm{E} = CV^2/2$) increased $\sim$ 100%. Therefore, aqueous electrolytes at low-temperature conditions and controlled electrode compression are promising candidates to improve the energy-storage characteristics in SCs.

Keywords: Compression, Low-temperature charge-storage, Pore size distribution, Ion dynamics, Supercapacitors.

Resumo

SCs são dispositivos de armazenamento de energia de alta potência com características de carga/descarga ultrarrápida. SCs com eletrólitos de base aquosa de alta concentração podem funcionar em baixas temperaturas devido às suas propriedades intrínsecas, como alto ponto de congelamento e robustez. Além disso, a compressão de eletrodos de SCs é essencial para minimizar o deslocamento dos íons, reações faradaicas, resistência ôhmica geral, e melhorar as características de armazenamento de energia. Estudos que abordam a dinâmica de íons em eletrodos de SCs sob compressão e baixa temperatura ainda são raras. Assim, o objetivo da dissertação é apresentar a dinâmica iônica de diferentes eletrólitos em eletrodos sob compressão e baixa temperatura para identificar mudanças eletroquímicas e estruturais sob estresse mecânico e térmico. O efeito de temperatura e compressão foi investigada usando métodos eletroquímicos, físico-químicos, estruturais e de espectroscopia Raman sob condições de polarização. Os resultados demonstraram que a dinâmica iônica é afetada pela compressão e são impulsionados principalmente pelas características do eletrólito, como o raio iônico, tamanho do íon, número de moléculas de água na camada de solvatação e condutividade iônica. Quando o eletrodo é comprimido até que os microporos tenham as mesmas dimensões dos íons hidratados do eletrólito, a formação de um estado superiônico é induzida, aumentando a capacitância em mais de 160%. Além disso, a tensão máxima da célula (V) aumentou $\sim$ 50%, enquanto a capacitância específica (C) diminuiu $\sim$ 20% quando a temperatura foi reduzida de 25°C para -10°C. Como resultado, a energia específica (E = $CV^2/2$) aumentou $\sim$ 100%. Portanto, eletrólitos aquosos em condições de baixa temperatura e eletrodos sob compressão controlada são candidatos promissores para melhorar as características de armazenamento de energia em SCs.

Palavras-chaves: Compressão, Armazenamento de carga em baixa temperatura, Distribuição do tamanho dos poros, Dinâmica iônica, Supercapacitores.

List of Figures

List of Tables

List of Acronyms

AC	Activated Carbon
ADC	Analog-to-Digital Converter
AVV	Anodic Vertex Voltage
BET	Brunauer-Emmett-Teller
BKP	Buckypaper
CA	Chronoamperometry
CNLS	Complex Nonlinear Squares
CPE	Constant Phase Element
CV	Cyclic Voltammetry
DAC	Digital-to-Analog Converter
EDL	Electric Double-Layer
EDLC	Electric Double-Layer Capacitor
EDR	Equivalent Distributed Resistance
EIS	Electrochemical Impedance Spectroscopy
ESR	Equivalent Series Resistance
FPD	Freezing-Point Depression
FWHM	Full Width at Half Maximum
GCD	Galvanostatic Charge/Discharge
HF	High Frequencies
LF	Low Frequencies
MPT	Maximum Power Transfer
MSE	Maximum Specific Energy
MWCNT	Multiwalled Carbon Nanotube
NMP	N-Methyl-2-Pyrrolidone
PMC	Point of Maximum Capacitance
PSC	Pseudocapacitor
PVDF	Polyvinylidene Fluoride
RCT	Charge Transfer Resistance
SC	Supercapacitor
SEM	Scanning Electron Microscope
SNR	Signal-to-Noise Ratio
SPSC	Single Potential Step Chronoamperometry
TST	Transition State Theory
WISE	Water-in-Salt Electrolyte

WVW	Working Voltage Window

List of Symbols

$E(t)$	Steady-State Voltage
E_0	Electrical Perturbation of Small Magnitude
R_{ct}	Charge Transfer Resistance
S_{Wrange}	Sweep Range
$Z_{(\omega)}$	Transfer Function of the System
ΔV_{drop}	Abrupt Change in the Voltage
ΔV	Constant Voltage
Δt	Total Discharge Time
Ω	Electrical Resistance Unit
α	Asymmetry Factor
β_{ref}	Reference Variable
η_s	Surface Overpotential
γ	Time Constant
μ_q	Expected Value
ν	Potential Scan Rate
ω	Angular Frequency
σ	Standard Variation
$\triangle U$	Working Voltage Window
f	Frequency
f_{high}	Highest Frequency
f_{low}	Lowest Frequency
i	Electric Current
m	Mass of the Active Electrode material
nb	Resolution in Bits
v_1	Inferior Potential Window
v_2	Superior Potential Window
-Z_{img}	Imaginary Impedance
Z_{cpe}	Impedance of the Constant Phase Element
A_s	Superficial Area
B_2	Electrophoretic Coefficient
C_{ads}	Adsorption Pseudocapacitance
C_{edl}	Electric Double Layer Capacitance
D	Coefficient of Diffusion
F	Faraday's Constant

$I_{0(a)}$	Anodic Exchange Current
$I_{0(b)}$	Cathodic Exchange Current
I_0	Initial Current
I_c	Capacitive Current
I_f	Faradaic Current
R_{edr}	Equivalente Distributed Resistance
R_{esr}	Equivalente Series Resistance
R_l	Charge Transfer Resistance
$U_{0(oer)}$	Potential of Oxygen Evolution reaction
U_{sc}	Voltage on the Supercapacitor
ΔG^o	Gibbs Energy of Activation
Λ	Molar Conductivity
Λ^0	Standard Water Conductivity
α_a	Anodic Charge-Transfer Coefficient
α_b	Cathodic charge-transfer coefficient
δV	Maximum Constant Voltage
η	Molar Viscosity
η^0	Standard Water Viscosity
τ_0	Relaxation Time Constant
$\triangle U$	Voltage Window Minus the Drop Potential
$\triangle U_{edr}$	Drop voltage from Distributed Resistance
$\triangle U_{esr}$	Drop voltage from Series Resistance
$\triangle t$	Interval of Time
φ	Phase Angle
a	Mean Ionic Diameter
g_w	Molal Osmotic Coefficient
i_{edl}	Current from Electric Double Layer
i_f	Redox Current
i_{self}	Self-discharge Current
k	Debye-Hückel Reciprocal Length
$q(\nu)$	Voltammetry Charge
$q_{capacitive}$	Capacitive Charge Storage
q_{in}	Charge of Ions aAdsorption
q_{out}	Charge Stored on the Outer Surface
C	Capacitance
C_{spec}	Specific Capacitance
E_{spec}	Specific Energy
I	Constant Discharge Current

P	Maximum Power Delivered
Rs	System's Resistance
T	Absolute Temperature
V	Maximum Constant Voltage
Y_0	Admittance of the Constant Phase Element
A	Arrenhius's Pre-Exponential Coefficient
R	Universal Gas Constant
k	Rate Constant
f_0	Frequency Referring to a Phase Angle of 45°
m_e	Active Mass of the Electrode
n	Parameter of the Constant Phase Element
C_{dl}	Capacitance of the Electric Double-Layer

Contents

1 Introduction

There has been a long-standing interest in energy storage systems since the eighteenth when the use o Leyden jars appeared as one of the first sources of energy storage [1]. Today, SCs are state-of-the-art energy storage. In this sense, the Brazilian Renewable Energy Solutions group (i.e., where this dissertation was done) has published a series of essential works concerning the field of SC [2–29] and the field of batteries [30, 31].

In fact, SC plays a vital function because it can storage reasonable specific energy, quickly provide high specific power and higher Freezing-Point Depression (FPD) [32–36]. Beyond that, the ionic adsorption and desorption of SCs have features that can provide a long life span of more than one million of charge/discharge cycles [37]. These excellent performances make the SC perfect for many applications that work at freezing environmental conditions and do not require substantial energy densities [35, 36, 38].

In contrast, batteries can store huge energy densities but are limited concerning specific power, cyclability, and working temperature. So, to work around these limitations, SCs have been used to complement battery storage systems, turning the equipaments more robust, capable of affording high power, high energy, and providing energy to applications below zero degrees Celsius [39–41].

Previous work has been limited in addressing the dynamics of solvated ions in SC electrodes under compression and low-temperature conditions [42–53]. So, several questions about the application of SCs in compressed and low-temperature environments remain open in the literature. As a result, the application of SCs in freezing temperatures, for example, in deep seawater submarines or arctic research centers, is still not very well explored in the energy storage field due to the lack of studies on the subject.

This study aims to evaluate how low-temperature and compressed electrodes conditions affect the electrochemical and physical-chemical measurements of the SCs. In addition, the Dissertation is divided into for general goals to achieve comprehensive information about the effects of temperature and compression in SCs. In this way, the first general goal (Chapter 2) describes fundamental concepts to master instrumentation measurements. This chapter aims to provide peace of knowledge about sources of uncertainty, error propagation, and fundamental electronic notions to help those not familiar with electrical and electronic concepts.

The second general goal (Chapter 3) describes in a review structure the effect of the experimental setup and data acquisition parameters on the quality and reliability of electrochemical measurements for SCs. This chapter seeks to provide a comprehensive study about how to master electrochemical experiments concerning SCs to avoid errors in the measurements. So, Chapters 2 and 3 have an educational function in the dissertation to prepare those readers inexperienced with electrochemical experiments and electronic concepts mainly because the energy storage field is a multidisciplinary field composed of researchers in different areas such as chemistry, physics, and engineering. Besides, Chapter 3 is fundamental for providing peace of knowledge about SCs techniques measurements to ensure more robust and reliable results in Chapter 4 and 5.

Studies about ion dynamics into different pore size distributions in SC electrodes under compression are still rare. So, the second general goal concerns evaluating the ion dynamics of five aqueous electrolytes in electrodes under compression (Chapter 4). In this way, it is possible to acquire information about the adsorption/desorption of ions in pore electrodes under compression to manufacture SCs more optimally for high compression applications. The last general goal (Chapter 5) is to evaluate charge-storage capabilities and physicochemical properties of SCs under low-temperature conditions ($T < 0°C$) using mesoporous carbon-based electrodes and concentrated aqueous-based electrolytes.

Chapter 5 predicts that compression and temperature are highly associated with parameters such as capacitance, Equivalent Series Resistance (ESR), Equivalent Distributed Resistance (EDR), power density, energy density, Working Voltage Window (WVW), the pore size distribution of the electrode, and conductivity/viscosity of the electrolyte. The capacitance and ESR are modified according to the compression applied, with a point of maximum capacitance achieved at an ideal compression level. In addition, it is presented the possibility of increasing the working voltage windows at low temperatures due to a superior free energy required to promote water-splitting. So, an SC at low temperature and controlled compression conditions could improve the energy density of the SC due to an increase in capacitance and WVW.

To test the hypothesis presented above, series of electrochemical, physicochemical, morphological, and Raman spectroscopy analyses are performed to shed light on the vital SC features influenced by the temperature and compression. Moreover, a detailed introduction of each chapter is presented in the following subsections containing the specific goals and results of the general goals discussed above.

1.1 Electrochemical Instrumentation and Misled Configuration of Supercapacitors

There has been a long-standing interest in energy storage devices [54,55] as they play a fundamental role in transportation electrification, which may become a potential key factor in reducing emissions of greenhouse gases to minimize global climate change [38]. Nevertheless, Energy Storage is a complex and multidisciplinary field [32] and, as a result, it requires the knowledge of different areas such as physics, chemistry, microelectronics, materials sciences, among others [56], especially when concerning experimental verification and practical studies. Such multidisciplinary and experimental research field requires reasonable know-how on areas that are outside the specialty of the researcher.

One example is a bachelor's in chemistry who needs to understand concepts on electronic engineering before performing electrochemical analysis by the means of a potentiostat. Nowadays, innovative studies in higher education that include the proposal of approaches in learning and teaching including multidisciplinary aspects in present educational processes can be widely found. However, a complete multidisciplinary teaching, which should include complex human aspects, is still far from being a common reality [57–61]. Even in a university like Unicamp, which was created to be essentially interdisciplinary (see "O Conceito de Universidade no Projeto da UNICAMP", Fausto Castilho, ed. Unicamp, 2008, in portuguese) [62].

Concerning SCs, several review papers have received huge attention, especially those that put the bodies of knowledge from different fields together to interpret SCs phenomena and to propose a correct explanation of the results [63–72]. Nonetheless, the aforementioned works are limited for including only simple descriptions related to electrochemical measurements with minimum details on procedures for instrumentation setup. Consequently, the findings listed by the previous works become more difficult to be reproducible and correctly interpreted by researchers who have basic expertise and familiarity with electrochemical analytical measurements [73]. Moreover, the lack of information on measurement procedures may conceive some systematic errors in the experimental measurement. Non-identified systematic errors may lead to an incomplete or incorrect collection of experimental data, which could be related, in some cases, to a misleading report of research novelty or contribution.

The present Dissertation aims to describe and propose based on Chapter 2 and 3 guidelines on how to perform electrochemical measurements of SCs properly. An aqueous electrolyte-based symmetric SC with electrodes of Multiwalled Carbon Nanotubes (MWCNT) is measured and characterized by the means of a robust selection of electrochemical analytical methods for SC measurements, namely Cyclic Voltammetry (CV), Galvanostatic Charge/Discharge (GCD), Single Potential Step Chronoamperometry (SPSC), and Electrochemical Impedance Spectroscopy (EIS). The effects in experimental measurements of voltage and current range, bandwidth, sampling interval, and delay interval for each method are analyzed.

Careful analysis shows that inappropriate configuration of both hardware and software of the measurement instrument can jeopardize the integrity of measurement results. Consequently, measurements results become misleading and may not explain a feature of SC correctly, may ruin the verification of a theoretical hypothesis, or may produce distorted and biased scientific evidence. On the other hand, the Dissertation lists and explains practical solutions to mitigate the problems mentioned previously. Discussions on stochastic errors caused by electromagnetic interference, environmental conditions, and wrong intervals plots are highlighted as well.

1.2 Supercapacitors Electrodes Under Compression

Many ideas about raising energy storage have been proposed in the last decade as increasing the WVW, decorating the electrodes with composites that adding faradaic process (i.e,. the reduction or oxidation reactions of chemical substances at the electrode surface), enhancing the porous electrodes, and applying the correct assembling [56, 74–78].The last one can be improved concerning proper compression levels to ensure good electric contact between the current collector/electrode interface, which avoids interfacial impedance [63, 79–83].

Besides, the correct electrode compression can also improve the porous electrode's performance by minimizing ions' distance travel into the electrode, improving the electrode conductivity and ions' diffusion resistance to access the porous structure [45, 84–91]. On the other hand, studies of the ion dynamics into different pore size distribution in SC electrodes after applying compression are still rare, as point out by Lahrar and co-workers [92].

Several studies have shown that compressing the electrodes can improve the capacitance and ESR [42–48]. However, these works only focused on the electrochemical response without considering the pore size distribution changes after compressing the electrode. For this reason, this paper presents an ion dynamics study into different pore size distributions in supercapacitor electrodes under compression.

There are two hypotheses: *i*) the superionic state occurs only when the pore's size has approximately the ion size for ionic electrolytes. However, ionic electrolytes do not present a solvation shell; *ii*) the maximum capacitance appears due to a superionic state reached when the pore's size fits with the hydrated ion size in the case of aqueous electrolytes. These hypotheses present a new approach that combines scanning electron micrographs and nitrogen adsorption/desorption analysis to evaluate the porous electrode's structural modifications with electrochemical measures to better describes the effects of compression and the ion's dynamics into different pore size distribution in supercapacitor electrodes.

1.3 Dynamics of Supercapacitors Below Zero Degrees Celcius.

This section and Chapter 5 reproduce the published scientific paper in the Journal of Energy Chemistry (Figure 1.1), "*Boosting energy-storage capability in carbon-*

based supercapacitors using low-temperature water-in-salt electrolytes" [93]. The authors retain the right to include it in the dissertation. In addition, if a reader wants to cite the study presented in this section or Chapter 5, it is required to cite the paper published in the Journal of Energy Chemistry [93].

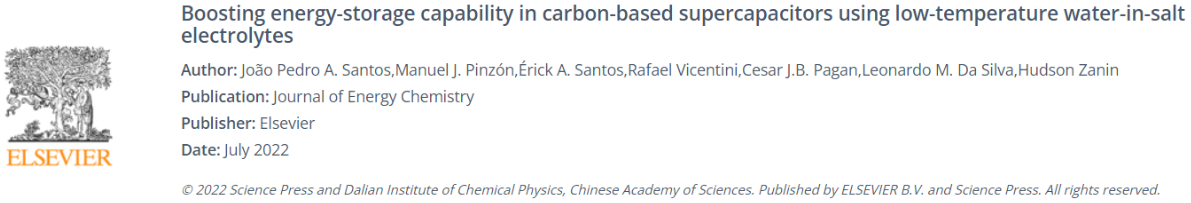

Boosting energy-storage capability in carbon-based supercapacitors using low-temperature water-in-salt electrolytes

Author: João Pedro A. Santos,Manuel J. Pinzón,Érick A. Santos,Rafael Vicentini,Cesar J.B. Pagan,Leonardo M. Da Silva,Hudson Zanin
Publication: Journal of Energy Chemistry
Publisher: Elsevier
Date: July 2022

© 2022 Science Press and Dalian Institute of Chemical Physics, Chinese Academy of Sciences. Published by ELSEVIER B.V. and Science Press. All rights reserved.

Figure 1.1 – Boosting energy-storage capability in carbon-based supercapacitors using low-temperature water-in-salt electrolytes.

Batteries and SCs are the main energy storage devices used in several technological applications. At low temperatures, batteries lose a significant part of the stored energy due to the intrinsic reduction in the charge-transfer kinetics, ionic conductivity between the electrodes, and mass-transport limitations during the surface and/or intercalation reactions [34]. On the contrary, at low-temperature (e.g., near-freezing conditions) conditions, SCs can perform much better than batteries due to the electrostatic nature of the energy storage process, the short distance separating the negative and positive electrodes, and the absence of mass transport by diffusion, (i.e., the ionic transport occurs solely by migration). Therefore, in some applications, batteries can be replaced by SCs, [32] as in the in-space avionic, astronomical observatories, high altitude aircraft, and several other electrical systems used in the polar regions [34].

Several studies have pointed out the possibility of increasing the FPD to temperatures lower than -25°C using Water-in-Salt Electrolytes (WISEs) [43, 49–53]. This approach uses highly concentrated salt solutions to decrease the number of free water molecules present in the solvent, i.e., those molecules not involved in the hydration process of the dissolved ionic species [76]. As a result, the cell voltage (V), corresponding to the electrolyte stability, can be increased (e.g., $V > 1.23$ V) since the onset of the water-splitting reaction is displaced to more positive voltages when the molal osmotic coefficient (g_w) of the solvent is strongly reduced at high ionic concentrations. Therefore, at least in principle, the use of WISEs can increase the WVW in SCs [77].

Despite these considerations, a literature survey shows that previous works have been limited to addressing the correlation between the SC typical characteristics, such as WVW, specific capacitance (C_{spec}), specific energy (E_{spec}), and equivalent series resistance (R_{esr}) at moderate freezing conditions [43, 49–53]. On the other hand, at high temperatures (e.g., $> 65°$C), it is pointed out the necessity of controlling the WVW as a function of the temperature to reduce the excessive electrolyte decomposition and the lifetime of SCs [94, 95].

From the above considerations, for the first time, this Dissertation reports the effect of using a low-temperature WISE system (e.g., $NaClO_4$ 17 mol kg^{-1} (17m)) on the overall performance of the energy storage process exhibited by a mesoporous carbon buckypaper supercapacitor in the symmetric configuration. Different electrochemical techniques and the in-situ (or operando) Raman spectroscopy under dynamic polarization conditions were used to address the main phenomena affecting the energy storage at reduced temperature. As will be seen, promising findings were obtained at reduced temperatures, as is the case of specific energy. Therefore, low-temperature WISEs are good candidates for special applications involving carbon-based SCs.

2 A Review on Electrochemical Instrumentation for Supercapacitors

Chapter 2 focuses on instrumentation topics, including hardware and software-related most common sources of errors, which must be appropriately identified to provide mitigation alternatives. Understanding instrumentation and basic electronic concepts of potentiostats to evaluate electrochemical devices' performance is fundamental to obtaining reliable experimental data. Based on that, the goal of Chapter 2 is to provide a review of electrochemistry instrumentation to help those interested in performing SCs measurements with accuracy, precision, resolution, and the correct installation to prevent random and systematic errors, as well as reinforce these concepts to improve the electrochemistry results in the following chapters. As potentiostats and SCs have specific and different features among them, all parameters need to be individually set for each situation. In this way, a unique "recipe" (i.e., use the standard configuration of the potentiostat) to perform an accurate experiment is not a reasonable approach to ensure reliable measurements. For this reason, it is seen that reviewing these concepts is fundamental to ensure reliable electrochemistry measurements, especially for the results presented in the following chapters (i.e., Chapter 3,4, and 5) of the Dissertation.

2.1 Accuracy and Precision in Electronic Instrumentation

When several measurements are done for the same quantity through any sensor, the resulting values are not the same for every measurement due to uncertainties from the measurement equipment and the equipment configuration. Furthermore, other external factors, such as mechanical vibration, temperature change, or electromagnetic noise due to other nearby electronic equipment, also induce deviations in the resulting value from the actual quantity. Usually, a sensor is characterized by its reliability, accuracy, and precision. A sensor that can detect a given quantity with low deviation is reliable. A sensor is accurate if the measured value is close to the corresponding true value. In other words, an accurate sensor shows no systematic errors. Finally, the sensor is precise when it is both reliable and accurate [96].

Figure 2.1 (a) illustrates the concepts of accuracy and precision of a measurement. Where accuracy is the closeness of the parameter measured concerning the real value and precision is the level to which a measured value presents identical results at invariable conditions [97]. Figure 2.1 (b) illustrates the concept of resolution. The resolution is the minimum variation of a quantity that a sensor can detect then produce an output signal [98,99]. As an example, in Chemistry graduated volumetric pipette can be considered a "sensor." Therefore, a 1-mL graduated volumetric pipette has a higher resolution for measuring an electrolyte of 0.5 mL than a 20-mL graduated volumetric pipette. It should be noted that resolution has no relation to the accuracy of a measurement [100].

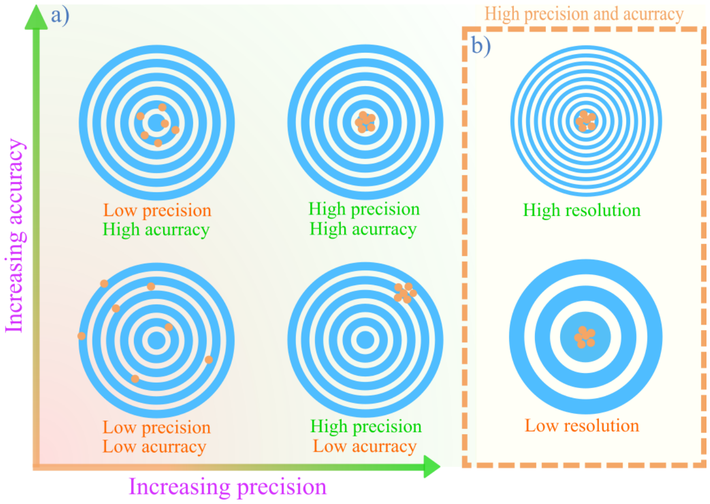

Figure 2.1 – Illustration of the concept of accuracy, precision, and resolution. (a) Accuracy and precision. (b) Resolution for a measurement with high accuracy and high precision. Figure adapted from [99].

2.2 Analog-to-Digital Converters and Resolution

A potentiostat detects voltage and current analogically. Figure 2.2 shows a simplified schematic of a potentiostat. The potentiostat is electronic equipment capable of executing a variety of measurement techniques, and it is widely used to evaluate the performance of electrochemical devices [101–104]. This basic electronic circuit is composed of a signal generator responsible for generating the user-defined perturbation signal, a signal-conditioning circuit based on a control amplifier, an electrometer for measuring electrical charging, and a current-to-voltage converter, which acquires current I_s through the device by measuring the voltage on the resistor R_{sense}. After acquiring both current and voltage, the potentiostat packs the raw data and transmits it to the computer to be processed by the potentiostat software [105].

Once that modern electrochemical equipment is digital, voltage and current detected by the potentiostat circuit in Figure 2.2 are discretized (or digitalized) periodically and stored as bits in the memory of a computer. By doing it, it is possible to perform mathematical operations with the data, store it in digital media, and transmit and share the data easily. The conversion of analog signals to digital signals (e.g., representing values of current or voltage through bits) inside the potentiostat is performed by the Analog-to-Digital Converter (ADC). When necessary, the opposite process is performed by a Digital-to-Analog Converter (DAC), which transforms a user-defined digital value

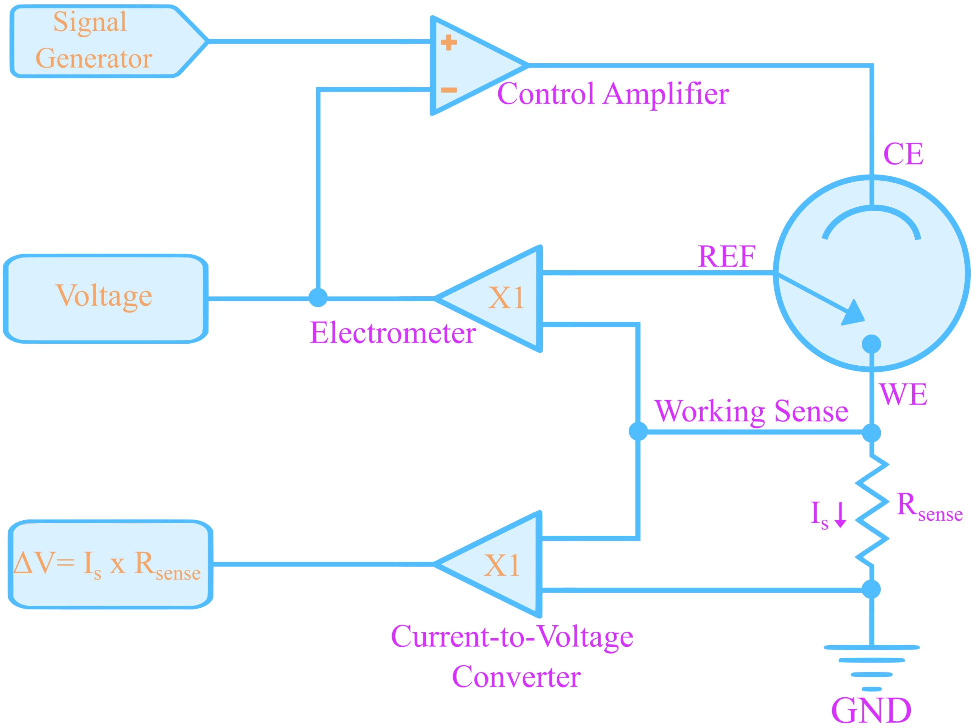

Figure 2.2 – Simplified electronic schematic of a potentiostat. Figure adapted from [105].

to an analog variable [106]. The ADC cannot convert a quantity "infinitely," therefore a resolution of its measurements can be defined by

$$Resolution = \beta_{ref} * \left(\frac{1}{2^{nb} - 1}\right), \tag{2.1}$$

where β_{ref} is the full-scale range and nb is the number of bits available to represent the measurement. For example, if the scale ranges from 0 to 100, a 10-bit measurement has $100/1023 \approx 0{,}098$ resolution. The resolution of the potentiostat is fixed (usually higher than 10 bits). Hence, users only need to configure the correct reference value (current or voltage). When a potentiostat is used to find some features of an electrochemical system, it is basically measured the voltage and current in the function of time or frequency.

So, based on these data is possible to find the behavior of a system concerning a perturbation. Otherwise, some tests require different magnitudes of current or voltage to evaluate a specific response properly (e.g., leakage current and power). Then, a potentiostat usually has several ranges of voltage and current for reading a variable at different magnitudes without losing resolution. Beyond, as the analog signal is continuous in time, it is necessary to convert it into a specific interval to have a reliable representation. This rate of the measured value is called the sampling rate of the converter. According to the Nyquist–Shannon sampling theorem, to obtain a genuine reproduction of the original signal, it is necessary to sample the signal with at least twice the maximum frequency of the fundamental signal [96, 100].

For electrochemical measures of SCs, the sampling rate is fundamental to ensure proper modeling. In principle, one might imagine that high sampling rates limited to short acquisition time intervals might be the best choice. However, it is incorrect because the equipment will produce unnecessary data, making raw data manipulation difficult. So, there is also not a recipe that can be followed to produce reliable data.

2.3 Sources of Experimental Uncertainty in Electronic Scientific Equipment

From a straightforward point of view, uncertainty is the expected maximum absolute difference between the measured value and the true value. This simple definition is frequently overlooked in experimental reports dealing with state-of-the-art scientific research. Even though it may be seen as counter-intuitive, the "true value" of a measurement is actually not known yet, being a reference value from simulated results or even an approximation. Consider for instance the execution of a EIS for a novel supercapacitor under study. After the experiment is performed and the parametric fitting is done, the obtained results could be benchmarked to existing experimental literature.

Systematic errors affect the accuracy of a measurement, resulting in measurements that divert from the true value consistently. In other words, systematic errors yield measurements different from the true value by the same amount, contributing to the total uncertainty. Systematic errors may be a function of experimental parameters and conditions. As the potentiostat is central scientific equipment for performance characterization of SCs, one should be especially concerned with its periodic calibration. In fact, lack of proper calibration may be responsible for errors in several measurements even along the SC preparation and assembly, such as in analytical weight scales used for mass measurements of electrodes and electrolytes. The measurements are later used to calculate specific energy (W h kg^{-1}), specific power (W kg^{-1}) and the establishment of gravimetric current (A g^{-1}) for performance assessment of the SC.

Random errors, on the other hand, can be addressed by replicating a measurement and performing mathematical operations on the collected data, such as simple averaging or more specific methods, so that the presence of random errors becomes unlikely or negligible. This occurs because random errors are caused mainly by chance, slight fluctuations in environmental conditions, and instrument conditions or installation, appearing not consecutively or consistently. It is in the best interest of researchers and laboratory staff to keep error sources under control and very well-known.

It is in the best interest of researchers and laboratory staff to keep error sources under control and very well-known. Following is a list of non-obvious systematic or random error sources in electronic scientific equipment.

2.3.1 Temperature Fluctuations

Temperature fluctuations on the sample under test occur due to poor temperature control of the test room or because the sample (supercapacitor, for instance) generates heat not properly dissipated to the surrounding medium. This is not uncommon in current- or power-intensive experiments with neither stable nor controlled temperature conditions. In such a situation, the environmental temperature rise may lead to an increase in the overall temperature of the sample, which may change the supercapacitor equivalent electrical resistance (usually decreasing it, as the temperature coefficient is typically negative). For low-power experiments, such as the evaluation of self-discharge current, generally, temperature affects the discharge rate, so error propagation may be large since experiment duration is very long (hundreds and thousands of hours).

Temperature also causes variations of open circuit voltage, which are hard to be quantified if the increase of thermal energy is not accounted during the experiment properly. In this case, it is necessary to determine the entropy coefficient (mV/K) of the under-test supercapacitor previously as a function of state-of-charge and to control and monitor room/chamber temperature tightly so that temperature variation can be analyzed after the experiment correctly. Finally, one must be aware of the temperature sensor's calibration (precision and resolution) by choosing the adequate sensing technology (e.g., thermocouple, negative/positive temperature thermistors).

2.3.2 Equipment Installation

Unexpected results can be produced by electromagnetic fields created by electronic equipment nearby the electrochemical cell and the potentiostat or connected to the same electrical mains. The disturbance may reach the potentiostat either by radiated or conducted electromagnetic noise [107, 108].

Radiated Electromagnetic noises are likely to be produced by nearby equipment operating above 30 MHz, such as electronic lamps and other circuits with inverters. The radiated noise has a very large frequency bandwidth, which increases the chance of coupling with ongoing experiments. Fluorescent lamps and switched-mode power supplies may also produce enough radiated disturbance to be noticeable in a potentiostat, although it is usually in a narrower frequency range and intensity.

To minimize the effects of radiated electromagnetic noises is recommended: (*i*) to install and to position the potentiostat and the electrochemical cell far from potential sources of radiated electromagnetic noise; (*ii*) to avoid unshielded electrical cables for connection of electrochemical cells [73]; and (*iii*) to insert the electrochemical cell within a faraday cage to avoid effects by the electromagnetic fields produced by the potentiostat itself, especially in low current experiments. These cares must be taken mainly in ultra-low voltage and current experiments because the measurements are significantly affected by background noise. The Signal-to-Noise Ratio (SNR) of measurements is expressed as SNR $= (\mu_q \ / \ \sigma)$ where μ_q is the expected value and σ the standard variation of the noise. SNR should be evaluated before preparing the experiment.

Conducted Electromagnetic noises may cause interferences in measurement equipment or in the sample under test by the mean of the conductors connected to the electrical mains. Switched-mode power sources with low power factor in equipment or tools, such as lamps and motor drivers, may produce harmonic-distorted currents, which contaminate the electrical mains voltage that feed the potentiostat. The eventual presence of distorted electrical mains voltage may lead to a poor-quality waveform during a frequency sweep performed in a EIS experiment, for instance. Although theoretically possible, filtering the distortion from experimental results is a too complex task since the potentiostat is not supposed to estimate the possible frequencies of the electrical mains voltage. Significant measurement errors may result from delays in signal propagation, couplings, current loop, signal reflections, common mode current, high-frequency harmonics, and so on [107, 108]. Whenever possible, it is important to add line filters between the equipment and the electrical mains and to avoid plugging other equipment to the same outlet or circuit to which the potentiostat is connected [73].

Finally, characteristics of an electrochemical device, such as SC, are highly dependent on its initial state of charge. So, it is fundamental to define and to know the initial state of the SC. Experiments, such as CV, SPSC, GCD, or EIS, unveil different profiles of a device for different initial voltages. For these experiments, the initial state must always be defined as fully discharged (i.e., no voltage in the terminals of the device) for proper measurement of the SC features. So, a routine procedure is necessary to assure the complete discharge of the device between the measurements, so the initial state is the same for all measurements. For example, the initial voltage in the SPSC experiment drives the maximum current and the final current over some time, so any residual voltage at the beginning of the procedure modifies the response.

2.4 Error propagation in electrochemical measurements

As previously discussed by Da Silva et al., using different electrochemical methods to characterize SCs can significantly affect the definition of specific capacitance, ESR, and energy density [32].

1. In the CV case, the integral method applied to determine the specific capacitance can be affected by changes in the CV profile caused by the ESR. For example, different scan rates change the number of electrolyte ions adsorbed in the micropores,

affecting the formation of the electric double layer and consequently the capacitance measured.

2. In the EIS case, in the existence of frequency dispersion and distributed capacitance effects, there is no way to determine only one capacitance value. Also, inadequate equivalent circuits are constantly used, leading to erroneous conclusions. It can be seen when a porous behavior related to a phase angle close to 45º is interpreted as a Warburg element [32].

3. In the GCD case, a common mistake occurs because slight deviations from the ideal triangular profile cause several errors in the specific capacitance calculus. For instance, when a battery-like behavior is seen on the profile, a simple algebraic equation can no longer accurately determine the specific capacitance. In this case, to avoid misinterpretation on the energy and power density calculus, a new approach must be used to find the energy storage and dissipated based on the irregular curves of the GCD.

Besides, the calculus of some important SCs parameters in the area of material science is strongly dependent on the weight as specific capacitance, energy, and power densities (i.e., F g^{-1}, Wh kg^{-1}, and W kg^{-1}, respectively). Some researchers use the weight per active material (e.g., carbon-based materials, metal-oxides), especially when it is necessary to determine the materials' features. In contrast, researchers from engineering applications use the whole weight of the cell (i.e., current collectors, electrolyte, separator, binder, connectors, and packaging) and carbon-based materials to evaluate the application of the energy storage device as a whole and not just the material used. Both are correct, but the way it is done needs to be very well described in the methods, and the authors need to understand when it is correct using each method.

A common mistake found in the literature concerning SCs is the lack of information concerning how the normalization of SCs is done. Sometimes, high values of energy and power densities in the materials field are seen in research papers as a novelty. However, if it is not investigated well, good results are seen only due to an error in data normalization. For example, in the materials field, if the mass of metal-oxide material used to decorate electrodes of pseudocapacitors is the only mass considered to calculate the energy density instead of considering the mass of the carbon-based electrodes plus the metal-oxide material and error of normalization will be present. This error in the materials field can overestimate the energy and power densities by a factor higher than four, especially when only a thin film of metal-oxide material is added to a vast mass of activated carbon.

2.5 Concluding Remarks

Testing energy storage devices may sound like an easy task. However, it involves essential electronic concepts that must be known, so the characterization process unveils precise and reliable measurements. Electrochemistry measurement of SCs is not an easy task, predominantly when those engaging in the topic are not familiar with electric/electronic engineering concepts as conducted/radiated electromagnetic, ADC or resolution. So, this chapter provides accessible and referred instructions for beginner-level users of such instrumentation to perform SCs reliable measurements. Based on concepts such as accuracy, precision, resolution, and the proper understanding of electromagnetic effects to prevent random and systematic errors. Furthermore, the concepts described in this chapter are fundamental for providing a robust strategy to turn the results seen in the following chapters robust and trustworthy.

3 How the Measurements of Supercapacitors are Affected by Misled Configuration of Electrochemical Equipments

The present chapter discusses important aspects of experimental characterization of SCs through a series of well-known electrochemical methods. It is noted that numerous published papers claim discoveries concealing or neglecting some vital information related to the electrochemical instrumentation setting (e.g., as briefly introduced in Chapter 2) and apparatus used. The lack of such information may lead researchers, especially the inexperienced ones, to misinterpret procedures and results. Eventually, the eventual misled configuration of electrochemical equipment due to misinterpretation of measurement procedures may result in low reproducibility rates.

In this way, this chapter aims to evaluate, analyze and estimate a series of experiments, namely CV, GCD, SPSC, and EIS based on the measurement of an aqueous electrolyte-based symmetric SC with electrodes of MWCNTs at different parameters to demystify results caused by incorrect configuration. The correct understanding of these techniques and how to set them properly is fundamental to equalize the contributions in the field and ensure reliable results in Chapters 4 and 5, leading to a more consistent evolution of the SCs.

3.1 Materials and Methods

All electrochemical results are based on symmetric SC soaked in an aqueous electrolyte (1 M of LiCl). The symmetric carbon electrodes are Buckypaper (BKP) composed of MWCNTs model Ctube-120 from (CNT Co., Ltd., South Korea). The BKP electrode preparation process had been presented in detail elsewhere [109]. In brief, a suspension containing MWCNTs and sodium dodecyl sulfate (Sigma-Aldrich, CAS-No: 151-21-3) (1:10 wt.%) was dispersed in deionized water and ultrasonicated for 30 min. After, the suspension was filtered with a controllable volumetric flow rate to produce a wafer [109]. Finally, to obtain the BKP electrodes, the wafer was washed, vacuum dried for 3 hours, and cut to 10 mm in diameter. In Figure A.1, it is possible to see the morphological structure of the MWCNTs electrodes. In addition, Figure A.2 has presented the nitrogen adsorption/desorption isotherms for MWCNT.

Electrochemical experiments were carried out with symmetrical two-electrode system using a standard CR2032 coin cell containing the BKP electrodes separated by a membrane soaked with 1 M LiCl as electrolyte. Figure 3.1 (a-c) presents a schematic representation of this system. The electrochemical techniques applied were CV, GCD, EIS, and SPSC. All measures were performed using a model SP-200 potentiostat from Biologic. The CV was done at different scan rates (1 to 500 mV s^{-1}). EIS was conducted in the range of 100 kHz to 10 mHz. GCD was executed at gravimetric currents in the 0.125 to 32 A g^{-1} interval. Finally, SPSC was set for a single potential step of 2 min.

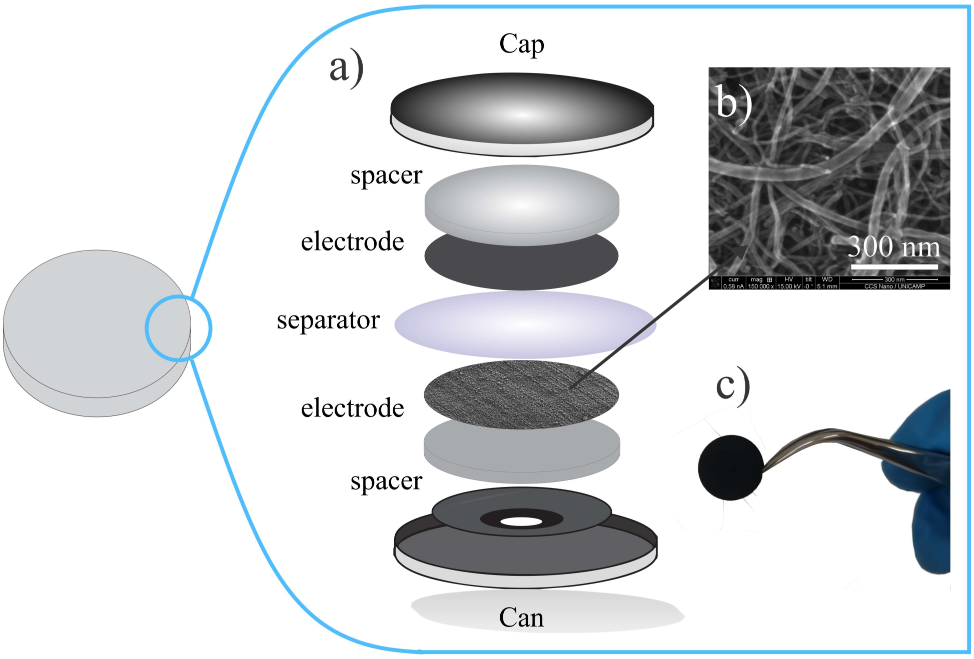

Figure 3.1 – (a) Schematic representation of the CR2032 coin cell used in the electrochemical analyses. (b and c) The BKP electrodes of MWCNT.

The maximum working voltage windows were set at 1.2 V for all techniques due to their electrochemical instabilities at higher electrical potentials. The other parameters modified to perform the measures are discussed in the results. The SC is discharged every measurement cycle to force a constant initial state. Then, SPSC routines at zero volts were done between all the experiments for two minutes to discharge the SC completely (i.e., discharge the SC). So, all the measures are presented concerning a non-charged initial state.

Here in this chapter, all figures are not normalized by the device's mass to facilitate the identification of the correct configuration parameters (i.e., range of current). It is not usually done in the scientific community. However, in this study, it is done as an instructive, pedagogical strategy to facilitate comprehension. Furthermore, to avoid misinterpretation of data caused by drastic changes seen at the first cycles, the devices were cycled ten thousand times before the experiments presented in the results.

3.1.1 Cyclic Voltammetry

CV is a versatile and well-established method in electrochemistry that supports the investigation of the electron transfer process in electrochemical systems [110]. Concerning SCs, the CV is a robust quantitative and pseudo quantitative technique that allows determining ion dynamics processes in the electrode/electrolyte interface, capacitance, correct WVW, and faradaic reactions. The CV is performed by applying a linear voltage while the current response is measured in a determined range of points [111]. The CV plot result provides several pieces of information about the reactivity and mass transport in function of the voltage applied. In SCs, the energy can be stored in the Electric Double-Layer (EDL) interface, the bulk of the active material (e.g., Faradaic reaction), or both [112, 113].

The CV is carried out by applying a linear controlled voltage between the reference and working electrode. This linear voltage is controlled by a defined scan rate, and as a result, the current flows from the counter electrode to the working electrode [110, 111]. Thus, based on the area of the voltammogram produced and the feature of the measure is possible to calculate the capacitance by

$$C = \frac{\int_{v_2}^{v_1} i dU}{\nu * \triangle U * m}, \tag{3.1}$$

where i is the current, v_1 and v_2 are the potential window that limits the integral, ν is the potential scan rate, $\triangle U$ is the WVW, and m is the mass of the electrode material [1].

Based on Equation (3.1), it is possible to see that the measured capacitance is highly influenced by the scan rate, especially to high scan rates. Redox processes are omitted when the scan rate is high ($\nu \rightarrow \infty$), reaming only capacitive charge storage because faradaic reactions are slower than scan rate. On the other hand, the time constant is suitable for the faradaic processes when the scan rate is nearly zero ($\nu \approx 0$). Then, it is possible to observe both process's faradaic and electrostatic at low scan rates [1].

The *quasi-rectangular* profile of current/voltage is usually found for SCs. From a theoretical point of view, the capacitive current I_c of the CV profile shown in Figure 3.2 (a) can be described by the following equation as

$$I_C = C_{EDL}\left[1 - \exp\left(\frac{-\triangle U}{R_{ESR} * C_{EDL} * \nu}\right)\right], \tag{3.2}$$

where R_{esr} is the equivalent series resistance and C_{edl} is the electric double layer capacitance.

On the other hand, when some irreversible faradaic reactions and/or battery-like reactions are occurring, the CV profile is according to the Butler-Volmer's model. For the anodic scan, the capacitive and faradaic current I_f, are described as

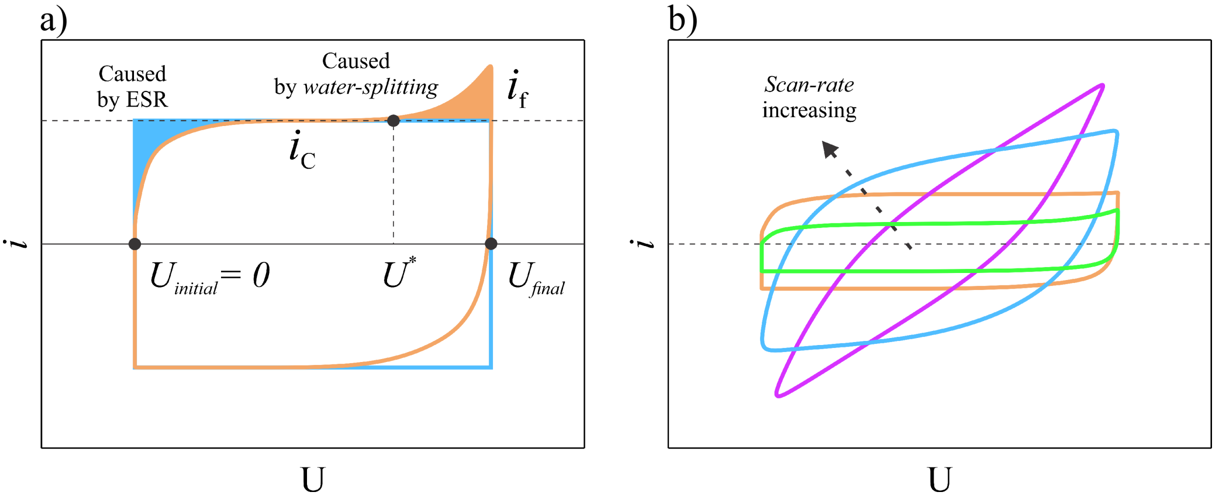

Figure 3.2 – (a) Theoretical aspects of a CV profile where the capacitive and faradaic contribution are evidenced. (b) CV with different scan-rates to evidences the differences on the shape. Figure adapted from [7].

$$I = I_C + I_F = C_{EDL} * \nu \left[1 - \exp\left(\frac{-\triangle U}{R_{ESR} * C_{EDL} * \nu}\right)\right] + I_{0(a)} \exp\left[\frac{\alpha_a F \left(U - U_{0(OER)}\right)}{RT}\right], \tag{3.3}$$

where $I_{0(a)}$ is the anodic exchange current density measured at the electric potential related to the oxygen evolution reaction $U_{0(oer)}$, α_a is the anodic charge-transfer coefficient, R is the universal gas constant, and T is the absolute temperature and F is the Faraday's constant.

For the cathodic scan, the capacitive and faradaic current of the CV profile is given as

$$-I = I_C + I_F = -C_{EDL} * \nu \left[1 - \exp\left(\frac{-\triangle U}{R_{ESR} * C_{EDL} * \nu}\right)\right] + I_{0(c)} \exp\left[\frac{\alpha_b F \left(U - U_{0(HER)}\right)}{RT}\right], \tag{3.4}$$

where $I_{0(b)}$ is the cathodic exchange current density measured at the electric potential related to the hydrogen evolution reaction $U_{0(oer)}$ and α_b is the anodic charge-transfer coefficient.

As predicted by Equation (3.2), the influence of the R_{esr} on the CV quasi-rectangular profile of SCs is evident. Likewise, with Equations (3.3) and (3.4) it can be noted that the exponential increase in anodic and/or cathodic currents is related to irreversible faradaic processes, which becomes an important tool to determine the WVW of SCs. Moreover, as these processes happen in different constants of time, it is possible to see their influence in the voltammogram applying a wide range of scan rates, as presented in Figure 3.2 (b). Concerning EDL charge mechanisms, the voltammogram will present a rectangular shape for a low scan rate, while faradaic reactions will present peaks.

The voltammetry charge $q(\nu)$ calculated by the integral of the CV profile, can be separated into two parts (q_{out} and q_{in}) for real SCs due to the faradaic (i.e., electrolyte and electrode decomposition) and EDL process. Where $q_{capacitive}$ is the capacitive charge storage processes, q_{out} is the charge stored on the outer surface of the electrode and accessed by the electrolyte, and q_{in} is the inner voltammetric charge representing the adsorption and desorption of ions on the pores, boundaries, and cracks [1]. As q_{in} is proportional to $\sqrt{\nu}$, $q(\nu)$ can be expressed as

$$q_{(\nu)} = q_{(out)} + q_{(in)} = q_{(capacitive)} + k\frac{1}{\sqrt{\nu}}. \tag{3.5}$$

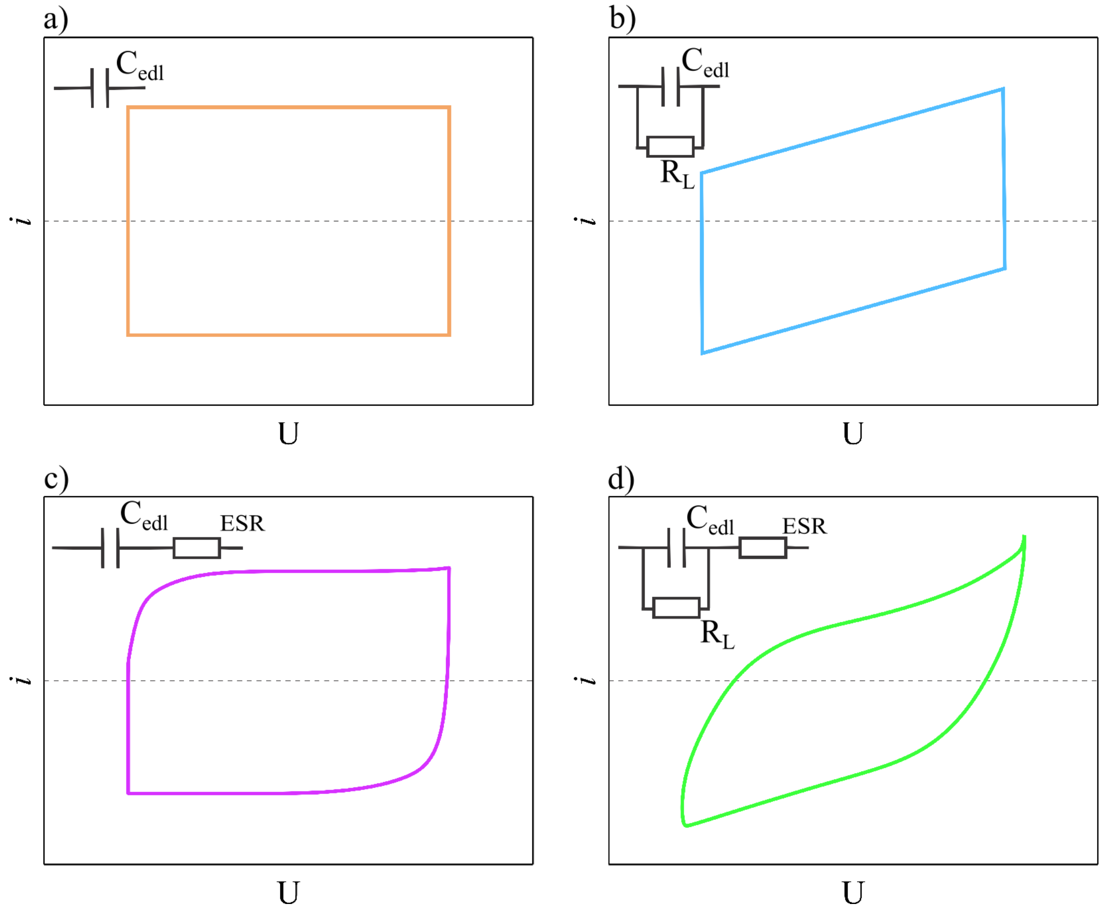

Figure 3.3 – Equivalent circuits for different CV profiles. (a) Ideal capacitive behavior, (b) inclined, (c) typical SC behavior combining C_{edl} and R_{esr}, and (d) irreversible faradaic reactions combining C_{edl}, R_l and R_{esr}. Figure adapted from [63].

As in the case of EIS data (see further discussion), it is possible to correlate de CV profile with electric circuits and their parameters. Thus, typical electric circuits and their corresponding CV are presented on the schematic in Figure 3.3. Here, based on the CV shape, Figure 3.3 (a) shows the expected ideal capacitive behavior, Figure 3.3 (b) ideal capacitive with an inclination caused by a faradaic charge transfer resistance R_l in parallel, Figure 3.3 (c) exhibits a typical SC behavior combining C_{edl} and R_{esr}, and Figure 3.3 (d) presents the irreversible faradaic reactions combining C_{edl}, R_l and R_{esr} [63].

3.1.2 Chronopotentiometry

Chronopotentiometry (CP or Galvanostatic charge/discharge, GCD, the other name for the same technic) is a transient technique that provides fundamental SC parameters such as energy storage, ESR, EDR, cyclability, rate capability, and coulombic efficiency [114–119]. The GCD analysis applies a constant current during the charges and discharges while the voltage is measured. The capacitance is constant in time and depends only on the applied potential. So, the charge and discharge profiles are linear and can be expressed by

$$U = t\frac{i}{C}, \tag{3.6}$$

where i is the current applied.

In contrast, for SCs, the response can be non-linear depending on the storage mechanisms, and this deviation is usually seen in Pseudocapacitors (PSCs) and hybrid systems [120, 121]. Besides the storage mechanisms, the GCD profile can also be driven by the current applied. At high current densities, faradaic processes are mitigated due to the insufficient constant of time for the transport of charge happening properly. So, the storage of ions in the EDL will be the majority approaching the curve to a linear plot even for PSCs. On the other hand, as in CV analysis of low scan-rate, the GCD profile will represent the sum of electrochemical processes in the device at low current density. Then, a SC will continue linear while hybrid systems and PSCs will describe a non-linear profile because the kinetic control of a single reversible reaction is not a linear voltage function [38, 55, 122].

The capacitance of the SC can be obtained with good accuracy through the GCD curve. So, for an SC that shows only charges storage on SC, the capacitance can be expressed by

$$C = \frac{i\triangle t}{\triangle U}, \tag{3.7}$$

where $\triangle t$ is the interval of time for charge (or discharge) the SC and $\triangle U$ is the corresponding voltage variation. (Note that $\triangle U$ is the result of the subtraction of the drop voltage at the beginning of the charge/discharge curve from WVW. See Figure 3.4(a)). For GCD measures that present a nonlinear plot, the capacitance needs to be found calculating the area of the discharge profile with

$$C = \frac{q}{U} = \frac{2i\int U dt}{\triangle U^2}. \tag{3.8}$$

The drop potential seen at the beginning of the discharge on GCD plots represents the R_{esr} (i.e., electrolyte resistance, cables resistance, and electrode resistance) and R_{edr} (i.e., ions' resistance to accessing the pores of the electrode). The graphical difference between both can be seen in Figure 3.4 (a).

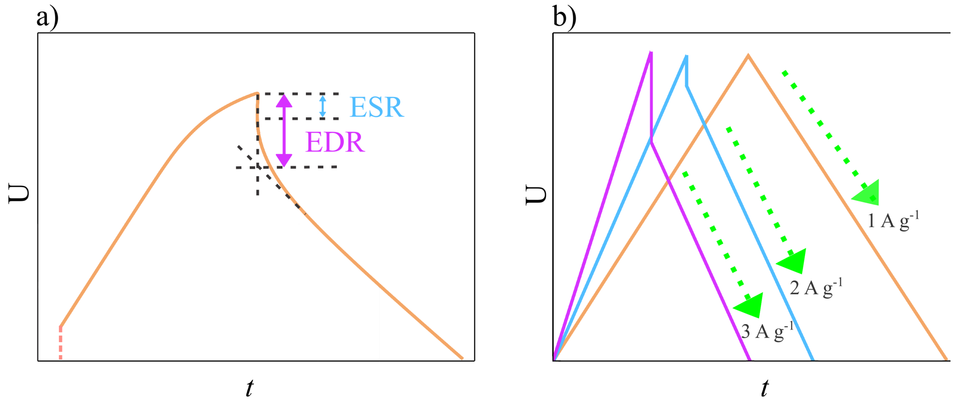

Figure 3.4 – (a) Parameters of galvanostatic curve used to determine the R_{esr} and R_{edr}. (b) GCD profiles with different gravimetric currents.

Based on that, it is possible to represent R_{esr} and R_{edr} as

$$R_{ESR} = \frac{\triangle U_{esr}}{2i}, \tag{3.9}$$

$$R_{EDR} = \frac{\triangle U_{udr}}{2i}, \tag{3.10}$$

where $\triangle U_{esr}$ and $\triangle U_{edr}$ are the drop voltages caused by the R_{esr} and R_{edr} in the discharge curve of the GCD. As can be seen in Figure 3.4 (b), the greater the applied current, the greater the voltage drop on the internal resistances. The drop voltage is seen as a perceptual of energy lost in the system to charge and discharge the SC [123–126].

3.1.3 Single Potential Step Chronoamperometry

Single potential step chronoamperometry SPSC is a technique in which a single or double voltage step is applied, and the current is measured as a response over time. The resulting current response depends of the electrochemical characteristics of the SC (i.e., EDL and faradaic) [33, 127–129]. The profile plot of Chronoamperometry (CA) measurements allows the identification of electrolyzed species, the ratio of peak oxidation and reduction current, the transfer of charge, ESR, leakage current, and energy storage [130]. Figure 3.5 illustrates the SPSC current response of a (a) typical SC without leakage current; (b) current vs. time considering the existence of leakage current and; (c) excitation waveform of SPSC experiment.

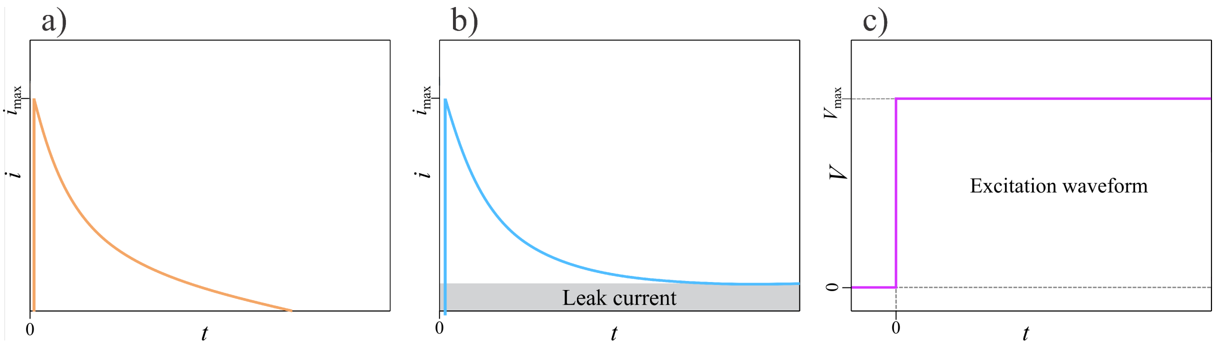

Figure 3.5 – Chronoamperometry experiments in two different situations: (a) without and (b) with leak current contribution. (c) The excitation waveform of an CA single-step experiment.

For electrostatic SCs, the equivalent circuit can be represented by a resistor in series with a capacitor circuit, and the current i_{edl} decay in function of time is described by

$$i_{EDL} = i_0 e^{\left(-\frac{t}{R_{ESR} C_{EDL}}\right)}, \tag{3.11}$$

where I_0 is the current in the exact moment when the potential is applied. The voltage on the SC (U_{sc}) increases exponentially as time progress, and it is a function of the WVW as described by

$$U_{SC} = (WVW)\, 1 - e^{\left(-\frac{t}{R_{ESR} C_{EDL}}\right)}, \tag{3.12}$$

The current in EDL devices theoretically tends to zero when the time tends to infinite. However, the current does not disappear in real-world SCs because a leakage current is always present in the experimental measurements. The leakage current is usually driven by parasitic resistances that drive self-discharge (i_{self}) [131] and redox reactions, especially at high WVW. The diffusion-controlled redox reaction in the function of time is described as

$$i_f = \frac{nFA_sC\sqrt{D}}{\sqrt{\pi t}}, \tag{3.13}$$

where A_s is the superficial area, C is the capacitance, and D is the coefficient's diffusion. Then, the current response in time of a SC can be described by the sum of the three aforementioned currents (i_{edl}, i_f, i_{self}) as

$$i_{Total} = i_{EDL} + i_F + i_{self}. \tag{3.14}$$

3.1.4 Electrochemical Impedance Spectroscopy

EIS is a powerful, low-cost, non-destructive, and extensive technique used to characterize energy storage devices, sensors, and electrocatalysis [132]. Concerning SC, it is possible to acquire several physical properties based on EIS, such as (*i*) porous distribution and shape, (*ii*) electrolyte resistance in the pores of the electrodes, (*iii*) ESR, (*iv*) interfacial impedance, and (*v*) charge transfer resistance [133]. These properties are fundamental to understand the SC electrochemical process. Moreover, EIS is a much easier technique than CV, GCD, and CA in regards to analyze variables separately.

The EIS technique measures the system impedance as a function of frequency, applying an electrical perturbation of small magnitude that can be a sinusoidal voltage (i.e., potentiostatic mode) or sinusoidal current (i.e., galvanostatic mode) superimposed on a steady state of voltage or current at a controlled frequency (e.g., typically from 10 mHz to 100 kHz) [134, 135]. Additionally, the applied voltage can be described by

$$E_{(t)} = |E_0| \sin(\omega t), \tag{3.15}$$

where ω is the angular frequency given by $2\pi f$, $E(t)$ is the steady-state voltage, and E_0 is an electrical perturbation of small magnitude. As a result of the applied voltage, the measured current is described by

$$i_{(t)} = |i_0| \sin(\omega t + \varphi), \tag{3.16}$$

where the phase angle (φ) depends on the circuit elements. If the circuit presents resistors, the voltage is in phase concerning the current. Otherwise, for a non-resistive circuit, the current phase angle will shift + 90° for an ideal capacitor and - 90° for an ideal inductor regarding the voltage phase angle.

The impedance $Z_{(\omega)}$ expressed by

$$Z_{(\omega)} = \frac{E_{(t)}}{i_{(t)}} = \frac{|E|_{(0)} \sin(\omega t)}{i_{(0)} \sin(\omega t + \varphi)}, \tag{3.17}$$

is a complex value that represents the transfer function of the system, which is obtained by the relation between the input (voltage) and output signal (current). For EIS measurements, the function transfer is expressed in ohms (Ω). Representing the impedance by complex algebra is very useful because it simplifies the circuits analysis and the identification of magnitude and phase. Besides, an alternative representation can be expressed as

$$Z = Z_{re} + jZ_{img}, \tag{3.18}$$

where Z corresponds to the complex number, Z_{re} to its real part, and Z_{img} to its the imaginary part.

Usually, the results are plotted in Nyquist or Bode plots. The first shows the real and imaginary impedance contributions and Z is represented as a vector of length |Z| expressed by

$$|Z| = \sqrt{Z_{re}^2 + Z_{img}^2}, \tag{3.19}$$

while the latter is represented by the magnitude |Z| or phase angle (φ) concerning the logarithm of the frequency (f) [1].

To represent and obtain meaningful results is essential to ensure causality, electrochemical stability, and linearity. So, in practical ways, (*i*) the SC needs to be stable and does not change with time, (*ii*) the perturbation signal E_0 needs to be linear and presents low amplitude (i.e., ≈ 5-10 mV for potentiostatic mode) to ensure a linear current behavior and electrochemistry stability (i.e., only adsorption/absorption of ions and no oxidation or reduction reactions at the electrode surface) [136], and (*iii*) the current must be a direct result of voltage perturbation, ensuring the system causality [137]. After ensuring these three requirements, it is possible to represent the system's frequency response fitting the experimental data to a suitable equivalent system model [138].

Furthermore, understanding the EIS data correctly to propose an equivalent circuit that fits the system response appropriately is a challenging task [73], and it still remains an open question in the scientific community. An equivalent circuit model and its components can represent unique experimental data [137], which leads to non-consensual models. Therefore, it is vital to ensure the best instrumentation configuration to acquire the more trustful results as possible to avoid systematic misinterpretation.

Overall speaking, the problem of nonlinearity is smaller as the signal amplitude is small. Nevertheless, if the signal has a minimum amplitude, the stochastic error increases significantly. The reason is that the value of current decreases drastically over time, and the analog to digital converter cannot accurately measure it. The diameter of the semi-cycle seen at high frequency in Nyquist plot can be interpreted as the charge transfer resistance R_{ct}, which decreases according to a sinusoidal voltage [139], in agreement with:

$$R_{ct} = \frac{RT}{nFi_0}. \tag{3.20}$$

Figure 3.6 (a) presents how the resistance R_{ct} is affected by an increase in surface overpotential. In addition, response in the low frequency range gives essential information about the presence of water splitting (Figure 3.6 (b)). Usually, if the applied voltage is higher than WVW, deviations from linearity caused by undesired faradaic processes, or the presence of water-splitting are observable. The number labels in Figure 3.6 (b) represents a degree of linearity of the system (i.e., 1 presents a linear system and 6 the presence of water-splitting). The linearity of an EIS experiment can also be evaluated by observing the input and output signal and this can be visually expressed through a Lissajous plot [73].

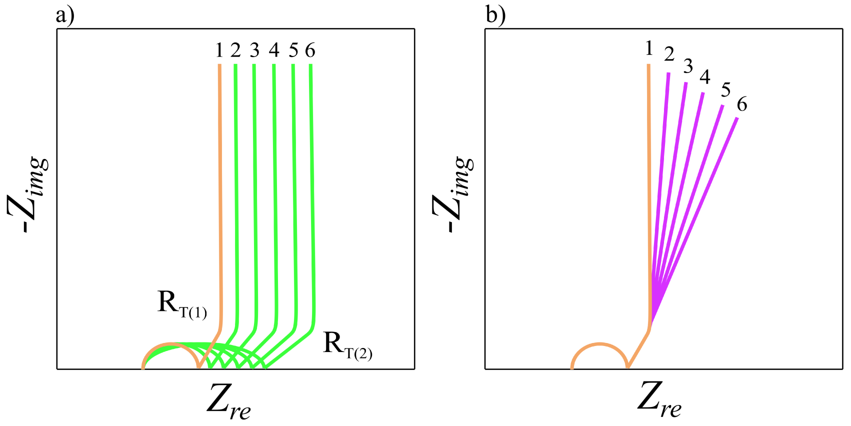

Figure 3.6 – (a) deviations from the linearity verified in the complex-plane plots at low frequencies commonly indicating the presence of water-splitting. (b) Effects of the surface overpotential in the charge transfer resistance. Figure adapted from [63].

3.2 Results and Discussion

3.2.1 Cyclic Voltammetry Results

In CV experiments, the voltammogram differs concerning the scan rate because the ESR affects its shape. For low scan rates, the profile tends to be almost rectangular perfectly because time is enough, especially for ions to access the electrode pores, so energy losses on internal resistances are low due to the small current. For a high scan rate, the voltammogram curve does not have its rectangular shape, instead of showing rounded corners. In this condition, time is insufficient for ions to access the deepest pores, and part of the energy is dissipated on the ESR as a result of the high current. In this way, Figure A.3 (see Appendix A) presents the CV voltammograms at several scan rates.

Figure 3.7 shows how the configuration of parameters of the CV test impacts the electrochemical result for incorrect experimental setups. In Figure 3.7 (a), it is possible to see the impact of different voltage ranges on the voltammogram. The CV voltage range was set at 2.5 V, 5.0 V, and 10 V, which are the available values. Thus, the correct voltage range should be the closest value larger than 1.2 V, which is 2.5 V in the available potentiostat. Otherwise, if the voltage range is set wrongly (i.e., 5 and 10 V), the measurement includes an error. The potentiostat modulates the voltage in CV experiments, so the measured

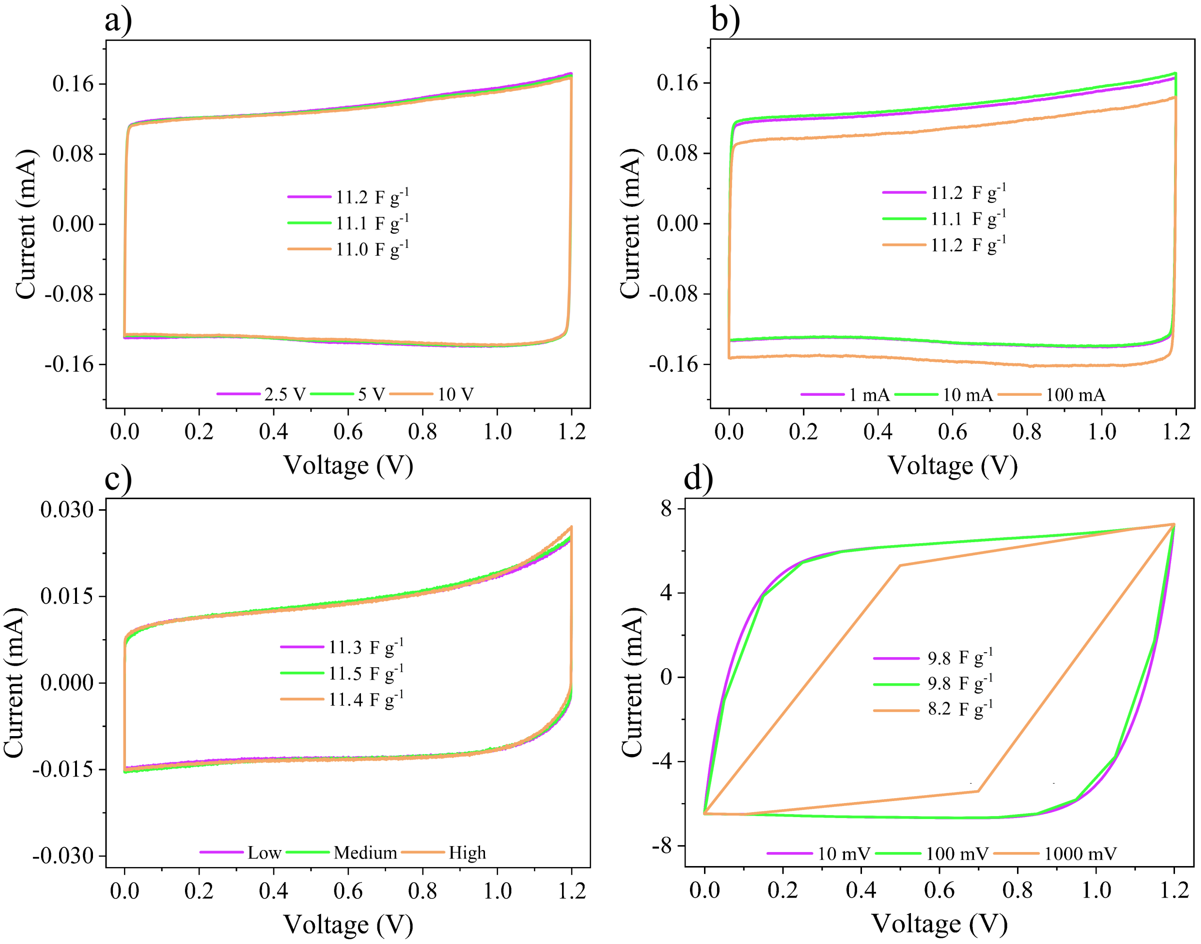

Figure 3.7 – CV measures at 1.2V and different setups. (a) Voltage ranges at 10 mV s^{-1} (b) Current ranges at 10 mV s^{-1}. (c) Bandwidth levels at 1 mV s^{-1}. (d) Sample intervals at 500mV s^{-1}.

voltage is crucial to the analysis. The error in CV plot when a 10 V range is chosen is of almost 200 mF g^{-1} in the acquired capacitance concerning the area of the voltammogram.

Figure 3.7 (b) shows a clear trend of the positioning of the voltammogram according to the current range. The correct, current range is 1 mA for the maximum current (approx. 0.16 mA) seen in the CV plot. Initially, the proper current range is set based on a value higher or equal to the maximum current of the experiment. However, if there is more than one available current range higher than the maximum current, the lowest value is selected to keep a good resolution and accuracy. For a current range of 100 mA, errors of position and capacitance calculated are observed. The higher position error is especially problematic because it shows that the discharged energy is higher than the energy accumulated during the charging, which indicates a wrong measurement clearly.

Figure 3.7 (c) shows how the bandwidth can alternate the perception of current at vortex potential (i.e., where the sweep direction is reversed in the voltammogram). The bandwidth expresses a stability factor, and it is fundamental to assure a good measure without oscillations. The stability factor usually is defined by the time constant of the SC.

In practical ways, it defines how fast the potentiostat has to work. In general, the smaller the time constant and the larger the capacitance, the greater must be the stability factor. In addition, if it is impossible to know the exact bandwidth value used by the potentiostat, it is recommended to repeat the measurements for the different available bandwidths to evaluate the results properly. At this experiment, a low scan rate of 1 mV s^{-1} was set, so the potentiostat does not need to respond quickly and mitigate transitory errors. As a result, the stability factor must be low to result in an adequate measurement. On the other hand, a higher current at vortex potential is observed for a wrong stability factor (medium or high), which does not correspond to correct WVW of the SC.

Lastly, Figure 3.7 (d) shows how the sample intervals impacts in the CV measurements. The data output of the potentiostat is digital, as mentioned before. As some experiments may require days or weeks, it is possible that a long sampling interval is used to reduce data storage. Nevertheless, CV consists usually of a fast procedure, and the voltammogram shape is fundamental to defining some SC properties. Therefore, a correct time interval consists of storing data points at every instant that the slight variation in voltage (in this case, 10 mV) is identified, which aids to keep the CV shape trustful and without variations. The CV shape becomes highly deteriorated for a sample interval of 100 mV and 1 V, making the analysis invalid due to its low precision.

3.2.2 Chronopotentiometry Results

Figure A.4 shows how the configuration of parameters impacts the GCD measurement. Figure A.4 shows that as the discharge current (e.g., electrical load) increases, lower is the capacitance and consequently the stored energy. Furthermore, Figure A.5 illustrates the plot of cycling performance and coulombic efficiency of the studied SC.

Figure 3.8 (a) shows that the voltage range does not cause any modification in the charge and discharge profile or specific capacitance for the studied SC. Nevertheless, the method to identify the correct voltage range is the same as presented for the CV test. For the GCD test, the correct voltage range is 2.5 V even if 5 V or 10 V leads to similar results. In the detail of Figure 3.8 (a), it is possible to see the differences between the EDR and ESR for the discharge profile.

Figure 3.8 (b) shows how the current range impacts in GCD measurements. The applied current in this experiment for charging and discharging the SC is 0.05 mA, which means the current range should be 0.1 mA for the available potentiostat. The GCD experiment consists in applying a constant current while changing the gain of an internal amplifier in the potentiostat, which aims to simulate a variable load. As a result, the current is the same even if the voltage varies eventually. It also means, however, that the current is a variable sensitive to the voltage and needs to be measured constantly by the equipment, so charging and discharging of the SC occur linearly. The drastic changes in

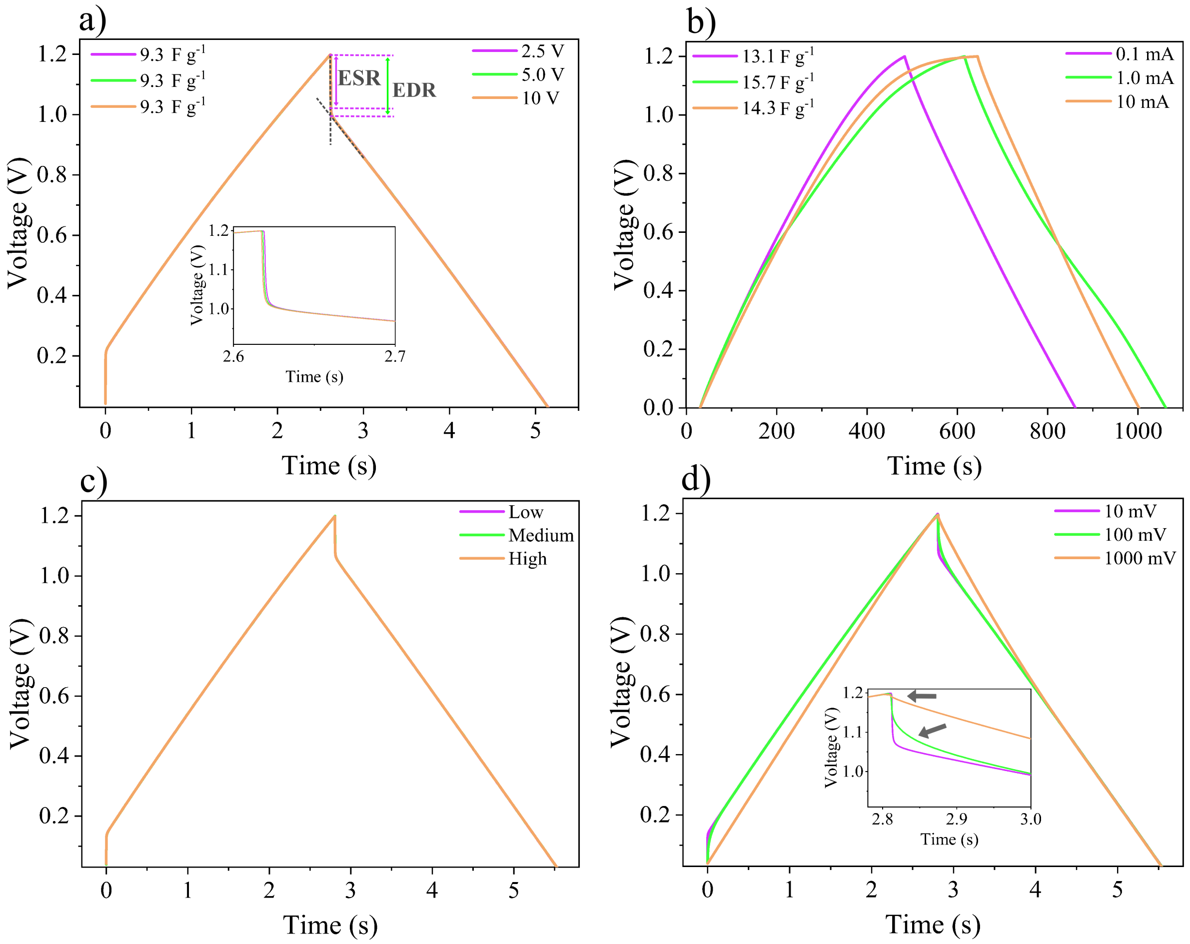

Figure 3.8 – CP measures at 1.2V and different setups. (a) Voltage ranges. (b) Current ranges. (c) Bandwidth levels. (d) Sample intervals.

Figure 3.8 (b) for the current ranges of 1 mA and 10 mA are due to the unprecise control of the current by the potentiostat in these current ranges. Not only the GCD profiles changes massively, the capacitance measured also changes significantly. For a current range of 1 mA, the specific capacitance presented an error of 2.52 F g^{-1} or almost 20 %.

Figure 3.8 (c) shows that the bandwidth does not produce any difference in GCD profile. Nevertheless, the bandwidth should be defined according to the charging and discharging time period. Generally speaking, for a short discharge time, the stability factor also needs to be lower.

Lastly, Figure 3.8 (d) shows how the sampling based on the voltage variation affect the ESR and EDR identification. The voltage interval for sampling must always be the lowest possible because the voltage drop due to internal resistance is a fundamental feature to determine EDR and ESR of SCs. For a voltage interval greater than 10 mV, the measured EDR and ESR change for the available potentiostat. Depending on the interval, it is not possible to even identify EDR and ESR properly.

3.2.3 Chronoamperometry results

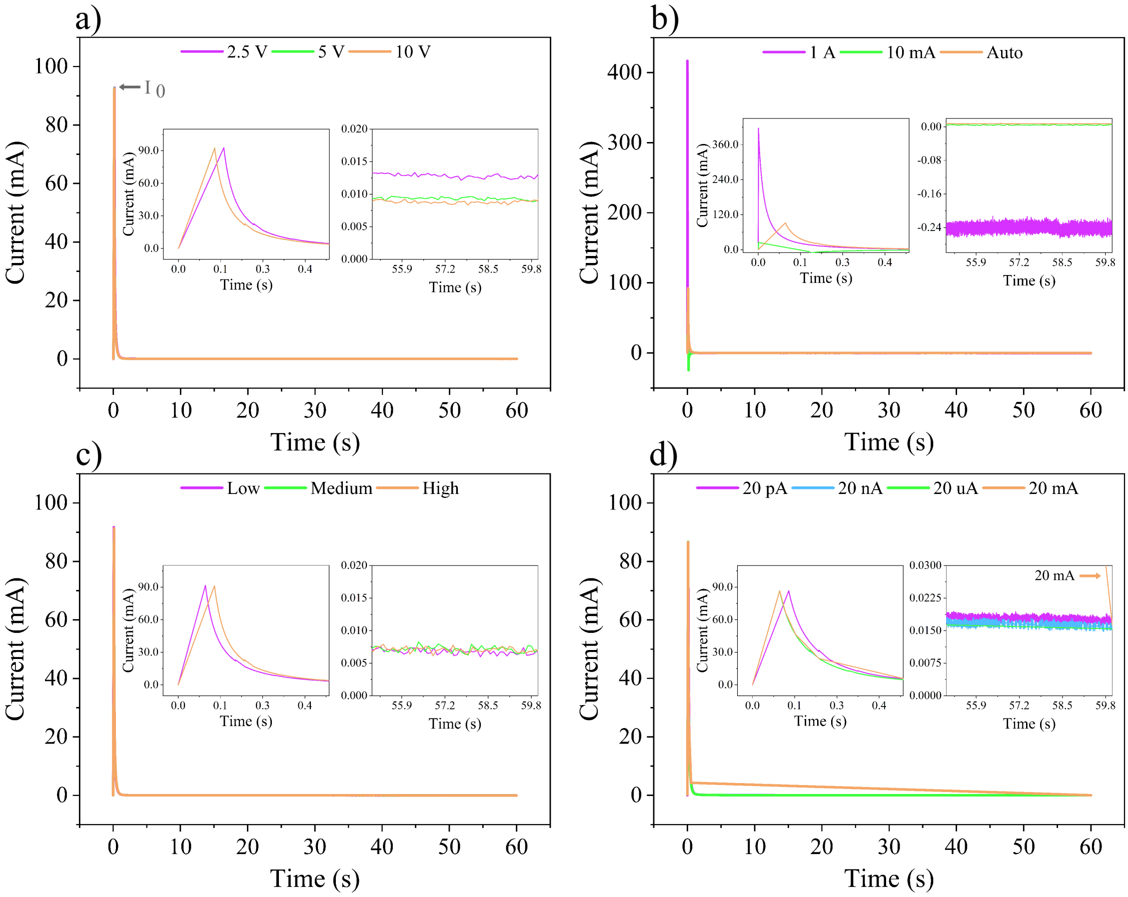

Figure 3.9 – SPSC measures at 1.2 V, 60 s of single potential step, and different setups. (a) Voltage ranges. (b) Current ranges. (c) Bandwidth levels. (d) Sample intervals.

Figure 3.9 shows the SPSC experiments at a diverse voltage and current ranges, bandwidth levels, and sample intervals. It is presented how the incorrect configuration of these parameters affects the SPSC measurements of SCs. Figure 3.9 (a) shows how the voltage range affects the SPSC results. The correct voltage range is 2.5 V because a single voltage step of 1.2 V is applied. The incorrect voltage range, which is 5 V or 10 V for the available potentiostat, reduces the current at 60 seconds by 33%. Note that voltage range is critical because the current response over time is used to define the correct WVW [77].

Figure 3.9 (b) shows how the current range affects SPSC results. Different from the procedures presented so far, the correct configuration for the current range is to set it to an automatic adjustment. The reason for the automatic current range is due to the extreme current variation during the SPSC procedure, reaching high currents at initial phases and a minimal current at the final phases because the SC is almost fully charged and yields only leakage current. The automatic current range sets the potentiostat to adjust the current range internally during the SPSC process, keeping an adequate resolution along with the experiment progression.

Figure 3.9 (c) shows how the stability factor of the bandwidth impacts the SPSC measurements. The three available settings are compared, and the values of maximum current and of the current at 60 seconds were not affected by the bandwidth. The correct bandwidth setting should be an automatic adjustment because the device presents a response much faster in the initial stage of the experiment than in the final stage. Nevertheless, the available potentiostat does not have an automatic bandwidth setting. Therefore, the best approach is to decide upon the more critical feature for the analysis to select the bandwidth. Generally speaking, a “higher” bandwidth should be chosen if it is necessary to prioritize the transient at the initial step, while a “lower” bandwidth should be chosen if analyzing the current in the final stages is the priority.

Lastly, Figure 3.9 (d) shows how the sample intervals of current affect the SPSC, which is the most critical configuration of the SPSC procedure. At first, assuming that a large current sample interval is set, the result may not be adequate if very small changes in current occur because the potentiostat does not store the sample due to the large current sample interval. On the other hand, excess data points may be stored when a too small current sample interval is set. Therefore, the correct configuration of sample interval becomes entirely empirical and dependent on the device under analysis. Usually, at the first time a SC goes through an SPSC analysis, the magnitude of the current at the final stage is unknown. So, it is recommended to perform the first experiment with a very low current sample interval to find the magnitude of the current for a fixed experiment time, which becomes the target current. After that, a current sample interval one thousand times lower than the target current is set to keep the measurement consistent and to optimize the amount of stored data, especially for long-time SPSC experiments required to evaluate SCs.

For the SC studied and the available potentiostat, a current sample interval of 20 pA was set for the first measurement. It was possible to identify that a current of approximately 20 uA is achieved at 60 seconds. Consequently, the current sample interval should be 20 nA or a smaller value. For comparison, a current sample interval of 20 mA yields a final current that diverges from the correct value. The stored data recorded by the potentiostat for each measure was 60 k, 18 k, 1.2 k, and 700 data points for current sample intervals of 20 pA, 20 nA, 20 uA, and 20 mA, respectively.

3.2.4 Electrochemical Impedance Spectroscopy Results

Figure 3.10 shows the plots for the EIS experiments. Each plot corresponds to results related to an essential parameter of EIS experiment, for which knowing the potentiostat and the fundamental electronic concepts prevents errors and optimizes the measurements. The mistakes in the configuration are usually observed when strange and random points in the Nyquist plot appear.

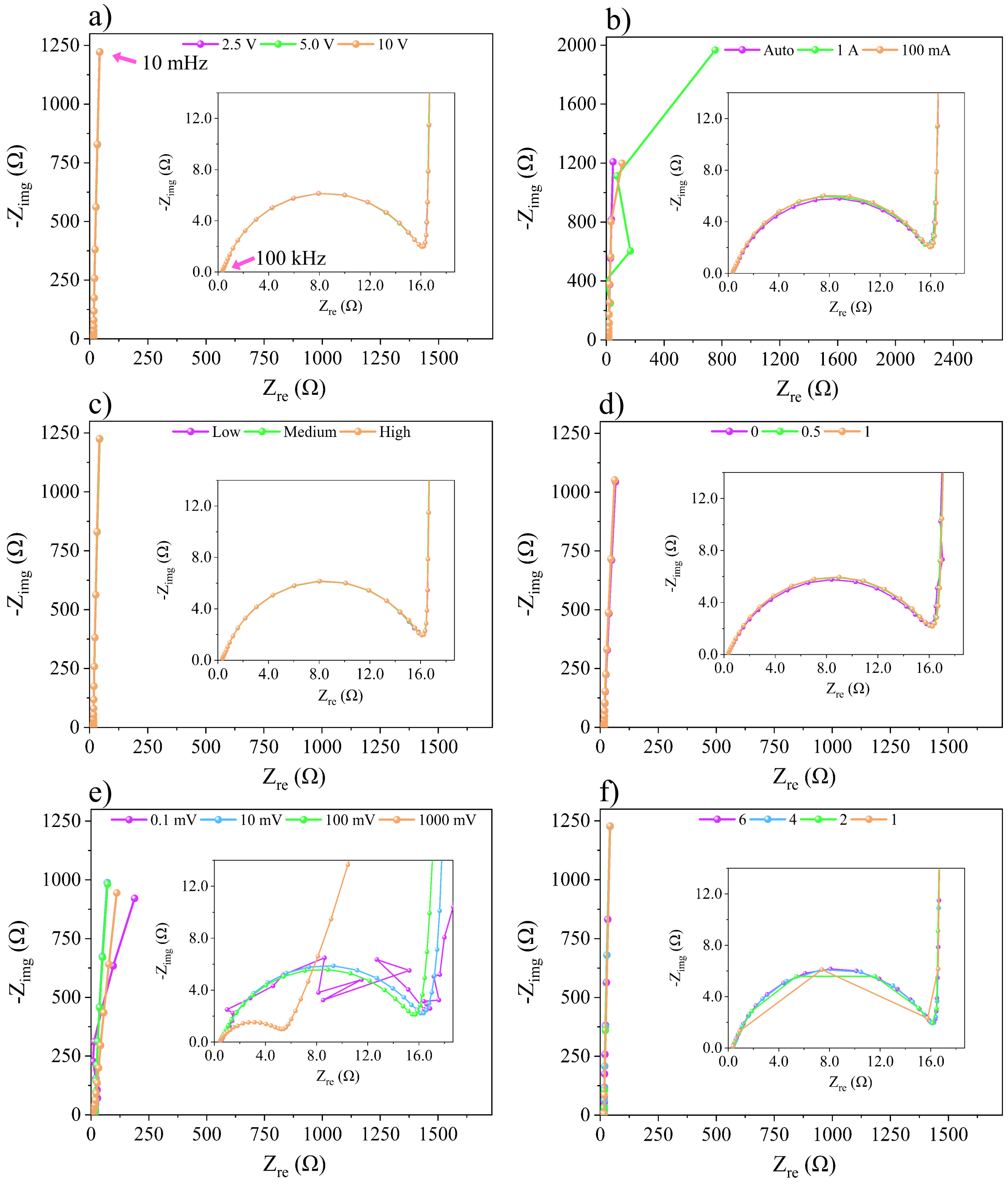

Figure 3.10 – Electrochemical impedance spectroscopy measures in the frequency range of 10 mHz to 100 kHz for different instrumental setups. (a) Voltage ranges. (b) Current ranges. (c) Bandwidth levels. (d) Waiting times. (e) Magnitude of the perturbation voltage. (f) Points per decade.

Figure 3.10 (a) shows how the voltage range impacts the EIS measurements. The EIS voltage range was set at 2.5 V, 5.0 V, and 10 V, which are the available values. The adequate voltage range should correspond to the lowest available voltage range that is larger than the configurated voltage value in the EIS experiment. For the device under test, a steady-state voltage of 0.3 V with a sinusoidal perturbation voltage of 10-mV peak was set, resulting in a maximum voltage of 0.31 V. Thus, the correct voltage range should be the closest value larger than 0.31 V, which is 2.5 V in the available potentiostat. Nevertheless, no noticeable differences in the Nyquist plot are noted for the available voltage ranges because the most critical variable of the device under test is the current.

Figure 3.10 (b) shows the impact of the current range in the EIS results. The potentiostat modulates the frequency of the sinusoidal voltage and measures the current to calculate the impedance |Z| at several frequencies. However, due to its modulated sinusoidal voltage, the magnitude of the impedance changes according to the frequency applied if the circuit is not composed only of resistors. Assuming that this experimental data could be fitted by a circuit consisting of a resistor R_{esr} in series with the parallel combination of a resistor R_{ct} and a capacitor C_{edl} represented by

$$Z_{eq} = R_{ESR} + \frac{R_L}{1 + j\omega R_L C}, \tag{3.21}$$

in which a change in the angular frequency ω during the experiment results in a change of the impedance of the circuit. In addition, the circuit's current also changes during the experiment due to the frequency variation as it is expressed as

$$i_{(t)} = \frac{E_{(t)}}{Z_{eq(\omega)}}. \tag{3.22}$$

Own this current variation during the experiment. It is fundamental to set the current range as automatic (if this feature is available) in the potentiostat. It means that the potentiostat used in this chapter (i.e., potentiostat model SP-200) sets the current range automatically during the experiment to ensure a more precise measurement according to the current magnitude variation. Based on this, the modifications saw to current ranges of 1 A, and 100 mA regarding the automatic range happens because as current decreases, the frequency falls. As a result, the signal-noise ratio intensifies, and the rate of errors rises.

Figure 3.10 (c) shows the EIS measurements concerning the three available bandwidth settings. Note that selecting the correct bandwidth is not simple because the capacitance of the device under test defines the time constant while the equivalent impedance changes with the applied frequency as described in Equation (3.22), which results in changing the stability factor accordingly to the applied frequency. For the available potentiostat, only one bandwidth can be selected at a time. In this case, the best approach is to define a fast bandwidth to avoid errors for high-frequency measurements. Nevertheless, no modification or stochastic errors in the Nyquist plot concerning the SC under test for all bandwidths are observed. However, it is essential to highlight that it does not mean that any bandwidth is adequate for EIS on a SC. The results are unique to the SC under test, for which the bandwidth was not critical.

Figure 3.10 (d) reports the waiting-time parameter. Also presented as “Wait for” in EIS measurements, it prompts a specific time delay before taking the measurement when the frequency changes to mitigate undesired errors caused by transients. The transient incorporated in the equivalent impedance may cause an error up to 4% if a delay of at least one period is not included [140]. Usually, the delay is defined proportionally to the period of the sinusoidal voltage signal. For the available potentiostat, the module of the impedance is calculated to all points, yielding an average impedance of 15.75 Ω, 16.09 Ω, and 16.12 Ω, for a waiting time 0 (no delay), 0.5 (half-period delay), and 1 (one-period delay), respectively. An error of approximately 2.3% is observed if the wait time is not configurated.

Figure 3.10 (e) shows the effects of changing the amplitude of the modulated sinusoidal superimposed in the steady-state voltage. Electrochemical reactions are defined by the current densities and are driven exponentially by electrical potential [141]. Therefore, the Butler-Volmer equation describes the kinetic control of a single reversible reaction in the not linear voltage function by

$$i = i_0 \left\{ exp\left(\frac{(1-\alpha)\, nF}{RT}\eta_s\right) - exp\left(-\frac{\alpha nF}{RT}\eta_s\right)\right\}, \tag{3.23}$$

where η_s represents the surface overpotential and α an asymmetry factor that defines the cathodic reaction and its fraction surface overpotential. Theoretically, it is the only electrostatic phenomenon that should be seen in SCs. However actually, faradaic reactions are observed for several reasons, such as contaminations during the porous materials production and electrolyte and electrode decomposition. From Equation (3.23), as the current changes, the impedance response changes consequently, resulting in different Nyquist plots, especially at voltages higher than 10 mV as seen in Figure 3.10 (e).

The result for 500 mV and 1000 mV is presented in a Lissajous plot where current and voltage are normalized in Figure A.6 [73]. As the system parameters are kept in linear regions, the Lissajous plot becomes more symmetric, as observed in Figure A.6. In the galvanostatic mode, every parameter needs to be checked to produce results within a linear operation region. For the device under test, the only modification is to select a lower current to guarantee the linearity and stability of the system. In Figure A.7 is possible to see the Nyquist plot for both modes with a steady voltage and current equal to zero.

Figure 3.10 (f) shows the effect of the number of points per decade in the Nyquist plot. To calculate de number of points measured, it is used

$$S_{Wrange} = \log\left(f_{high}\right) - \left(f_{low}\right), \tag{3.24}$$

$$N = S_{Wrange} * points_{decade}, \tag{3.25}$$

where S_{Wrange} is the sweep range, f_{high} is the highest frequency, f_{low} is the lowest frequency, and N the estimated points. So, for (6, 4, 2, and 1) points per decade, it represents 42, 28, 14, and 7 points measured during the experiment. Note that less than 6 points per decade lead to a deformed Nyquist plot. For the device under test, the adjustment of 6 points per decade was enough to represent the system well. More points per decade could produce a more precise representation, but it would increase the experiment time overly, affecting the SCs initial state. Therefore, a simple rule for the number of points per decade in SC measurements does not exist. Nevertheless, it is recommended to perform the experiment correctly and as fast as possible to avoid electrochemical reactions that may lead to alteration of SC characteristics, leading to a higher probability of stochastic errors.

3.2.5 Temperature Effects on Electrochemical Measurements

The effects of temperature in SCs characterization have been reported extensively concerning their application in high or low temperature conditions [34, 142–145]. Generally speaking, the temperature impacts the measurements massively in different ways [43, 51, 53, 146, 147]. Figure 3.11 shows the effects of temperature on CV, GCD, SPSC, and EIS measurements of a (1 M of LiCl) aqueous-based SC. Figure 3.11 (a) shows the CV measurements for different temperatures, which an exponential trend in anodic vertex voltage is observed. It can be concluded that the rate of faradaic processes and the decomposition of the electrolyte (water-splitting reaction) have increased due to the increase of temperature accordingly.

Figure 3.11 (b) shows GCD measurements for different temperatures. From a certain threshold temperature, the impact on the specific capacitance becomes significant. At 35°C, the capacitance increased by more than 50% compared to the other temperatures. One should expect it because the faradaic process starts to contribute to the energy storage characteristic of the device under test. In addition, the EDL is formed easily as the viscosity decreases with the increase of temperature and of the ionic diffusion increase, which leads to an increase of the capacitance consequently. Figure 3.11 (c) shows SPSC measurements for different temperatures. The temperature affects the parasitic resistances and the redox reactions, for which both are evaluated through the leakage current. At 35°C, the leakage current is more than two times larger than the current at 25°C.

Figure 3.11 (d) shows EIS measurements for different temperatures. Note how the Nyquist plot changes, especially at low frequencies (i.e., 10 mHz), due to the nonlinearity of the system caused by the increase in temperature. The detail of Figure

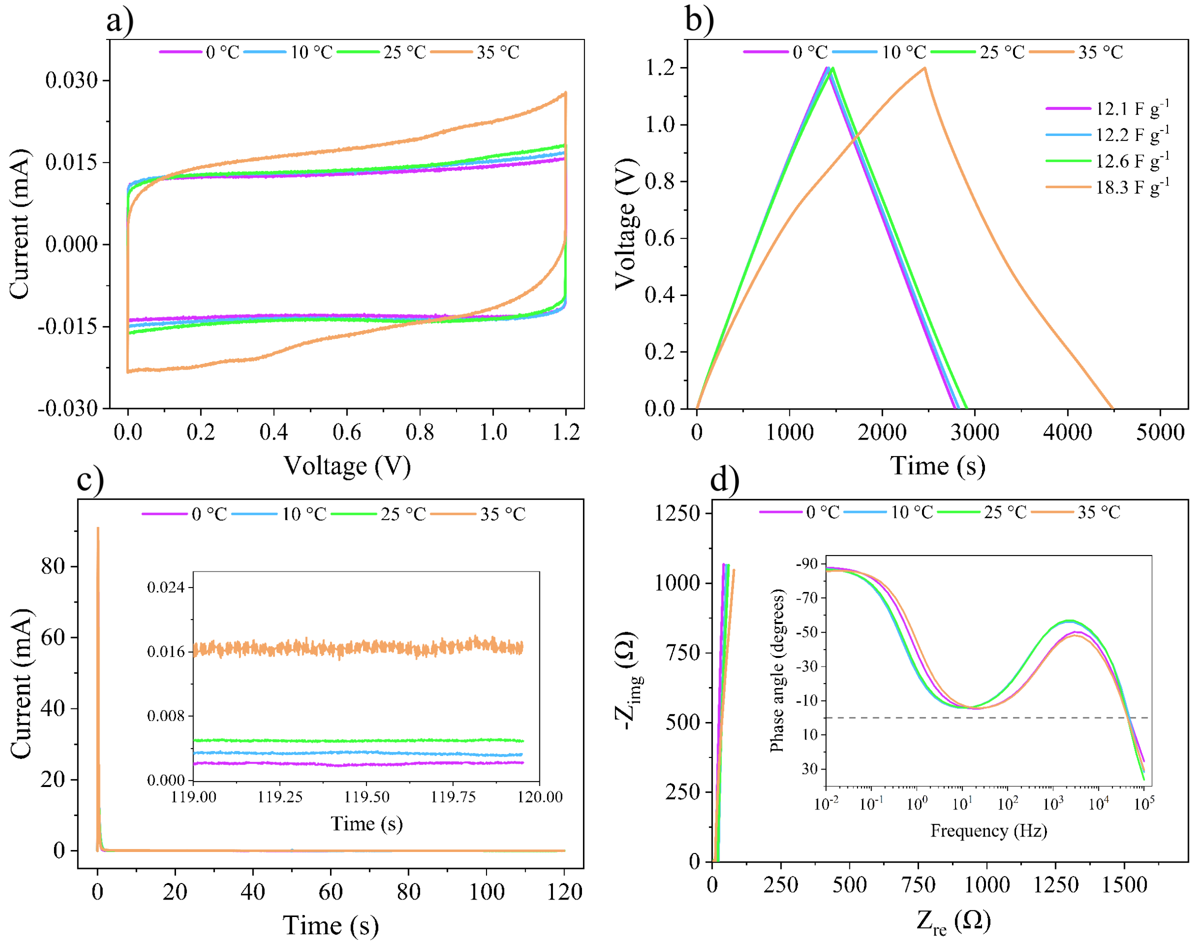

Figure 3.11 – Electrochemical findings from a (1 M of LiCl) SC at 1.2 V and different temperatures. (a) Cyclic voltammetry at 1 mV s^{-1}. (b) Galvanostatic charge-discharge at 0.003 A g^{-1}. (c) Single potential step chronoamperometry with a single step of two minutes. (d) Nyquist and Bode's diagrams are extracted from electrochemical impedance spectroscopy measured in the interval of 10 mHz to 100 kHz.

3.11 (d) shows the Bode diagram. Note how the change in temperature modifies the phase angle. As the temperature changes, the ion absorption in the electrode pores changes due to lower or higher ionic resistance. As a result, the time constant of the device under test changes, which reflects on the phase observed in the Bode diagram profile consequently.

3.3 Concluding Remarks

This part of the Dissertation has focused on describing, demonstrating, and discussing intensively and didactically the misleading experimental data and results of electrochemical measurements of symmetric SCs that are consequences mainly from wrong setup configurations and a careless approach towards the sources of stochastic errors. Adjustments related to voltage and current ranges, bandwidth and voltage and current sample interval are explained, so a correct configuration may lead to a high-quality and reproducible SC characterization for CV, SPSC, GCD, and EIS procedures. The studied case and the practical rules presented in this chapter are strong suggestions to ensure data reliability and address fundamental questions related to errors in instrumentation setup or unexpected physical-chemical results. Moreover, the assessment of the procedures aims to contribute positively to the discussion of standardization and measurement reliability, especially with the quality of the data presented in Chapters 4 and 5.

4 Electrodes Under Compression

There is a massive interest in raising the energy storage in SCs by applying different techniques to improve the electrode and electrolyte features. One way to improve the electrode is to apply compression. It minimizes ions' distance travel, avoids interfacial impedances, improves the conductivity, and falls the system's resistances. However, the ion dynamics into different pore size distributions in SC electrodes after applying compression are still rare. Here we present a extensive study demonstrating and explaining the ion dynamics of five electrolytes into different pore size distributions in supercapacitor electrodes under compression, tracking scanning electron micrographs, nitrogen adsorption/desorption analysis, and electrochemical measures. The results show that it is possible to raise the energy density by more than 160 % when the electrode is compressed until the micropores match in dimensions with the electrolyte's hydrated ion size, creating a superionic state. In contrast, if excessive compression is applied, the capacitance falls more than 25 %. In summary, the pore size distribution modifications caused by compression significantly affect the ion dynamics into the pores of Activated Carbon (AC), improving several features of SCs.

4.1 Experimental Section

4.1.1 Preparation of Electrodes

The ink was produced with the AC YP-80F (Brunauer-Emmett-Teller (BET) specific surface area = 2271 m^2 g^{-1}) from Kuraray, carbon black percolator model Black Pearls 2000 from Cabot, and Polyvinylidene Fluoride (PVDF) binder from Aldrich Chemistry. The ink was prepared by mixing AC (80 wt. %), Carbon black (10 wt. %), and PVDF (10 wt. %). In 2.5ml of N-Methyl-2-Pyrrolidone (NMP) solvent for 30 minutes in an ultrasonic sonicator. To prepare the electrode film was added 50 µL of ink directly over a 16 mm stainless steel spacer to prepare the electrodes. The electrode film was also vacuum dried for 4 hours at 80 °C the spacer with liquid ink above to form the solid electrode. The electrodes formed presented an average mass of 17.15 mg.

4.1.2 Compression of Electrodes and Cell Aseembly

To apply the compression, a manual hydraulic press of the Specac model GS15011 was employed with a manometer changed to work in the range of 0 to 300 Psi. The minimum pressure that ensures the electrical contact between the electrodes is at least 30 PSI. Unfortunately, we could not increase the compression to pressures higher than 260 PSI. Because, after applying more than 260 PSI, the electrodes started to short-circuit. The short-circuit can be seen in Figure 4.1 as an abrupt rise in the chronoamperometry experiment after compressing more than 260 PSI. In addition, we performed all experiments applying pressure instead of measuring the electrode thickness because it turns the work more reproductive and does not require the electrode's mass or initial electrode's thickness. All results presented are based on triplicate or quadruplicate measurements of the supercapacitors under compression.

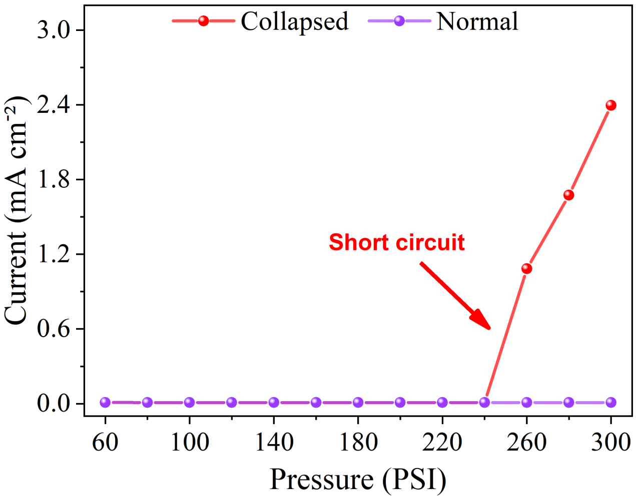

Figure 4.1 – Electrochemical behavior from chronoamperometry experiment, when the electrodes short circuit between then.

All SCs were assembled inside a coin cell with a CR2032 package without the spring. The spring was removed to reduce the influence of its mechanical strain on the obtained results. Since we are working in an atypical situation, was necessary inserting the cells inside a sterilized polystyrene Petri dish with two current collectors to connect the potentiostat to the SC's electrical terminations cell (See Figure 4.2.)

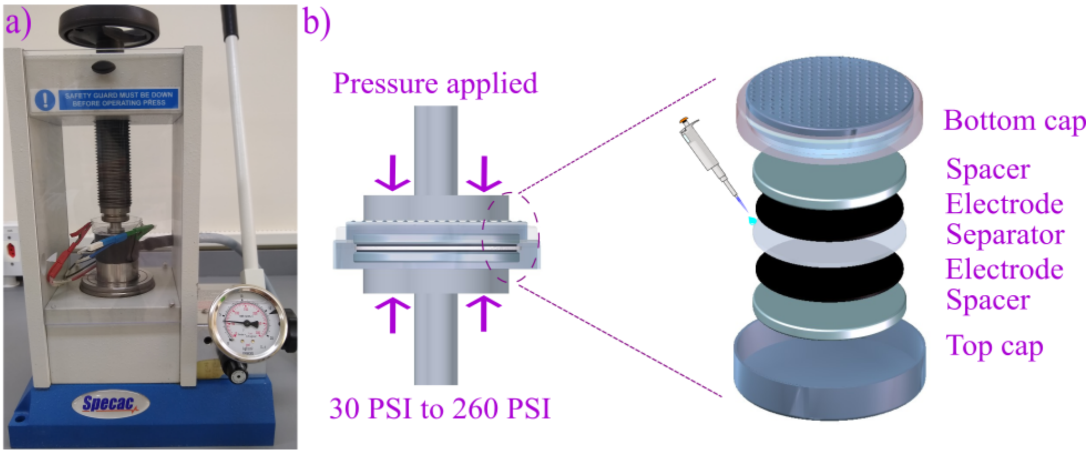

Figure 4.2 – Experimental setup that was used to compressing the electrodes. (a) Hydraulic press modified to measure the pressure applied from 0 PSI to 300 PSI and the electrical connection to the CR2032 cell. (b) Internal view of the cell.

4.1.3 Sample Preparation to Scanning Electron Microscope Analyses

To obtain the pictures from 0 PSI electrodes using the scanning electron microscope, we only used the electrodes made above the current collector, as shown in Figure 4.3 (a). Though to 100 PSI and 260 PSI, something happened when compressing the cell. The electrode was transferred to the separator as shown in Figure 4.3 (b) to Figure 4.3 (d). We cut that separator into a small piece and analyzed with the scanning electron microscope the electrode transferred to cellulose paper as shown in Figure 4.3 (e - f).

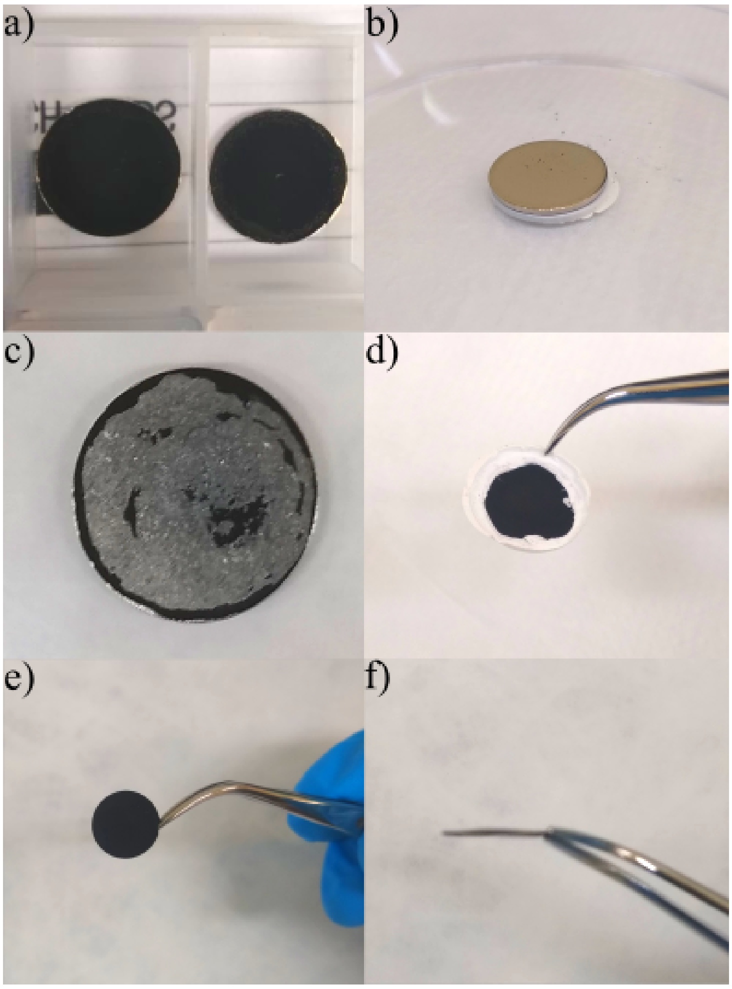

Figure 4.3 – (a) Sample without any compression. (b) Separator between electrodes. (c) Current collector after applying pressure. (d) Electrode transferred to cellulose separator. (e) and (f) Electrode cut in a smaller piece.

4.1.4 Sample Preparation to Nitrogen Adsorption-Desorption Isotherms

Initially, the samples were conditioned in a vacuum oven at 105 °C for at least 12 hours. After the samples reached thermal equilibrium at room temperature, the samples' mass was measured (20 mg) and then taken to the equipment for treatment at 180 °C until reaching a pressure constant of 3 µmHg. After treatment, the sample was analyzed considering micropores with an equilibrium time of 30 s. The minimum mass requires to determine the nitrogen adsorption-desorption isotherms is much bigger than the mass of an electrode. Thus, the electrodes above were prepared in a Petri dish as shown in Figure 4.4 (a) with the same ink and process of the electrodes produced to assembly the SCs. As shown in Figure 4.4 (b), we remove the solid electrode from the Petri dish's bottom after drying, as shown in Figure 4.4 (c). After it, a piece of powder was stored and target as the 0 PSI powder. We want to know the effect of compression in the same way as the electrodes compressed inside the cell CR2032. We took the other part of the powder and insert it in the steel die to apply 260 PSI of pressure, as shown in Figure 4.4 (d) and Figure 4.4 (e). This powder compressed turned a pellet, as shown in Figure 4.4 (f). Hence, the analysis was performed on activated powder YP-80F from Kuraray, one electrode without compression, and one pellet electrode with 260 PSI of pressure.

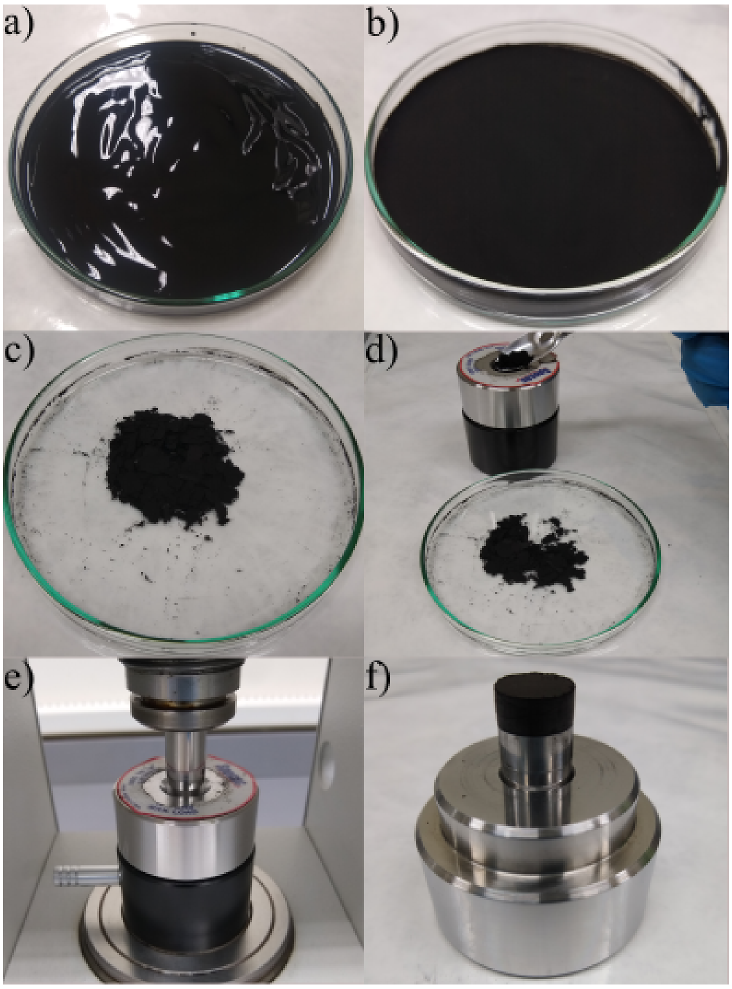

Figure 4.4 – Samples conditioned to the determination of nitrogen adsorption-desorption isotherms. (a) Ink deposited above the petri dish. (b) Electrodes formed by the ink dried at 80 °C in a vacuum oven. (c) Electrodes removed from the bottom. (d) and (e) Electrode powder being compressed. (f) Pellet formed by the electrode powder's compression.

4.2 Electrochemical Measurements

The full results presented are based on triplicate or quadruplicate measurements of the supercapacitors under compression. The CV, EIS, and CA experiments were performed with an electrochemical workstation from BioLogic (Model: SP-150) at room temperature of ≈ 25 °C and two-electrode configuration. The CV measurements were performed at several WVW, and the scan-rate varied from 10 mV s^{-1} to 200 mV s^{-1}. The CA measurements were performed with two minutes of constant voltage for various WVW. All the EIS experiments were set with the same parameters. The constant voltage was set at 0.3 V with a sinusoidal signal in the frequency range of 100 kHz to 10 mHz and an amplitude of 10 mV (peak-to-peak). The GCD experiments were performed at several gravimetric currents. The specific capacitance (F g^{-1}) was calculated from the discharged curve provided by the GCD experiments using

$$C_{\text{spec}} = \frac{I\Delta t}{m_e \Delta V}, \tag{4.1}$$

where Δt is the total discharge time, I is the constant discharge current, m_e is the active mass of the electrode and ΔV the constant voltage used to charge the SC excluding the ΔV_{drop} that is an abrupt change in the voltage during the discharge. Through the specific capacitance, it is possible to calculate the specific energy following

$$E_{\text{spec}} = \frac{V^2 C_{\text{spec}}}{2}. \tag{4.2}$$

The maximum power delivered by the SC to a load can be calculated by

$$P = \frac{V^2}{4ESR}, \tag{4.3}$$

where V is the maximum constant voltage used to charge the SC, and the ESR is the equivalent series resistance extracted from the GCD curves and can be calculated by

$$ESR = \frac{\Delta V_{\text{drop}}}{2I}. \tag{4.4}$$

4.3 Dynamics of Solvated Ions Into Different Pore Size Distribution

4.3.1 Activated Carbon Morphology Under Compression

It is investigated the effect of compression on the AC electrode's morphology by Scanning Electron Microscope (SEM). Figure 4.5 presents micrographs that were taken from the samples (a-c) as a prepared electrode material and compressed at (d-f) 100 PSI and (g-i) 260 PSI. As can be observed, massive macropores are highly reduced in size after compression, and the particles started to be closer to each other. For another perspective, Figure 4.5 (j-k) illustrates the squeeze of the electrode conceptually. These electrode structure modifications are highly related to the SCs electrochemical performance, mainly because the morphology defines the electrode conductivity, thickness, contact surface, and pore size distribution.

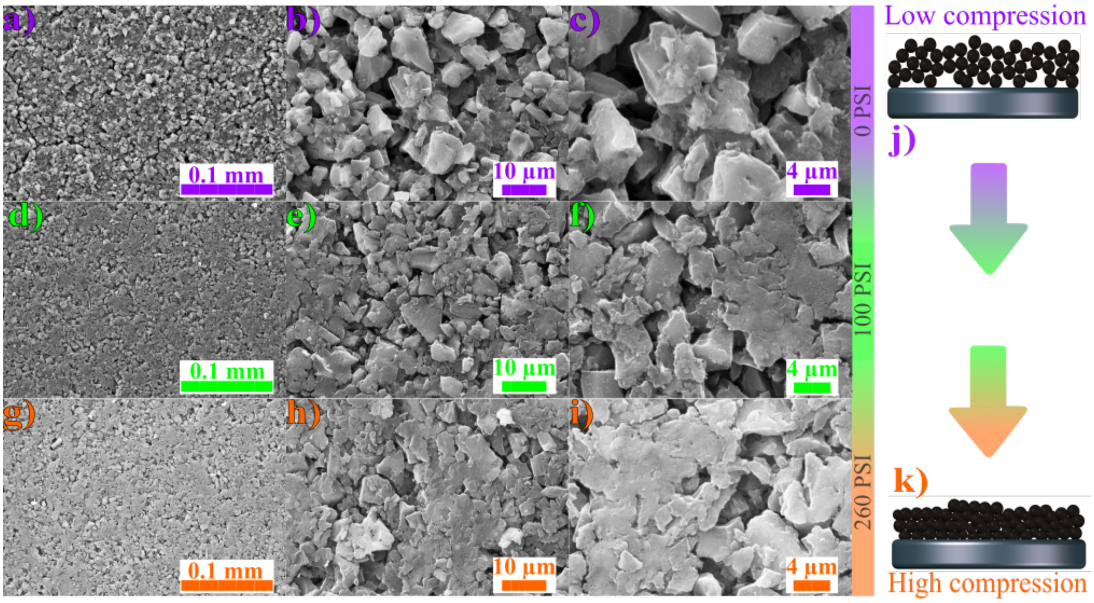

Figure 4.5 – Scanning electron micrographs took from the electrodes manufactured with activated carbon YP-80F. (a - c) Micrographs are taken from as-prepared electrode materials. (d - f) After being compressed under 100 PSI and (g - i) after compression of 260 PSI. j) and k) Schematic representation of electrode particle spaces and interaction with the current collector.

4.3.2 Pore Size Distribution of Activated Carbon Under Compression

However, micrographs cannot infer if the mesopores and micropores were also modified. For this reason, to have a better matter characterization, the nitrogen adsorption/desorption isotherms analysis is employed to reveal the effect of compression on the pore size distribution. The raw YP-80F powder is applied as a contrast to check if the coating was adequately prepared. The YP-80F is named P-0P. The electrode without compression is named E-0P, and the electrode squeezes at 260 PSI, E-260P. Figure 4.6 presents the isotherms. Up to the relative pressures of $P/Po < 0.9$, the P-0P was the sample that adsorbed the highest quantity of nitrogen, as seen in Figure 4.6 (a). The lower adsorbed quantity to E-0P and E-260P is expected because the binder used to manufacture the electrodes blocks the AC's smallest pores [148], reducing the superficial area (Figure 4.6 (b)). To relative pressure higher than 0.9, a massive rise in the quantity of adsorbed nitrogen is observed in E-0P and E-260P. It suggests compression activated the AC electrode. This physical activation alters the density and structural cavities improving large pores undetectable for P-0P isotherms [149].

Moreover, it is essential to point out that the quantity of nitrogen adsorbed by E-260P increased 18 % compared with E-0P in almost all relative pressure. The higher quantity of nitrogen adsorbed seen in E-260P can be explained by greater Van der Waals interactions provided by the pores overlapping when the gas is in contact with the pore walls and a pore shape modification (i.e., cylinder to a slit shape) caused by the compression [150,151]. Figure 4.6 (c) illustrates the increase of 13 % in the cumulative pore volume after compressing the electrode and is mainly influenced by pore width smaller than 30 Å. Otherwise, Figure 4.6 (d) shows that compression also affected the differential pore volume to micropores. As a result, this micropores improvement also enhances nitrogen adsorption.

Figure 4.6 (b) depicts that BET surface area increased 10 % after the compression of the electrode, evidencing the benefits of this procedure. The surface area's rise is explained by the increase of 32 % in the mesopores and macropores volume and also due to the higher density of E-260P, as presented before [152]. The higher electrode density provided by the compression increased the volume of mesopores and macropores. This improvement can be explained by dispersed particles clustered with other arrangements forming new pathways and clusters [152]. While micropores increased only 6 %, mesopores and macropores rise 32 %. It may happen because larger pores have a smaller mechanical resistance, so they compress and create clusters easier than micropores (i.e., micropore is so tiny that there is not much to be compressed). Several studies, for instance, have been carried out on the effects of compression on AC materials and are aligned with the findings presented above [81,149,152,153]. Beyond that, they also show compression as an essential technique to modify the pore size distribution and improve the surface area of AC materials.

The micropores and mesopores have a higher contribution to the EDL improvement, especially when the ion size matches the micropore diameter [154,155]. As micropores, mesopores, and macropores were affected by the compression and SCs electrochemical behavior is directly driven by dynamics between the ion/electrode interface; is expected that these modifications would drastically change the features of the SC [156,157]. In general, the increase in cumulative volume could improve the total energy stored in the SC based on the higher pore volume available for the EDL formation.

4.3.3 Dynamics of Solvated Ions in Electrodes Under Compression

However, it is insufficient to look out only at the electrode. To adequately evaluate the compression influence in SCs, there is a necessity to investigate the electrolyte effects on the device's behavior. Mainly because of electrolyte features as ion size, solvent concentration, interaction ion/solvent, and interaction ion/electrode drive almost all electrochemical dynamics of the SC [64,158–160]. Besides, the ionic conductivity, the

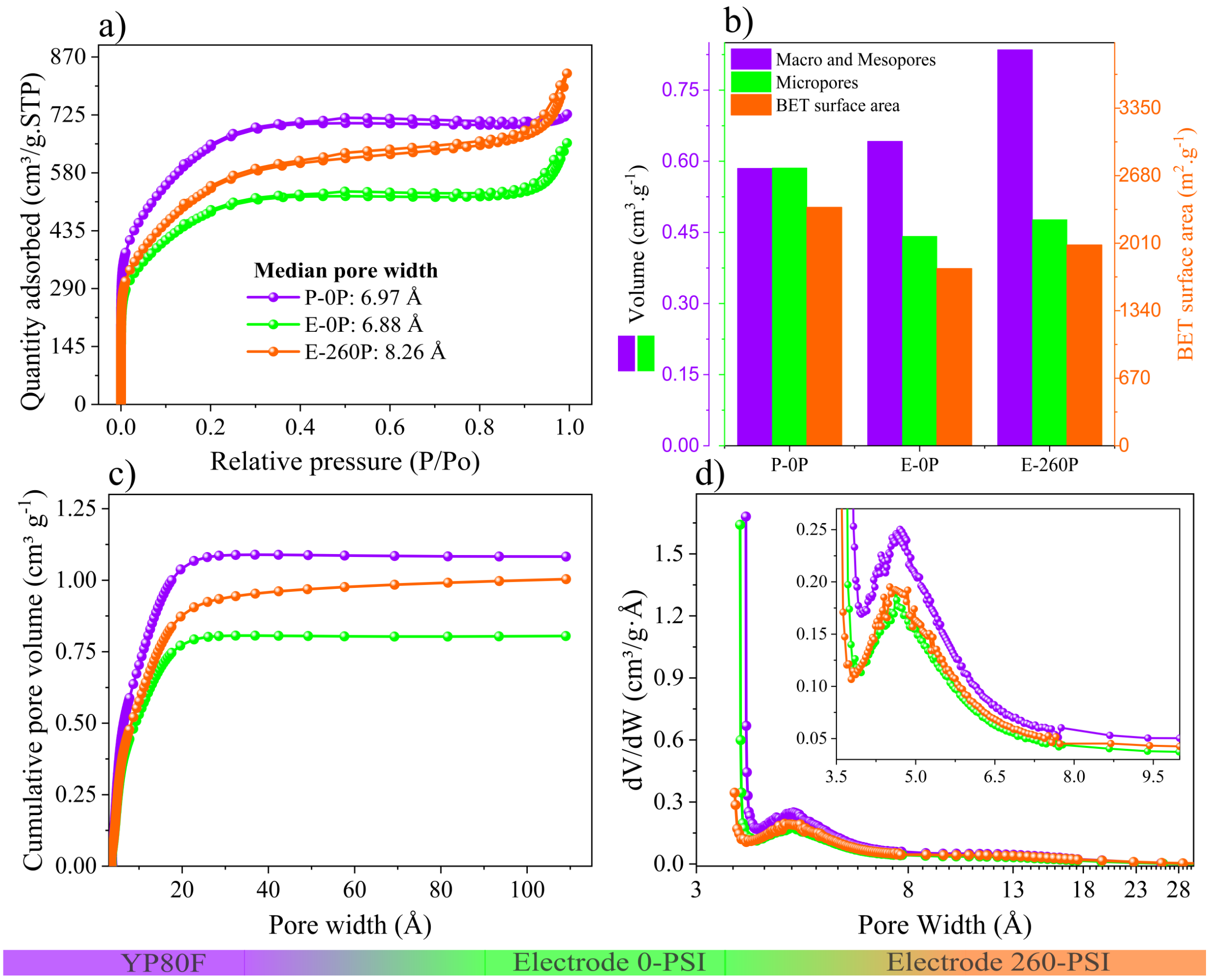

Figure 4.6 – Nitrogen adsorption/desorption isotherms for activated carbon powder YP-80F, electrode without any compression, and an electrode compressed at 260 PSI. (a) Isotherm linear. (b) Brunauer Emmett Teller surface area, the total volume of micropores, and total volume of mesopores and macropores. (c) Horvath-Kawazoe cumulative pore volume. (d) Horvath-Kawazoe differential pore volume.

number of water molecules of solvated ion, and hydrated ion size are features that make the ionic diffusion unique inside the pores [55]. Hence, to investigate if there is a correlation between pore size distribution and ionic adsorption, five aqueous electrolytes with different anions and cations were used: 1m KOH, 1m LiOH, 1m KCl, 1m LiCl and 1m $NaClO_4$. Then several figures exhibit the electrochemical performance of these electrolytes under different compression levels. Here, the influence of pore size distribution on the electrochemical behavior for all electrolytes studied is evidenced.

Figure 4.7 presents the specific capacitance concerning the pressure applied. Here, the values were obtained from a GCD curve at 4 A g^{-1}. More recent evidence highlights the use of compression to improve the capacitance of aqueous electrolytes SCs [43–46]. Beyond that, this study shows the presence of a Point of Maximum Capacitance (PMC) relative to the compression applied to several electrolytes. For LiOH electrolyte, increasing pressure from 60 PSI to 120 PSI rose the capacitance from 13.5 to 35.2 F g^{-1}, representing an increase of 161 %. Nevertheless, from 120 PSI to 260 PSI, the specific capacitance dropped from 35.2 to 29.8 F g^{-1}, representing a decrease of 15 %. The behavior is slight different from the LiCl electrolyte but also follows the same trend. The capacitance increases from 31.4 to 36.7 F g^{-1} (i.e., 17 %) alternating from 60 PSI to 80 PSI and after raising from 80 PSI to 260 PSI, the capacitance declined from 36.7 to 28.1 F g^{-1} (i.e., 23 %).

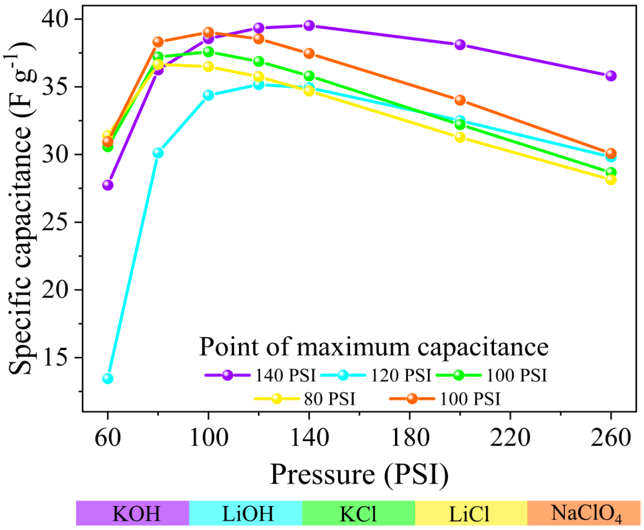

Figure 4.7 – The curve of maximum capacitance at the current density of 4 A g^{-1}.

To analyze the capacitance as a function of compression, the morphological changes (Figure 4.5) and the pore size distribution (Figure 4.6) of the electrode are considered. Initially, the capacitance was improved because clustering the AC's particles reduced the electrolyte resistance into the pores and improved the electrolyte interfacial wettability due to the lower travel distance liquid penetration, as several authors have been investigated and proposed [43–46]. About the drop seen in capacitance, recent evidence has highlighted a reduction in capacitance (i.e., more than 80 %) due to excessive compression of porous electrodes [79, 80, 82, 153].

Two hypotheses fit very well to explain the fall in capacitance seen in Figure 4.7 after the PMC. Firstly, as proposed by Gourdin and co-workers, excessive compression turn micropores inaccessible, reducing the ions' diffusion [82]. So, based on the reduction of micropores smaller than 4 Å seen in Figure 4.6 (b), it is reasonable to infer that the same process is happening here. Secondly, based on the multiphase lattice Boltzmann method, several studies have presented that compression alters wettability and decreases the effective area available to the electrolyte coming inside the AC's pores as the porosity falls [153, 161–163]. So, based on the porosity reduction presented in Figure 4.5, the fall in capacitance can also be expected by the lower available sites to ions coming inside and forming the EDL, especially after the PMC.

Table 4.1 – Pauling ionic radii, hydrated ion size, number of water molecules in this shell, and ionic conductivity values.

Ion	R_p size [Å]	R_h size [Å]	n_w	S [S cm^2 mol^{-1}]
Li^+	0.69$^{a)}$	3.82$^{b)}$	5.2$^{a)}$	38.69$^{b)}$
Na^+	1.02$^{a)}$	3.58$^{b)}$	3.5$^{a)}$	50.11$^{b)}$
K^+	1.38$^{a)}$	3.31$^{b)}$	2.6$^{a)}$	73.50$^{b)}$
OH^-	1.33$^{a)}$	3.00$^{b)}$	2.7$^{a)}$	198.00$^{b)}$
Cl^-	1.81$^{a)}$	3.32$^{b)}$	2.0$^{a)}$	76.31$^{b)}$
$ClO4^-$	2.50$^{a)}$	3.38$^{b)}$	1.4$^{a)}$	67.30$^{b)}$

Source: $^{a)}$from ref. [164] $^{b)}$from ref. [36]

Based on Table 4.1, it is presented how the anions and cations from electrolytes behave in different pore size distributions. Initially, it is observed from Figure 4.7 that the electrolytes formed by the anions Cl- and ClO_4- have a PMC reached until 80 PSI while electrolytes composed with the anion OH- have a PMC up to 140 PSI. More recent experimental and computational evidence suggests that this abnormal increase in capacitance happens because the highest energy storage in the EDL occurs when the pore width and the ion size have proximity same dimension, forming a superionic state (that is, theory for ionic liquid) [46–48, 148, 149].

In complement, our results point to an unexpected result because some experimental and theoretical studies have presented that the superionic state happens when the pore size matches the ion size for ionic electrolytes [133, 165–170]. Nevertheless, to aqueous electrolytes and AC electrodes, the results indicate that the superionic state happens when the pore size matches the hydrated ion size. The schematic presented in Figure 4.8 clarifies the three ion dynamics conditions inside the AC's pores concerning the compression applied. Initially, Figure 4.8 (a) presents how the adsorption occurs when the pore size is wider than the hydrated ion size. In this state, micropore size was not significantly changed by the compression applied. Then Figure 4.8 (b) demonstrates the superionic state when the pore width has almost the dimension of the hydrated ion after compress the AC. At least, Figure 4.8 (c) exhibits how the ions lose their solvation shell to come inside pores smaller than their hydrated ion size due to excessive compression of the AC's electrode. As a result, the match between the ion and pore width only happened with at least 120 PSI to the KOH and LiOH electrolytes due to the small, hydrated ion size from OH-. The compression reduces the micropores until they have approximately the dimension of the hydrated ion size, which is the best condition to form the EDL.

Likewise, the electrolyte KOH presents the highest PMC because of a minor combination of anion and cation hydrated ion size. In contrast, the LiCl electrolyte shows the lowest PMC due to their highest combination of hydrated ions size (Figure 4.7). As presented in Figure 4.7, it is observed that electrolytes composed with the anion OH-

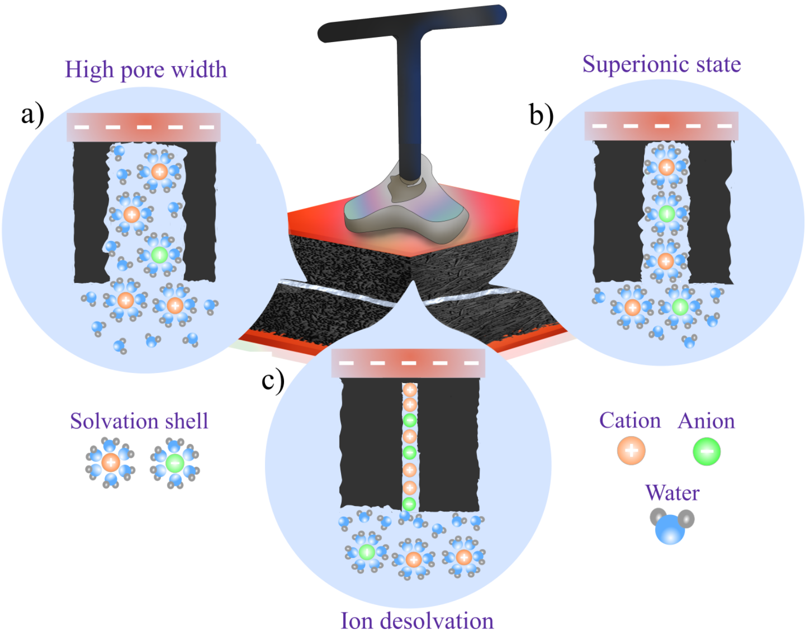

Figure 4.8 – Ion's adsorption in the porous structure. (a) High pore width concerning hydrated ion size. (b) Demonstrate the superionic state that appears when the pore width approximates the dimension of the hydrated ion size. (c) Represents the ion's desolvation process to come inside tiny pores.

promoted a slower fall in capacitance after reach the PMC. So, it is expected that the anion OH- has a higher facility to access the smallest pores and improves the EDL. That is highly associated with its higher ionic conductivity and smaller ion size (Table 4.1).

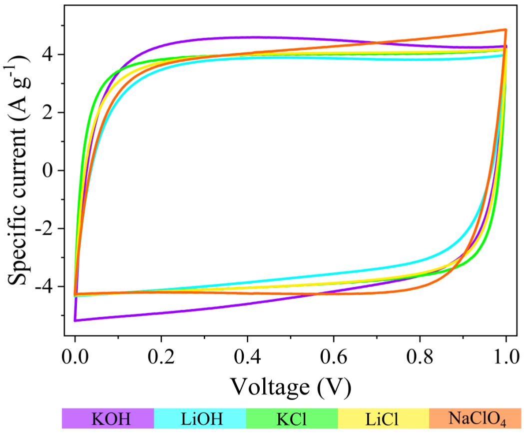

Figure 4.9 – Cyclic voltammetry curves at a scan rate of 100 mV s^{-1} to the highest capacitance found according to pressure applied.

Figure 4.9 shows the almost rectangular CV curves at 100 mV s^{-1} and 1 V of WVW. However, it remains rectangular even at higher scan rates (Figure B.1 (d) to Figure B.5 (d)). A high scan rate is possible due to a reduction in the resistive portion of the time constant (i.e., $\gamma = RsC$), improved by the electrode's correct compression, where Rs is the system's resistance and C the capacitance.

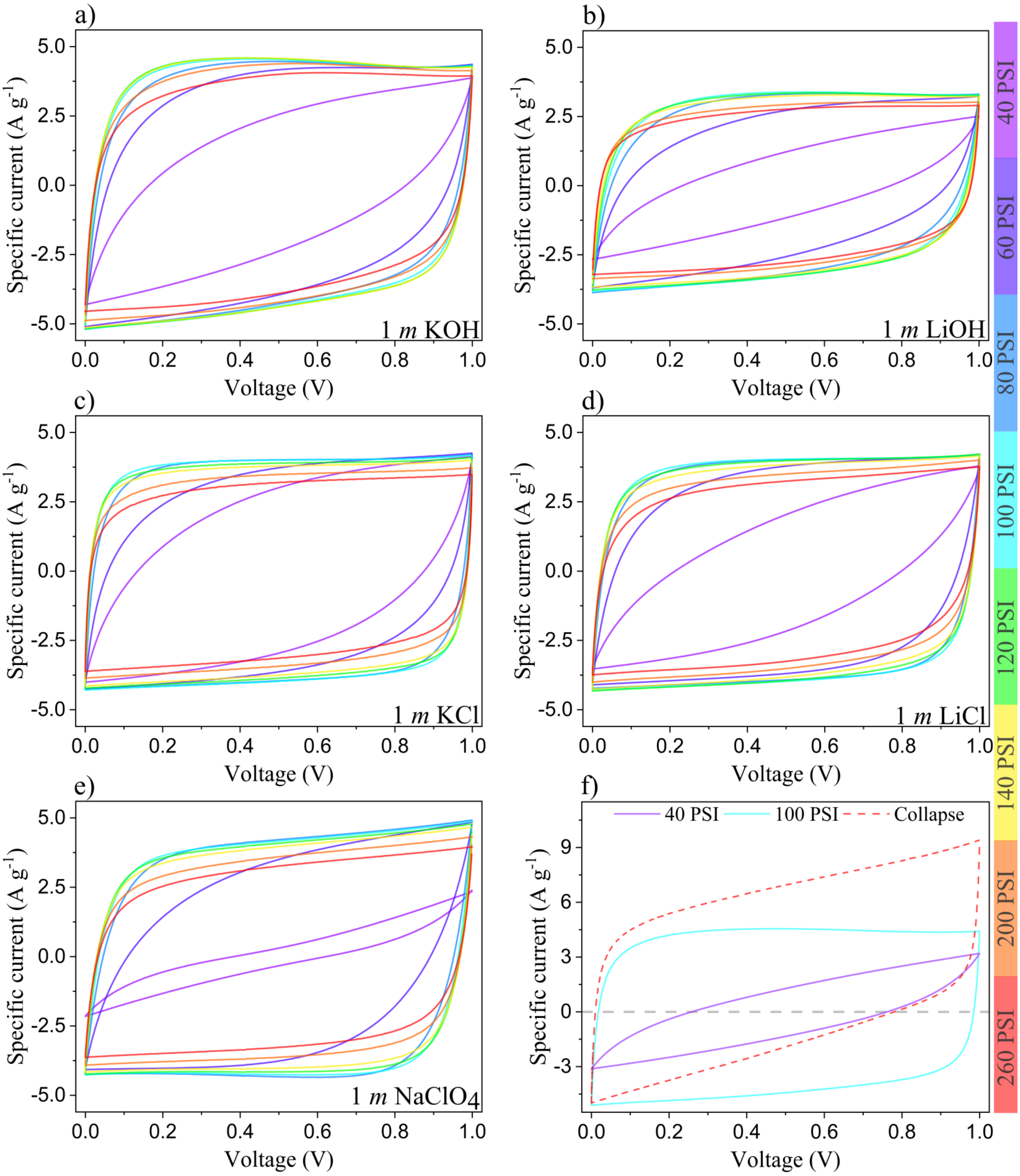

Figure 4.10 – Cyclic voltammetry curves at a scan rate of 100 mV s^{-1} and 1 V for the following electrolytes (a) KOH, (b) LiOH, (c) KCl, (d) LiCl, and (e) $NaClO_4$ at different levels of compression. (f) Cyclic voltammetry curves measures when the electrodes short-circuit among them, usually after applying more than 260 PSI.

Figure 4.10 (a-e) depicts the shapes of CV curves at 100 mV s^{-1} from 40 PSI to 260 PSI to all electrolytes. Initially, an elliptic-like CV curve can be seen at low pressures from 40 to 60 PSI because the resistive portion is much higher than the capacitive (i.e., $Rs \gg C$) due to the low contact resistance and dispersion of the electrode particles. At pressures higher than the PMC, a flatness in CV shapes is caused by the specific capacitance reduction shown in Figure 4.9. In addition Figure 4.10 (f) reflects the SC's collapse seen as a substantial asymmetric increase in the CV's current due to an excessive pressure applied over the cell that causes a short circuit among the electrodes [82].

Figure 4.11 highlights the effect of pressure on the EDR extracted from GCD. As summarized by Mei and co-workers [133] the EDR shows the sum of all internal resistances as (*i*) bulk electrolyte resistance, (*ii*) the electrode resistance, (*iii*) the electrolyte resistance in the pores of the electrode, (*iv*) resistance between the electrode/current collector, (*v*) nonuniform electrode pore size and (*vi*) roughness. So, in this case, at 60 PSI, the EDR is high due to the low contact resistance between the electrode/current collector and the high electrolyte resistance in the electrode pores. However, the EDR started to decrease exponentially until 140 PSI, where they reached a plateau region. These findings show that no more pressure is necessary to reduce the EDR.

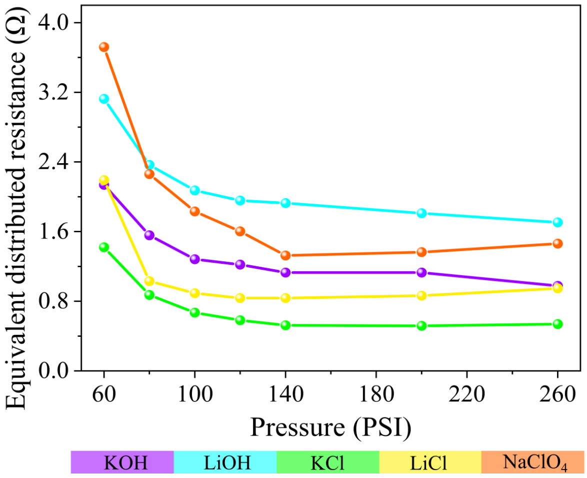

Figure 4.11 – Equivalent distributed resistance extracted from galvanostatic charge and discharge measurements.

About the ions features concerning the EDR, it is possible to see that electrolytes with the anion Cl- have a lower EDR. The EDR considers the electrolyte resistance in the electrode's pores [133]. So probably as the LiOH electrolyte has an average EDR of 1.96 Ω and KCl 0.58 Ω, some feature favors the ion K+ and Cl- to falls the EDR. Based on that, it is possible to infer a correlation between the ions of low EDR with the low number of water molecules on the ion's solvation shell. It appears to happen because ions with a lower amount of water molecules on the solvation shell have a higher facility to lose the water molecules of their solvation shell to come inside in very tiny pores. Another hypothesis raised is related to the Pauling ionic *radii*, mainly because ions will access the deeper pore structures if it is small. So, the further ion diffusion inside the pore structure, the higher the ion's resistance [73]. Consequently, KCl has the lowest EDR due to its combination of anions and cations of the highest Pauling ionic radii and LiOH for the opposite reason (Figure 4.11).

As seen in Figure 4.12, the rise in ESR suggests that the separator has also been affected by the compression. Mainly because more recent evidence highlights that porosity and ionic conductivity of separators are reduced after apply compression [171–173]. So, as the ESR is related to the bulk electrolyte, the low ionic conductivity of the separator difficult the ion diffusion on the bulk electrolyte; thus, the ESR rises after compressing the cell. Surpassing the separator effects, the electrolyte between the electrodes also leaks, creating some dry spaces between electrode and separator [79, 85], as seen in Figure 4.13 (a-b). As a result, ions diffusion does not happen anymore in these spaces, raising the ESR because it is directly proportional to the available area. So, in addition to micropore reduction and low wettability of the AC, the electrolyte leakage also explain why the capacitance starts to drop after reaching the PMC (Figure 4.7). The bulk electrolyte is highly related to the electrolyte's ionic conductivity. For this reason, it is seen that the KOH electrolyte has the lowest ESR to all compression levels.

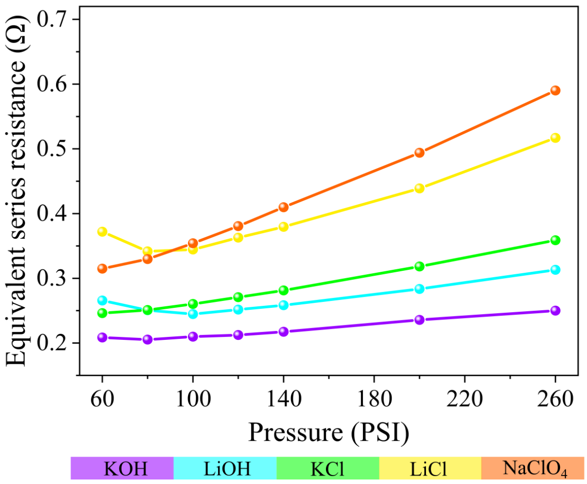

Figure 4.12 – Equivalent series resistance obtained from electrochemical impedance spectroscopy measures to the frequency of 100 kHz.

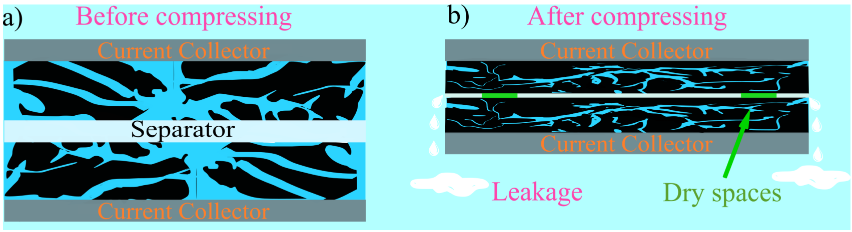

Figure 4.13 – (a) Cell assembled without any compression. (b) Cell assembled with a high compression level causes an electrolyte leakage

Figure 4.14 (a-b) highlight that the point of Maximum Specific Energy (MSE) does not match with the point of Maximum Power Transfer (MPT) concerning the applied pressure to all electrolytes. For example, for the LiCl electrolyte, the MSE is reached by applying 80 PSI. In contrast, the MPT is reached only after 120 PSI. It is essential to highlight that prioritizing MSE or MPT can provide diverse Ragone plots [174], as seen in Figure 4.15. So, the manufacturers and the academic community need to select the most important feature between MSE and MPT before manufacturing the SC to produce devices more adequate to a required application. Figure 4.16 shows the best way to identify the better MPT and MSE points according to the applied pressure.

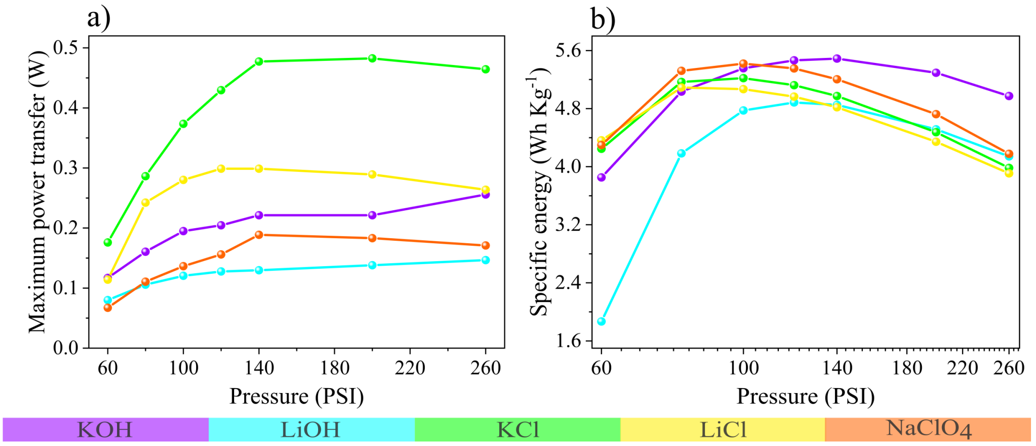

Figure 4.14 – (a) Maximum power transfer calculated with equivalent series resistance from galvanostatic charge/discharge and 1V of window potential. (b) Specific energy calculated with capacitance and 1V of window potential.

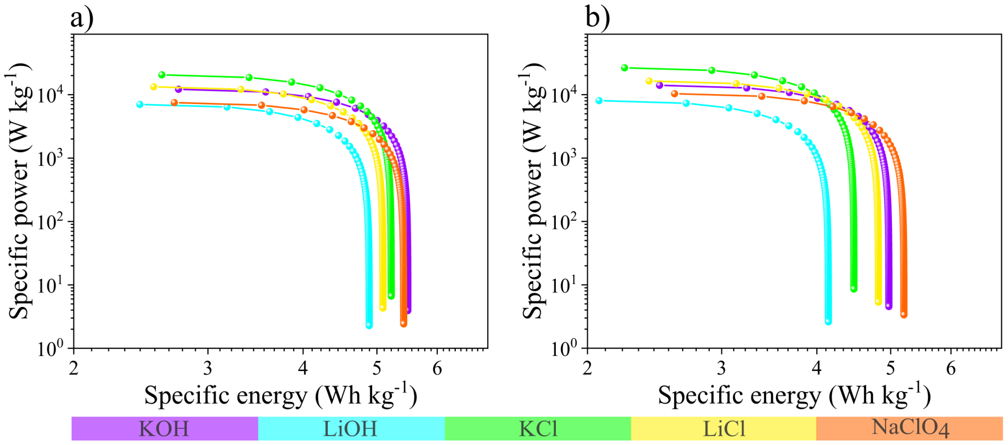

Figure 4.15 – Ragone Plots. (a) Concerning the point of maximum specific energy and (b) regarding the point of maximum power transfer.

To assess if there is electrode deformation and how it can change the SCs electrochemical behavior, Figure 4.17 presents a comparison among compressed and decompressed cells. Firstly, the cell was compressed from 40 to 260 PSI. Secondly, the cell was decompressed until 40 PSI after reach 260 PSI. With that, pieces of evidence can be accessed inferring the electrode suffered a plastic deformation. This scenario can be seen in Figure 4.17 (a-e). After compress the cell and return to the initial state, the CV curves strongly differed at 40 PSI. It fits very well with the nitrogen adsorption/desorption isotherms findings, the AC's materials only presented diverse isotherms results because the samples did not return to their initial state after release the compression (Figure 4.4 (f)).

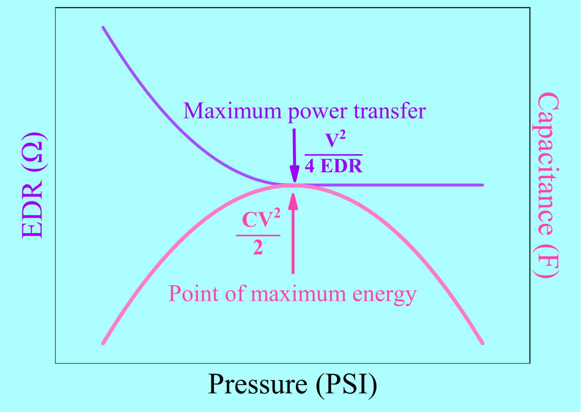

Figure 4.16 – Theoretical behavior of capacitance and equivalent distributed resistance of an supercapacitor under compression.

Besides that, is seen to all electrolytes that decompressed states have straiter CV shapes. It means that the AC material also suffered an elastic deformation for not returning to PMC shape. So, to achieve the PMC during the SC's manufacturing is fundamental to compressing the electrodes before the cell assembly. In addition, and not less important, it is necessary to compress the cell continuously with a correct pressure.

Figure 4.18 shows the Nyquist plots obtained at different compression levels. As observed, the Nyquist plots also represent a clear correlation between the frequency domain responses and the compression applied. The most remarkable results emerged from the High Frequencies (HF) (e.g., f > 10 Hz) and Low Frequencies (LF) (e.g., f <= 10 Hz) domain analysis. The semi-circles seen in Figure 4.18 (a-e) are usually interpreted as a Charge Transfer Resistance (RCT) due to functional groups' presence over the electrode surface or unwanted faradaic reactions [175]. However, some authors suggest that it is most reasonable to occur due to interfacial impedances between the current collector/electrode [63]. For our best understanding, this interfacial impedance hypothesis fits much correctly with the findings.

As seen in Figure 4.18 (a-e), the interfacial impedance reduced 289 % and 283 % after increasing pressure from 60 PSI to 260 PSI to the $NaClO_4$ and KCl electrolytes. Moreover, one can be observed that after applying 140 PSI, the semi-circle diameter almost did not change with compression. It suggests that the interfacial contact between the current collector/electrode occurs almost completely. The residual semi-circle seen in HF (Figure 4.18 (a-e)) is attributed to the electrolyte resistance in the electrode's pores. On the other hand, the Nyquist plot of a typical EDL formation, i.e. in the absence of water-splitting or undesired faradaic reactions, is represented by a vertical line parallel to the imaginary axis (i.e., $-Z_{img}$) [32]. At LF domain, the Constant Phase Element (CPE)) can be used in the canonic model for fitting the 'frequency dispersion phenomenon' related to rough/porous electrodes [32]. In other words, the impedance $Z_{cpe} = 1/Y_0(j\ 2\pi f)^n$ must have a phase angle higher than -83° (i.e., $n > 0.9$) to represent a good EDL's

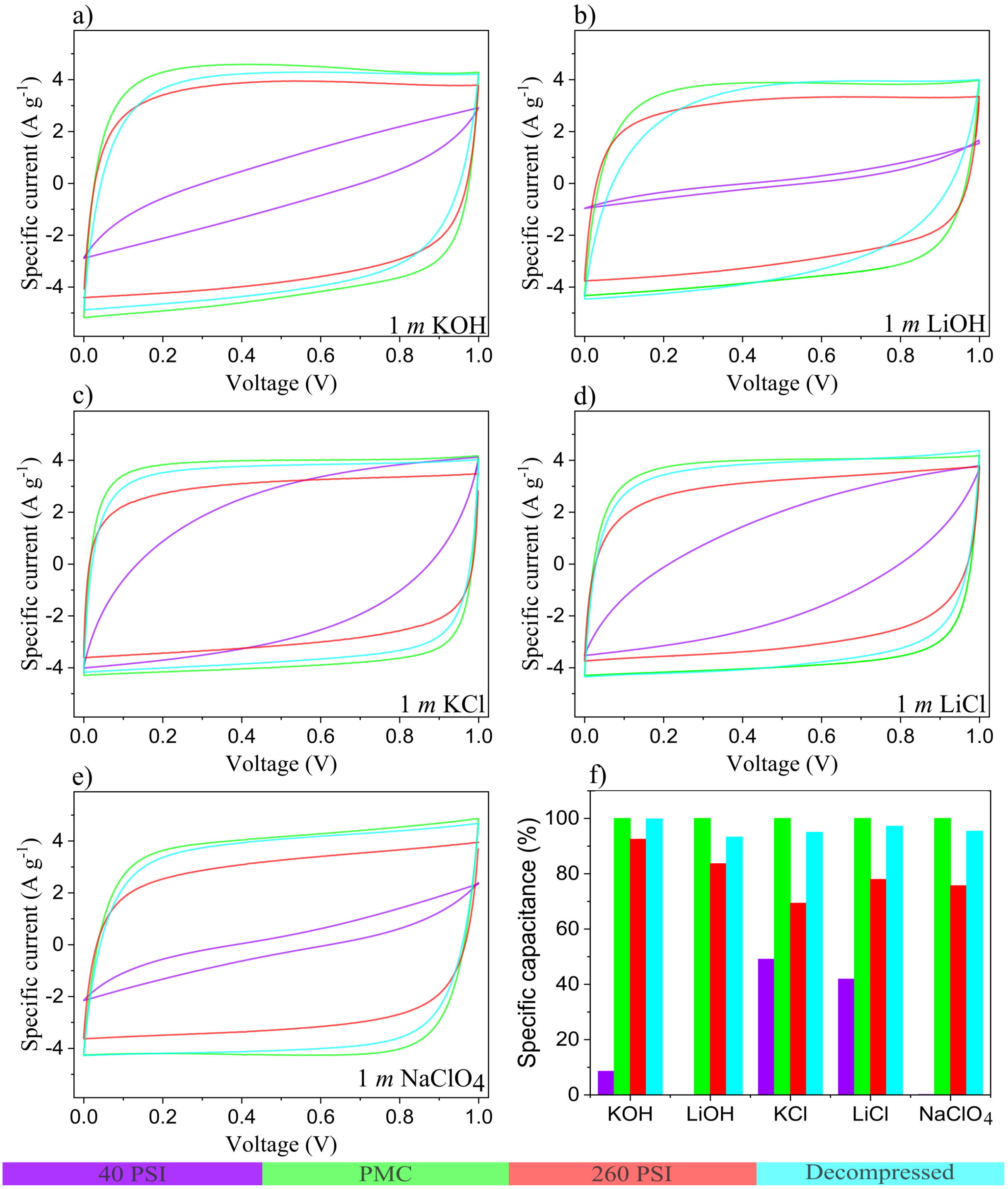

Figure 4.17 – Cyclic voltammetry curves at a scan rate of 100 mV s^{-1} for 40 PSI, the point of maximum capacitance, 260 PSI, and decompressed to 40 PSI after applying 260 PSI for the following electrolytes (a) KOH, (b) LiOH, (c) KCl, (d) LiCl, and (e) NaClO$_4$. (f) exhibits the percentage-specific capacitance for all electrolytes at a current density of 4 A g^{-1}. The percentages are related to the point of maximum capacitance of each electrolyte.

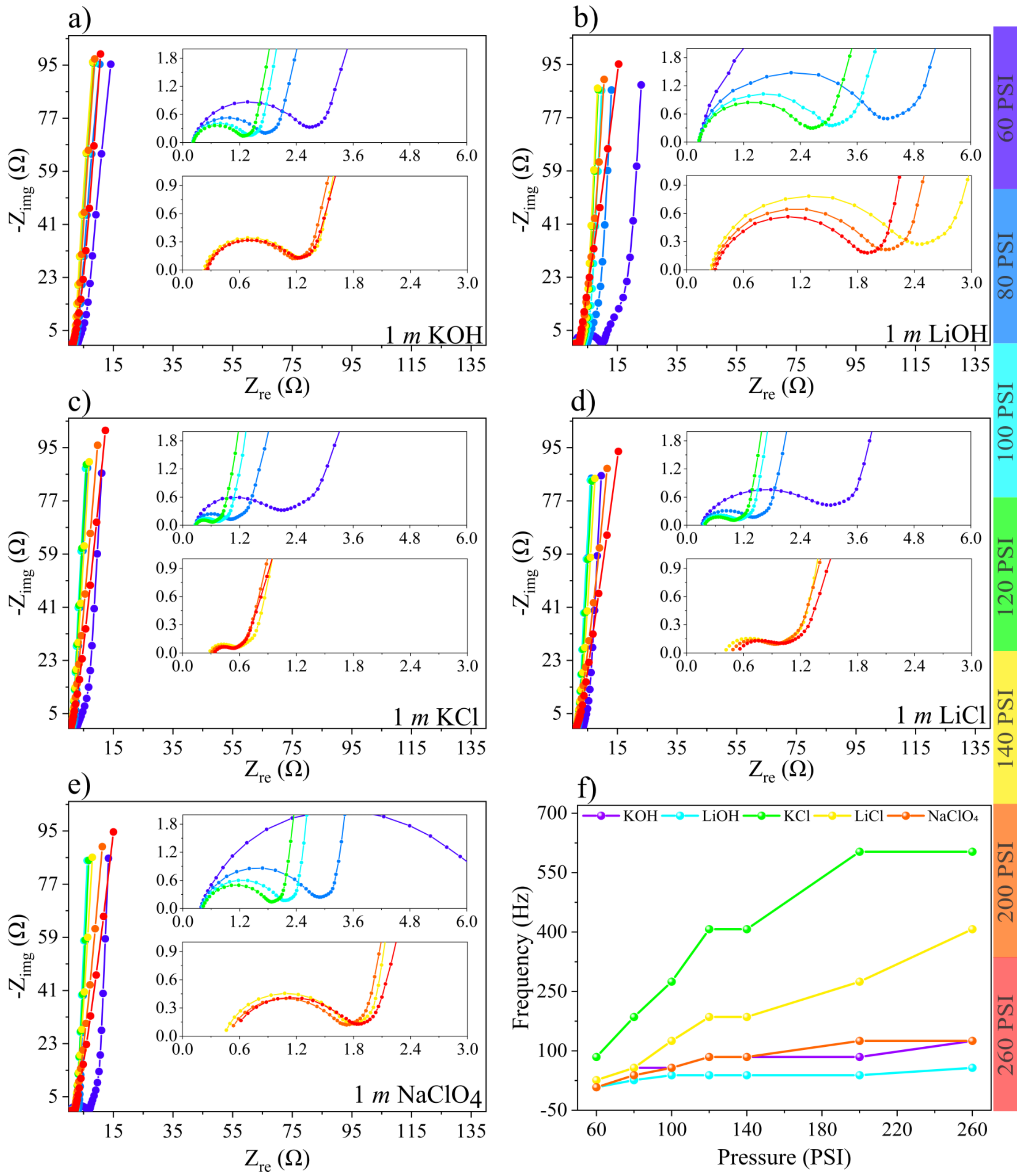

Figure 4.18 – Electrochemical impedance spectroscopy measures in the frequency range of 10 mHz to 100 kHz for the following electrolytes a) KOH, b) LiOH, c) KCl, d) LiCl, and e) $NaClO_4$. f) Knee frequency extracted from Nyquist plots.

formation [32, 77]. As presented in Figure 4.18 (a-e), the phase angles decreased after applying compression to all electrolytes. The phase angle decreases from 87° ($n = 0.97$) to 83° ($n = 0.92$) and 87° ($n = 0.97$) to 82° ($n = 0.91$) after increase pressure from 60 PSI to 260 PSI for LiOH and LiCl electrolytes, respectively. It supports the fact that the morphological change of AC electrodes difficult the ionic penetration into pores at LFs conditions.

Figure 4.18 (f) evidences the frequency in which the EDL starts to be formed massively, usually called “knee frequency”. Li and co-workers have demonstrated the possibility of improving the knee frequency of aqueous supercapacitors compressing the single-walled carbon nanotubes electrode [44]. Here is seen the same possibility. The knee frequency extracted from Nyquist plots (Figure 4.18 (f)) shows an improvement to all electrolytes. Its improvement occurred mainly to the KCl and LiCl electrolyte reaching 650 Hz and 400 Hz each other at 260 PSI. So, the higher knee frequency increases the range of possibilities of SC applications, mainly to high-frequency electronic devices. It is necessary to highlight that the knee frequency also is driven by the electrolyte features. In this case, the higher frequency reached by the anions Cl- and ClO_4- is caused by the number of water molecules. It is propose that the lowest number of water molecules in the shell turns easier for these anions to come inside the electrode’s pores. So, the time required to access the pore’s structures is faster. It also suggests that ions with many water molecules have difficulty losing their solvation to access the deeper pore structure.

4.4 Concluding Remarks

This chapter described how the compression modified the pore size distribution of an AC electrode and the ion’s dynamics into the pore structure regarding several electrochemical measures that helped explain the correlations in operation conditions. The results showed that the state of a maximum energy storage point was achieved when the electrode was compressed until the micropores match in dimensions with the electrolyte’s hydrated ion size. The compression form a superionic state that increases the capacitance. The level of compression required is different according to the electrolytes used. KOH electrolyte that has the lowest combination of cation and anion size required the highest electrode compression.

In contrast, the LiCl that contains the largest hydrated ion size required a lower level of compression to achieve a superionic state that provided the maximum energy storage. The Pauling ionic *radii*, hydrated ion size, number of water molecules in the shell, and ionic conductivity are highly associated with the SC’s performance and the electrode pore size distribution. The findings might not be generalized to all kinds of porous materials as carbon nanotubes or graphene because these materials’ deformation features are entirely different from the AC. So, the study provides considerable insight into the manufacturing of activated carbon SCs. For some electrolytes, the MSE is not achieved at the same electrode’s compression as MPTs. So, there is the need to define the essential feature between MSE and MPT to prioritize during the SC’s compression and manufacturing.

5 Sodium Electrolytes Supercapacitors at Low Temperatures

SCs using concentrated aqueous-based electrolytes can work at low temperatures due to their intrinsic properties, such as higher FPD and robustness. Besides the traditional organic- and aqueous-based (salt-in-water) electrolytes used in SCs, WISE sodium perchlorate electrolytes offer high FPD, non-flammability, and low-toxicity conditions, allowing the fabrication of safer, environmentally friendly, and more robust devices. For the first time, this work reports a comprehensive study regarding a WISE system's charge-storage capabilities and physicochemical properties under low-temperature conditions ($T < 0$ °C) using mesoporous carbon-based electrodes. The effect of temperature reduction on the electrolyte viscosity and electrical properties was investigated using different techniques and the in-situ (or operando) Raman spectroscopy under dynamic polarization conditions. The cell voltage, equivalent series resistance, and specific capacitance were investigated as a function of the temperature. The cell voltage (WVW) increased $\sim$ 50%, while the specific capacitance (C_{spec}) decreased $\sim$ 20% when the temperature was reduced from 25°C to -10°C. As a result, the specific energy ($E = C^*V^2/2$) increased $\sim$ 100%. Therefore, low-temperature WISEs are promising candidates to improve the energy-storage characteristics in SCs. Remembering that this chapter reproduces the published scientific paper in the Journal of Energy Chemistry, "*Boosting energy-storage capability in carbon-based supercapacitors using low-temperature water-in-salt electrolytes*" [93].

5.1 Experimental Procedures

5.1.1 Electrode Preparation

The mesoporous carbon BKP electrodes used in the symmetric aqueous-based supercapacitor were obtained from as-prepared MWCNTs model Ctube-120 from CNT Co. Ltd. (South Korea). The electrode (BKP) preparation method was presented in detail elsewhere [176]. In brief, a suspension (1:10 wt%) containing MWCNTs and sodium dodecyl sulfate from Sigma-Aldrich® (CAS-No: 151-21-3) was prepared using 0.2 dm^3 of deionized water (18 MΩ cm). Afterward, the suspension was sonicated and filtered using a model SL-61 vacuum pump from SOLAB for 45 min. This process was completed in 3 steps of 15 min. Finally, a filtering system with a controllable volumetric flow rate was employed to produce the BKP disks. Each electrode has a 10-mm diameter and a carbon mass of 2.5 mg.

5.1.2 Viscosity and Conductivity of Sodium Water-In-Salt Aqueous Electrolyte

The viscosity of the electrolytes was measured using a viscometer model SNB-1A from MesuLab Instruments Co. Ltd. (Guangzhou). The conductivity was measured by a conductivity probe K10 connected to an Arduino Uno Rev3 microcontroller board from Arduino® and calibrated with a standard solution (1 M of KCl from Sigald®, CAS-No: 7447-40-7). A beaker was boiled for 1 h a day before taking the calibration measurements to avoid any contamination caused by sodium or calcium remaining in the glassware. In addition, to avoid the formation of carbonic acid (H_2CO_3) due to the presence of carbon dioxide (CO_2) in the atmosphere, the electrolyte was sonicated and bubbled with pure nitrogen gas using a beaker with a Parafilm® layer on top to avoid as much as possible the presence of CO_2 during the measurements. Concerning the acquisition of the viscosity and conductivity at different temperatures, the procedure performed to avoid carbonic acid and beaker contamination was repeated. Before each measurement, 50 cm^3 of the 17-m $NaClO_4$ (Sigald®, CAS-No: 7601-89-0) solution was thermostated at -12°C and stabilized for 12 h.

5.1.3 Raman Spectra Measurements

The Raman spectra of the electrolyte at different temperatures were acquired with a Renishaw inVia spectrometer. The spectrometer parameters were set to provide reliability and quick measurements to avoid temperature changes during the experiment. As a result, we used a 785-nm wavelength excitation laser and a 50X objective lens. Experiments were carried out with 1 accumulation and 10 s of exposition, resulting in less than 1 min of measurement time. The laser power was adjusted to 10% to avoid temperature changes and solvent evaporation. The equipment was calibrated using an internal silicon pattern (520.5 cm^{-1}).

A particular experimental setup was adopted to ensure isothermal conditions. To reach the lowest temperature, a sealed glass bottle was filled with the electrolyte, degassed, and maintained overnight in a refrigerator at -12°C. After that, the electrolyte sample was removed for analysis. The sample was introduced in a small metal container immersed in an ice bath to keep the electrolyte temperature constant inside the spectrometer. The temperature was monitored using a digital thermocouple. A natural cooling process was adopted for the studies at other (higher) temperatures ($T > -12°C$).

5.1.4 Electrochemical measurements

Electrochemical experiments were performed using a standard CR2032 coin cell containing the BKP electrodes separated by a mesoporous membrane model TF4030 ($\epsilon =$ 30 µm and porosity of 73% - Nippon Kodoshi Co.) soaked with a 17-m $NaClO_4$ aqueous solution. Electrochemical data were collected at different temperatures (e.g., -10, 0, 10, and 25°C). The electrochemical techniques used were CV, GCD, EIS, and SPSC.

All experiments were accomplished using a model BCS-128 potentiostat from Biologic®. The EIS experiments were carried out at different d.c. voltages in the range of 1.2 to 1.8 V. Sinusoidal signals with a small amplitude of 10 mV (peak-to-peak) were applied in the frequency range of 10 kHz to 10 mHz. The CV measurements were performed using scan rates in the interval of 1 to 200 mV s^{-1} and different voltage windows in the range of 1.2 to 1.8 V. The GCD experiments were performed at gravimetric currents in the 0.016 to 15 A g^{-1} interval.

The specific capacitance was determined using Equation (4.1). Based on the specific capacitance, it is possible to calculate the specific energy by Equation (4.2) and the corresponding maximum power by Equation (4.3).

5.2 Electrochemical Responses

Figure 5.1 to Figure 5.5 show the electrochemical findings obtained from different techniques as a function of the electrolyte temperature used to identify the best WVW, as recently proposed in the literature [77]. Figure 5.1 shows the CVs from 1.2 to 1.8 V at 10 mV s^{-1} at different temperatures. For the different temperatures, the CV findings showed an almost ideal Electric Double-Layer Capacitor (EDLC) behavior characterized by symmetric rectangular voltammetric profiles.

It was verified that the upward anodic current following an exponent trend is close to the anodic vertex (limit) voltage Anodic Vertex Voltage (AVV), which is characteristic of the onset of the electrolyte decomposition. Basically, the influence of temperature and applied potential (or voltage) on faradaic reactions is dictated by the well-known Butler-Volmer's phenomenological model based on Transition State Theory (TST) proposed by Eyring. This theory establishes the dependence of the heterogeneous rate constant for faradaic reactions on the activation parameters, temperature, and overpotential by

$$k = A * exp\left(\frac{\Delta G^o}{RT}\right), \tag{5.1}$$

where A is the Arrenhius's pre-exponential factor, ΔG^o is the Gibbs' activation energy for the electron transfer reactions, R the universal gas constant and T the absolute temperature [177]. As seen from Equation (5.1), for a given overpotential (e.g., AVV), the electron transfer rate for water-splitting decreases with temperature reduction. Therefore, the use of WISE at reduced temperatures can permit the enlargement of the working voltage window for SCs.

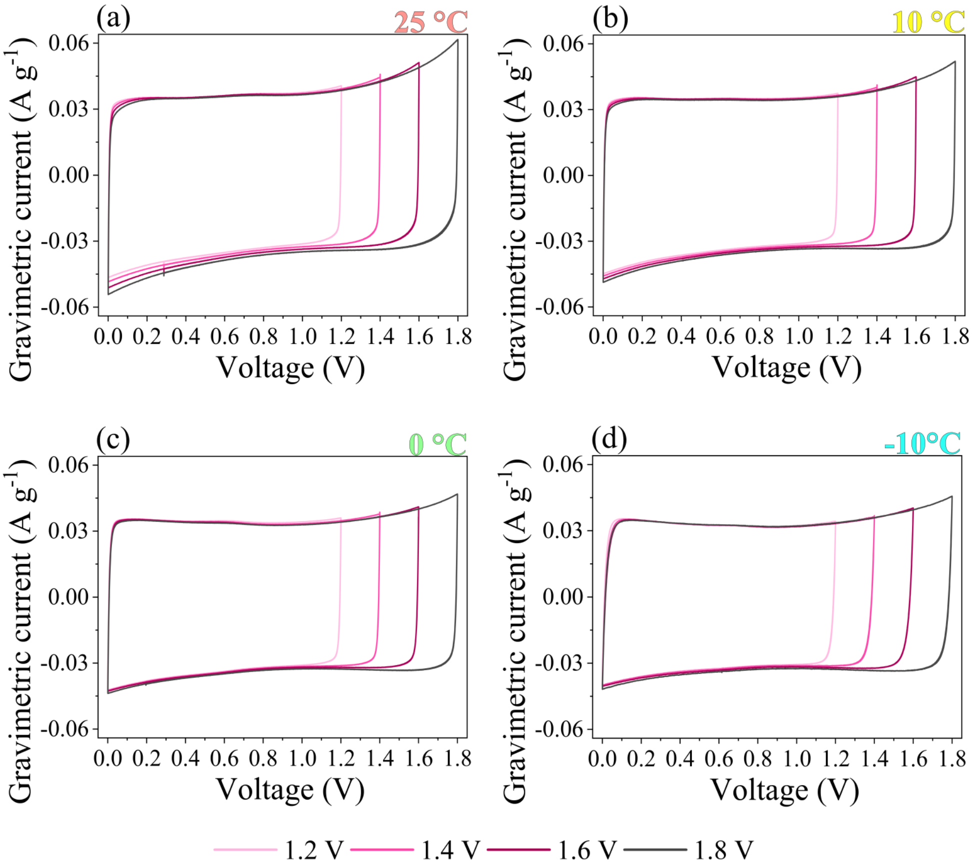

Figure 5.1 – Cyclic voltammetry performance at several voltages (i.e., 1.2 V, 1.4 V, 1.6 V, and 1.8 V) and varied temperatures. Figure adapted from [93].

Overall, these findings revealed an improvement in the capacitive voltage range (or working voltage window for SCs) at low temperatures since the onset of the water-splitting reaction was displaced towards more positive voltages [178]. It means, increasing the WVW to 1.6 V at 10°C and 1.8 V at 0°C and - 10°C (Figure 5.1 (b, c and d)). In addition, Figure 5.2 presents the low scan rate CVs (e.g., 1 mV s^{-1} and 1.8 V) for the different temperatures. It is possible to notice the difference in the current increase at the AVV as a function of the temperature. In addition, Figure 5.3 shows the CVs for the best WVW at different scan rates. As can be seen, in all cases, the quasi-rectangular voltammetric profile was verified.

These findings were used to confirm the onset of water-splitting close to the reversal (vertex) voltages since at low scan rates ($\nu \rightarrow 0$), the faradaic current (I_f) under kinetic control ($I_f \cong I_0.\exp(\alpha F\eta_s/RT)$) is maximized over the capacitive current ($Ic = C_{edl}.\nu$, where ν is the scan rate). In the former equation (Butler-Volmer's model under the high-field approximation), one has that I_0 is the exchange current measured at $\eta_s \rightarrow 0$, while α (≈ 0.5) is the charge-transfer coefficient. The other symbols have their usual meaning. Unfortunately, several literature reports evaluated the WVW at high scan rates, leading to misleading findings. In these cases, the faradaic current due to water-splitting is commonly suppressed by the capacitive electrode response.

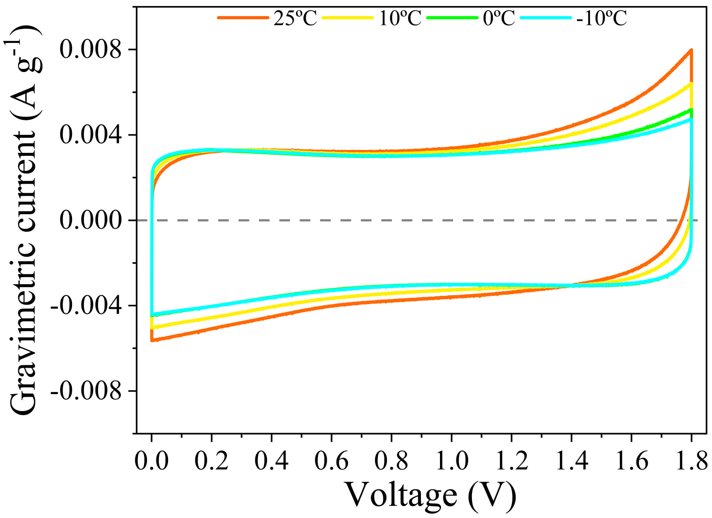

Figure 5.2 – Cyclic voltammetry measurements at 1 mVs^{-1} and 1.8 V, for different temperature condition. (a) at 25°C, (b) 10°C, (c) 0°C and (d) - 10°C. Figure adapted from [93].

The EIS technique can yield important information for the study of SCs. The main parameters commonly obtained from the impedance experiments are the overall ohmic resistance (e.g., electrolyte, electrode, and current collector), denoted as equivalente series resistance (R_{esr}), the electrical double-layer capacitance (C_{edl}), and the frequency dispersion at high frequencies which gives information about the porous electrode behavior (De Levie's model) [133].

In this sense, impedance measurements were performed at the same voltage (WVW) considered in the CV experiments to permit a comparison between the different techniques. In addition, the analysis of the low-frequency data gives information regarding the presence of water-splitting, i.e., deviations from the linearity verified in the complex-plane plots at low frequencies commonly indicate the presence of water-splitting. In this case, the impedance response is no longer purely capacitive since a charge-transfer resistance (R_{ct}) related to the faradaic process appears in parallel to the EDL charging process.

Nyquist plots for the WISE-based SCs at different temperatures are shown in Figure 5.4 (a, b, c and d). Generally, well-behaved SCs are characterized by low-frequency phase angles (φ) greater than ca. -83°, i.e., from the perspective of the CPE approach used to represent the frequency dispersion phenomenon intrinsic to solid electrodes, where $Z_{cpe} = 1/Y_0\,(j\omega)^n$, a good SC behavior is associated with $n > 0.90$ since in these conditions $Y_0 \approx C_{edl}$. The unit of an actual capacitance is the farad (F $=$ s Ω^{-1}), while in the case of a CPE, one has the fractal unit given by F s^{n-1}.

The conversion of Y_0 to C$_{\text{edl}}$ can be achieved using the 'Brug-Sluyters' formula. Figure 5.4 (a) shows well-behaved impedance data with a low-frequency phase angle of -86°

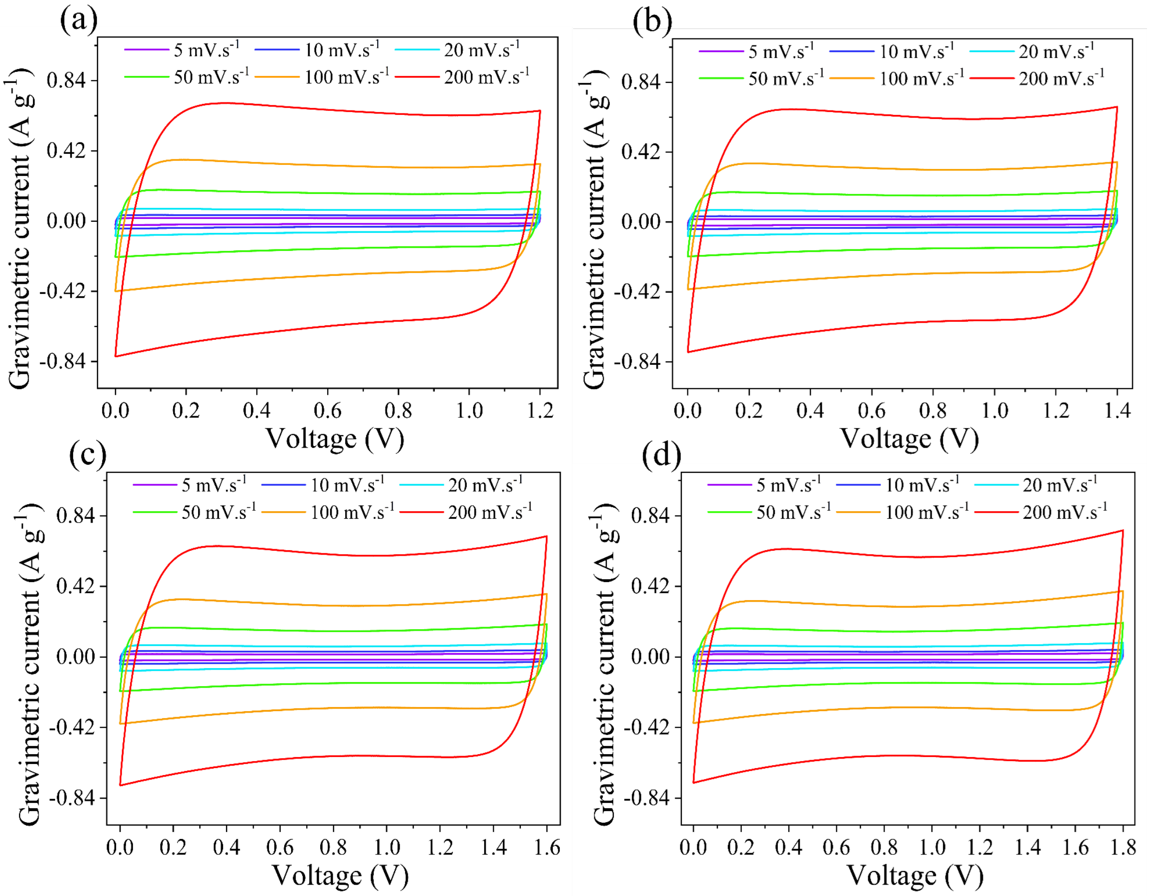

Figure 5.3 – Cyclic voltammetry measurements at different scan rates for the correct working voltage window and temperature condition. (a) at 25°C, (b) 10°C, (c) 0°C and (d) -10°C. Figure adapted from [93].

($n = 0.95$) obtained at 25°C and 1.2 V. For 10°C, an almost ideal phase angle of -87° ($n = 0.97$) was verified at 1.4 V (see Figure 5.4 (b)). It was verified for 0°C and 1.6 V a phase angle of -86° ($n = 0.95$) (see Figure 5.4 (c)). Furthermore, as shown in Figure 5.4 (d), at -10°C and 1.8 V, the phase angle is -87° ($n = 0.97$). Therefore, the EIS technique permitted the identification of small changes in the electrical double-layer capacitive behavior as a function of the temperature and voltage conditions.

Nevertheless, to confirm the best WVW, the SPSC technique was applied since the study in the time domain involving the analysis of current transients makes it possible to discriminate the capacitive and faradaic responses. For an ideal SC, the SPSC current response is given by

$$I_c = (\delta V / R_{esr}) * exp(-t / R_{esr}.C_{dl}), \tag{5.2}$$

where δV is the applied voltage step (pulse) and ($\delta V / R_{esr}$) is the initial current measured (I_0) at t → 0. For the most laboratory-made coin cell devices, which exhibit a short time constant ($\gamma = R_{esr}$*C$_{dl}$), the capacitive current must practically fade away, corresponding

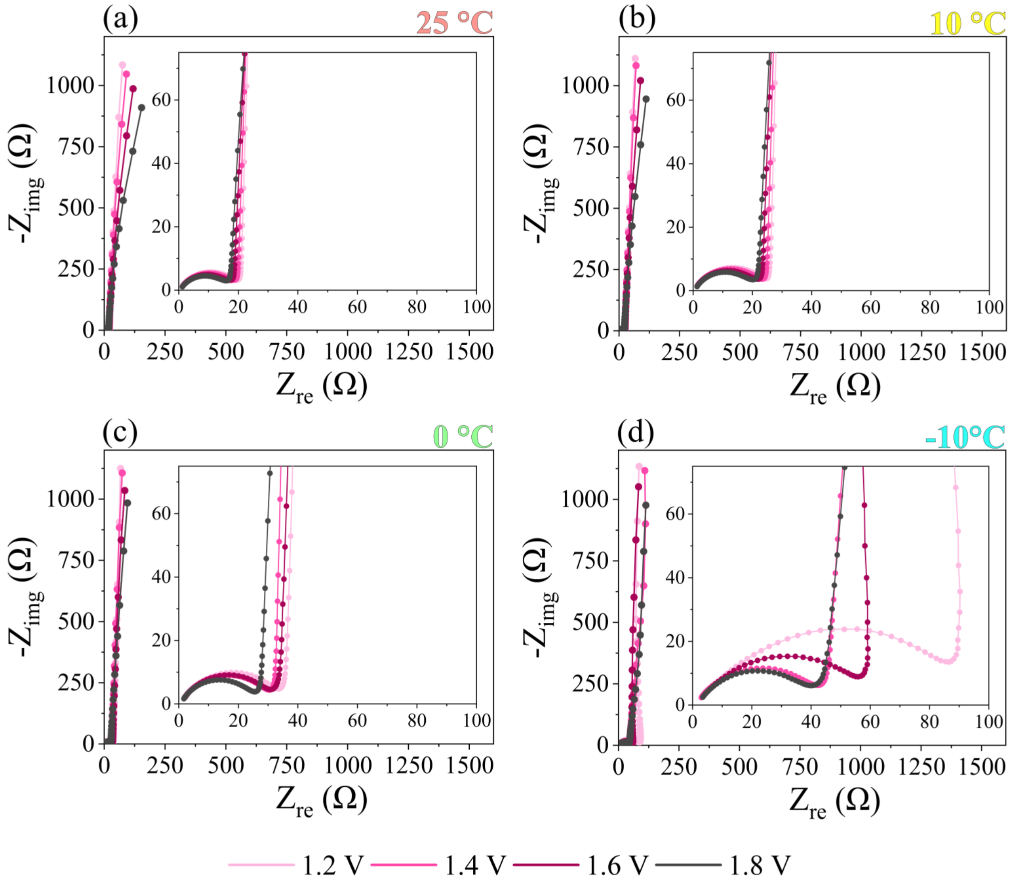

Figure 5.4 – Electrochemical impedance spectroscopy performance at several voltages (i.e., 1.2 V, 1.4 V, 1.6 V, and 1.8 V) and varied temperatures. Figure adapted from [93].

to a current reduction (e.g., I_c/I_0.100%) of ca. 98% after $\sim$ 1-20 s, depending on the electrode size and the active mass. Therefore, the verification of non-negligible stationary (residual) currents ($>$ 2%) in the SPSC experiments reveals the presence of an irreversible faradaic process (e.g., water-splitting), [1] since the latter does not depend on the elapsed time according to Butler-Volmer's model.

Figure 5.5 (a-d) shows the residual currents measured for the different experimental conditions up to 300 s. Generally, the use of low temperatures reduces the onset of the water-splitting reaction [142]. In all cases, current reductions higher than 99% were verified, i.e., maximum and minimum residual currents of 6.6 and 0.2 mA g^{-1} were verified for initial currents (I_0) of 3.1 and 1.3 A g^{-1}, respectively. Therefore, considering the SPSC experiments, one can discard the occurrence of water-splitting for practical purposes. It is worth mentioning that due to the high precision exhibited by the SPSC technique, the presence of minimal residual currents (e.g., $I_c/I_0 <$ 1%-2%) is commonly attributed to the presence of adventitious contaminations in the electrolyte solutions due to minute impurities present in the several chemicals used as-purchased, (i.e., without further purification) [22].

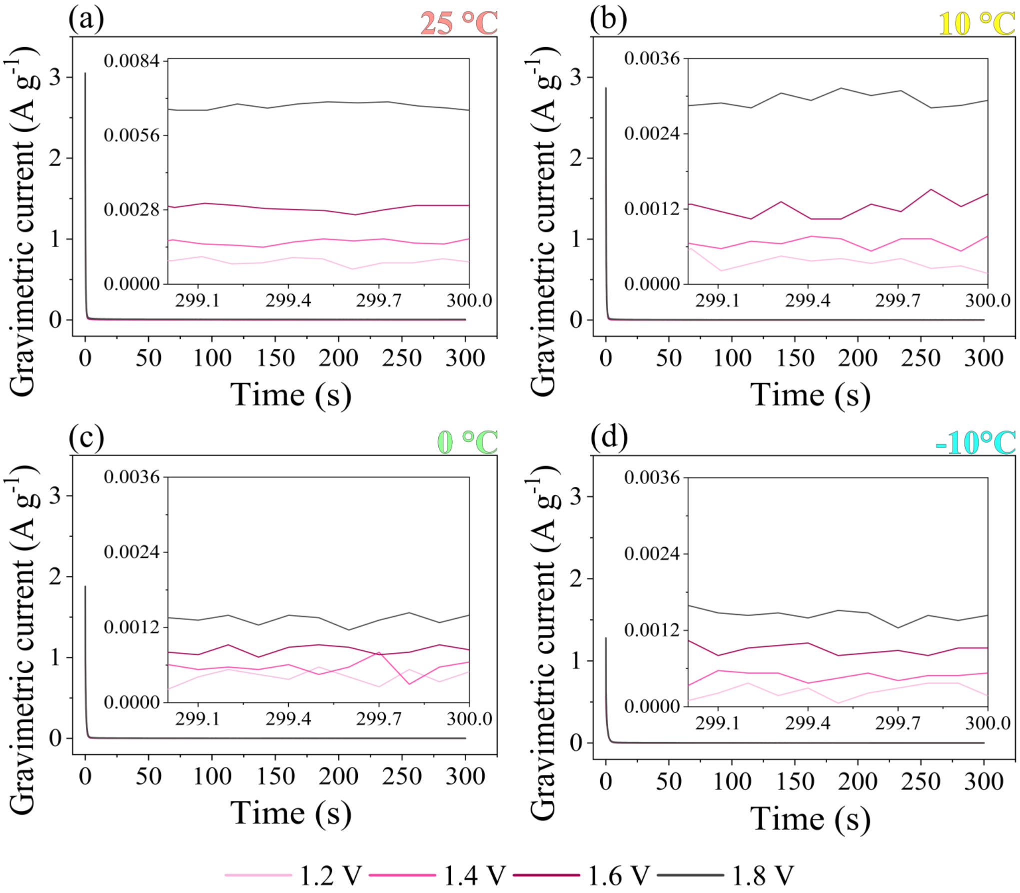

Figure 5.5 – Chronoamperometry performance at several voltages (i.e., 1.2 V, 1.4 V, 1.6 V, and 1.8 V) and varied temperatures. Figure adapted from [93].

The viscosity and conductivity of the electrolytes were measured as a function of the temperature to understand better the electrochemical behavior exhibited by the WISE-based SCs. Figure 5.6 shows the conductivity and viscosity of the WISE as a function of the temperature. As can be seen, the viscosity exhibited a pronounced linear decrease from -10°C to 0°C. On the contrary, for the temperature range of 0°C to 25°C, only a monotonically decrease was detected in the experiments. At the same time, the conductivity increased asymptotically for the entire temperature interval. However, the quantitative analysis of these findings is not straightforward.

Most studies involving the physicochemical properties of highly concentrated electrolytes (e.g., WISE) under non-equilibrium thermodynamic conditions incurred by the presence of a finite electric current flow, as is the case of the electrolyte conductivity, are empiric. From the theoretical viewpoint, even for diluted and moderate ionic solutions (e.g., $\sim$ 0.001-2.0 m) there are several difficulties due to the following phenomena: [179] (*i*) short- and long-range ion-ion interactions, (*ii*) electrophoretic phenomenon involving the 'dragging of the solvent species' in an electric field, (*iii*) 'relaxation effects' of the ionic cloud, and (*iv*) formation of ion pairs (e.g., the presence of dissolved, but undissociated ionic species).

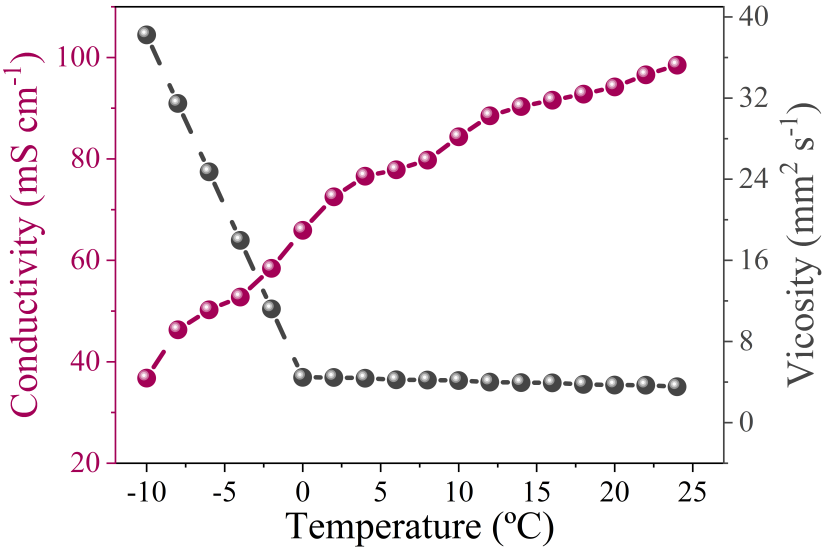

Figure 5.6 – Conductivity and viscosity of $NaClO_4$ *water-in-salt* aqueous electrolytes at different temperatures. Figure adapted from [93].

To quote, the electrolyte theories valid for equilibrium or non-equilibrium conditions, proposed by Debye-Hückel, Onsager, Fuoss, and Falkenhagen, are indeed 'limiting laws' valid only for diluted solutions (e.g., $\sim$ 0.001-0.1 m). It is worth mentioning that some modified versions of these electrolyte theories, such as the Bates-Guggenheim and Robinson-Stokes semi-empirical models, among others, have their applications extended to more concentrated solutions (e.g., $\sim$ 1 m) at the expense of using one or more empirical (adjustable) parameters. In this sense, the existing semi-empirical models are, in practice, sophisticated correlation functions. [180, 181] Even so, the maximum concentration values under investigation are far from that used in WISEs whose concentrations can reach up to ca. 10-20 m.

The semi-empirical model proposed by Wishaw-Stokes-Falkenhagen can be mentioned as a practical example of the complex scenario behind the study of electrolyte solutions. The latter relates the conductivity and viscosity at moderate concentrations (c $<$ 4 m) for asymmetric (1:1) electrolyte as follows: [179]

$$\frac{\Lambda\eta}{\eta^0} = \left(\Lambda^0 - \frac{B_2\sqrt{m}}{1+ka}\right)\left(1+\frac{\triangle X}{X}\right), \tag{5.3}$$

where Λ and η are the specific (molar) conductivity and viscosity of the solution at a given temperature, while Λ^0 and η^0 are the standard water conductivity and viscosity at the desired temperature, respectively. B_2 is the temperature-dependent electrophoretic coefficient, m is the molality, k is the Debye-Hückel reciprocal length, a is the mean ionic diameter (e.g., an adjustable parameter), and $1+\frac{\triangle X}{X}$ is the Falkenhagen's relaxation electric field factor accounting for the finite ion size. Please, for further details, see the Eq. (11.50) and the respective discussion in the seminal book by Robinson and Stokes [179].

It is worth mentioning that the experimental determination of the ‘relaxation electric field factor’ is not a facile task. The proper choice of an arbitrary/adjustable parameter is necessary to account for the effective ionic radii.

Therefore, the theoretical difficulties intrinsic to the study of concentrated solutions strongly preclude developing fundamental models for WISEs. In this sense, the use of computation methods (e.g., Monte-Carlo and Molecular Dynamics) based on different correlation functions is helpful for the study of different properties of the electrolyte solutions [180]. However, even these methods have shortcomings when some crucial aspects of the system cannot be disregarded or even simplified in the theoretical calculations to result in acceptable computation times.

Figure 5.7 shows the electrochemical findings obtained using different techniques for WISEs at different temperatures. The SCs were tested at a low gravimetric current for all temperatures, exhibiting the best triangular capacitive behavior at -10ºC. The relaxation time constant ($\tau_0 = 1/f_0$) was evaluated at -45° for the different temperatures using the impedance technique (see Figure 5.7 (c)). The τ_0 value is the smallest time required to promote charge and discharge in SCs with an efficiency higher than 50% [182]. As seen, the relaxation time increased more than 155% after the temperature decreased from 25°C to -10°C, (i.e., the charging and discharging processes at the lowest temperature demanded a three-fold relaxation time increase compared to ambient temperature). These findings are higher compared to those reported in the literature [43]. The high-frequency characteristics of SCs as a function of the temperature can be crucial for practical applications. As seen in Figure 5.7 (d), after 0.1 Hz, the influence of temperature becomes pronounced. The real component of the impedance is the main cause of the observed changes.

Figure 5.8 shows the electrochemical findings obtained from different techniques at diverse temperatures. The SCs were measured at the correct WVW of each temperature condition (e.g., 1.2, 1.4 V, 1.6 V, and 1.8 V for 25°C, 10°C, 0°C, and -10°C, respectively). As presented in Figure 5.8 (a), the specific capacitance decreased 17% as the temperature decreased (e.g., 17.4 F g^{-1} @ 25°C and 14.4 F g^{-1} @ -10°C). These findings can be understood considering that the ionic mobility is reduced at low temperatures while the electrolyte viscosity increases [147, 183]. At lower temperatures, the solute-solute interaction becomes more pronounced, and the ionic mobility in the Helmholtz plane is more restricted during the charge-discharge processes [146]. Also, the ionic desolvation at interfaces decreases with temperature decreasing, reducing the ionic drift, especially into the smaller micropores [51]. Hence, the electrical double layer (EDL) capacitance decreases, affecting specific energy (see the Ragone plot) [147].

Remembering that $E = C^*V^2/2$ gives the stored energy in SC, a capacitance decrease can be compensated when a substantial voltage increase is attained at low temperatures. Figure 5.8 (b) contrasts the specific energy and power in a Ragone plot at

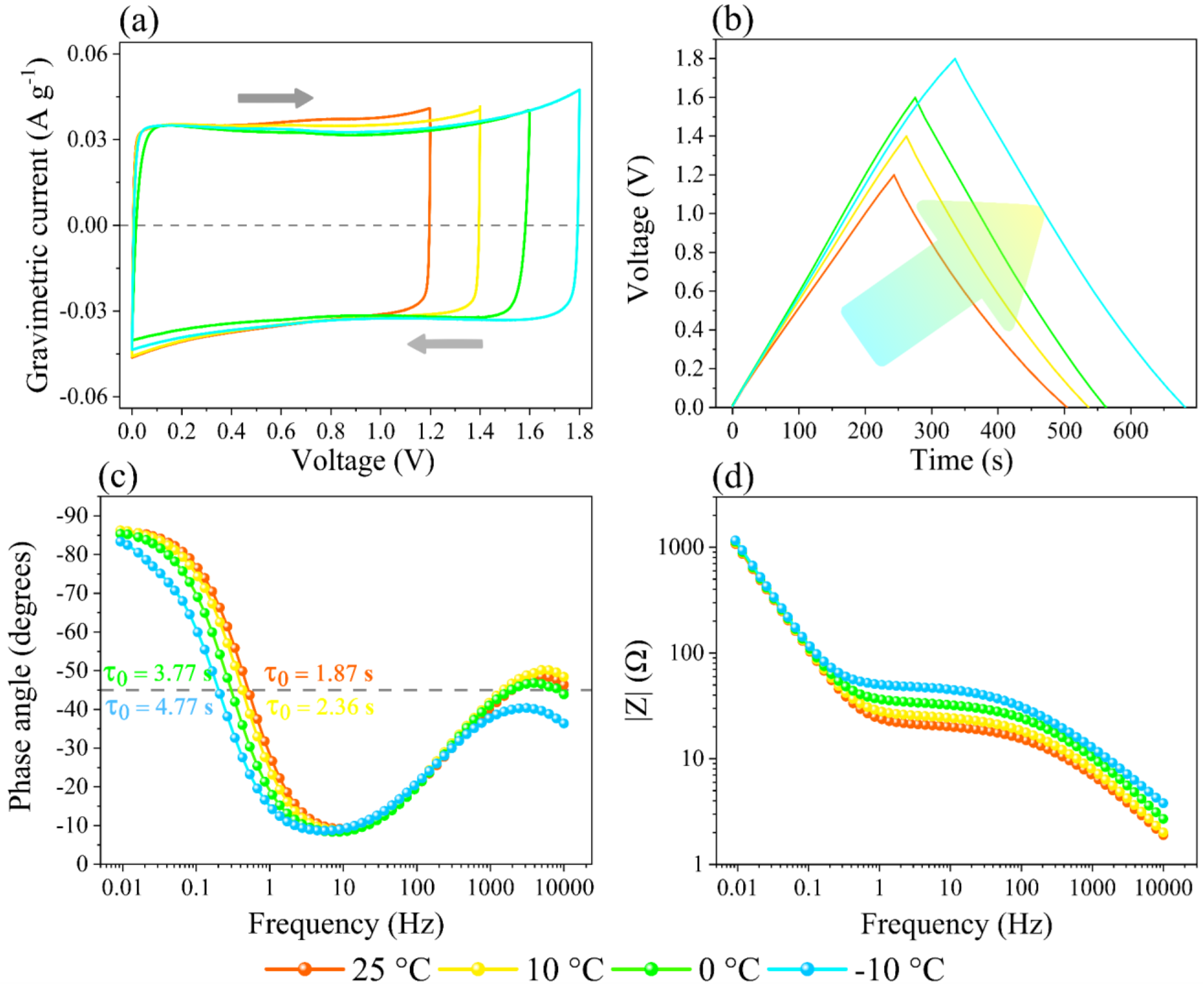

Figure 5.7 – Electrochemical performance of the supercapacitor at different temperatures. (a) Cyclic voltammetry curves at 10 mV s^{-1}. (b) Galvanostatic charge/discharge curves at 0.02 A g^{-1}. (c) Phase angle as a function of frequency. (d) Impedance as a function of frequency. Figure adapted from [93].

different temperatures [126]. As verified, maximum specific energies of 3.5 and 6.5 Wh kg^{-1} were verified at 25°C and -10°C, respectively. Therefore, the stored energy increased 86% for the maximum temperature reduction. On the contrary, after reducing the temperature from 25°C to -10°C, the specific power fell about 17%. This behavior can be understood considering the voltage increase is not entirely compensated by the equivalent series resistance increase entailed by the high viscosity attained at reduced temperatures (Please see Equation (4.3)).

Figure 5.8 (c) reveals the excellent capacitance retention values higher than 97% obtained for the different temperatures. In all cases, these findings indicate a high level of device stability, consistent with the absence of water-splitting in the different experimental conditions [184, 185]. Figure 5.8 (d) shows that temperature affects the specific capacitance concerning the gravimetric current for values higher than 5 A g^{-1}. These findings indicate that the ionic drift in the presence of an external (oscillating)

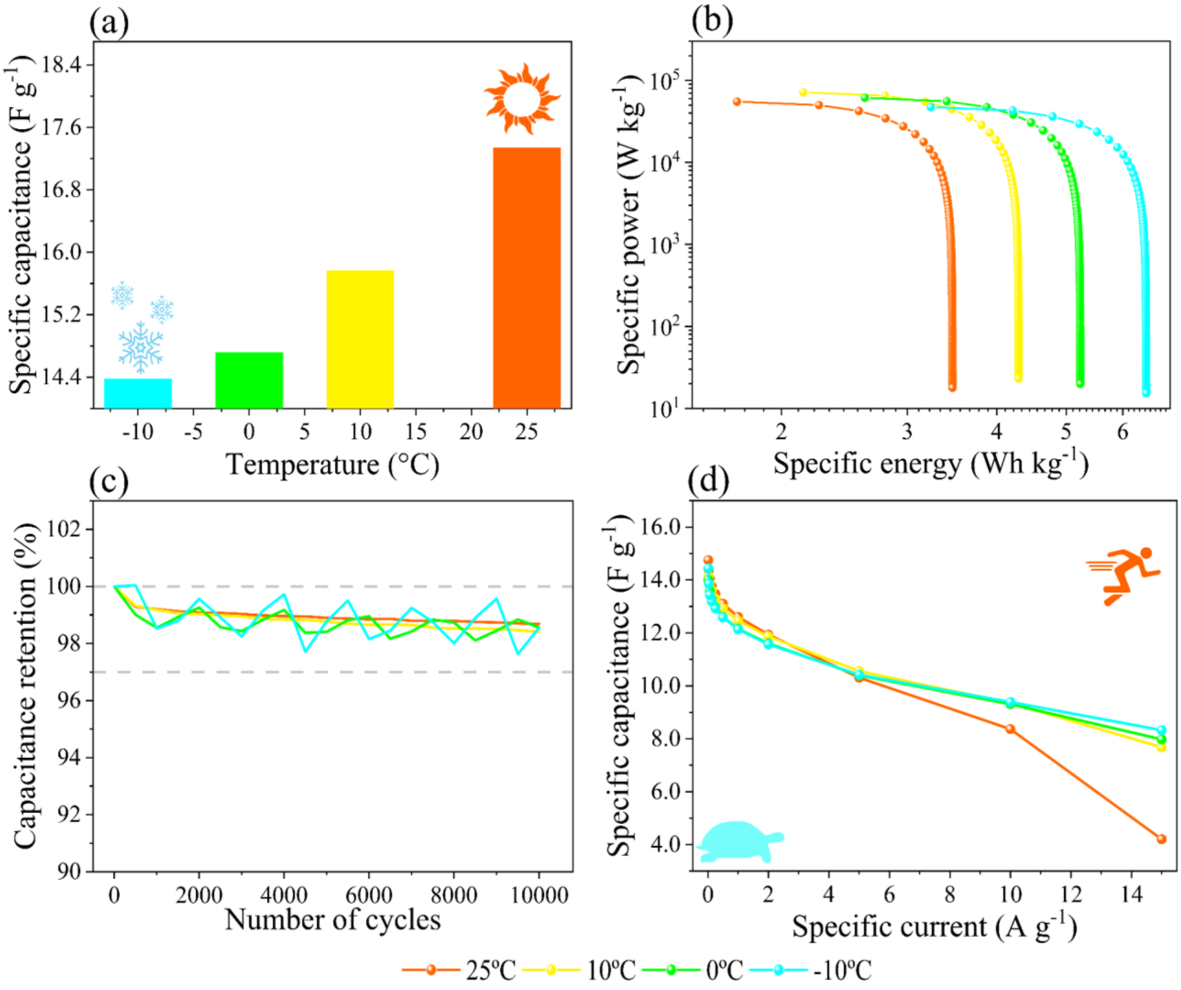

Figure 5.8 – Electrochemical performance of the supercapacitor at different temperatures. (a) Capacitance extracted from galvanostatic charge-discharge at 0.02 A g^{-1}. (b) Ragone plot in the function of temperature. (c) Capacitance retention to 10 thousand cycles of charge and discharge at 2 A g^{-1}. (d) Specific capacitance to different conditions of charge and discharge cycles. Figure adapted from [93].

electric field (charge migration) is mainly affected at higher specific currents, i.e., under conditions where a rapid motion of the positive and negative ionic species is necessary even in the presence of reduced mobility attained at higher viscosities.

The above considerations verify that low-temperature conditions used in WISE-based SC can benefit energy storage when the applied current does not exceed the threshold limit inherent to the particular electrochemical system.

5.3 Frequency Domain Analysis

Figure 5.9 contrasts the impedance data obtained from the complex-plane analysis using the Complex Nonlinear Squares (CNLS) fitting method. Simulations were accomplished using Conway-Tilak's circuit model (e.g., $R_{esr}*[C_{edl}/(R_l*C_{ads})]$) proposed for the study of the electrode/solution interface in the presence of a pseudocapacitance [174, 186–188]. Here, one has the following circuit parameters for the symmetric coin cell: (i) R_{esr} is the equivalent series resistance; (ii) C_{edl} is the electrical (electrostatic) double-layer capacitance; (iii) R_l is the leakage (or charge-transfer) resistance due to oxidation-reduction of oxygenated surface groups present on carbon materials; (iv) C_{ads} is the adsorption pseudocapacitance incurred by the solid-state faradaic (redox) processes.

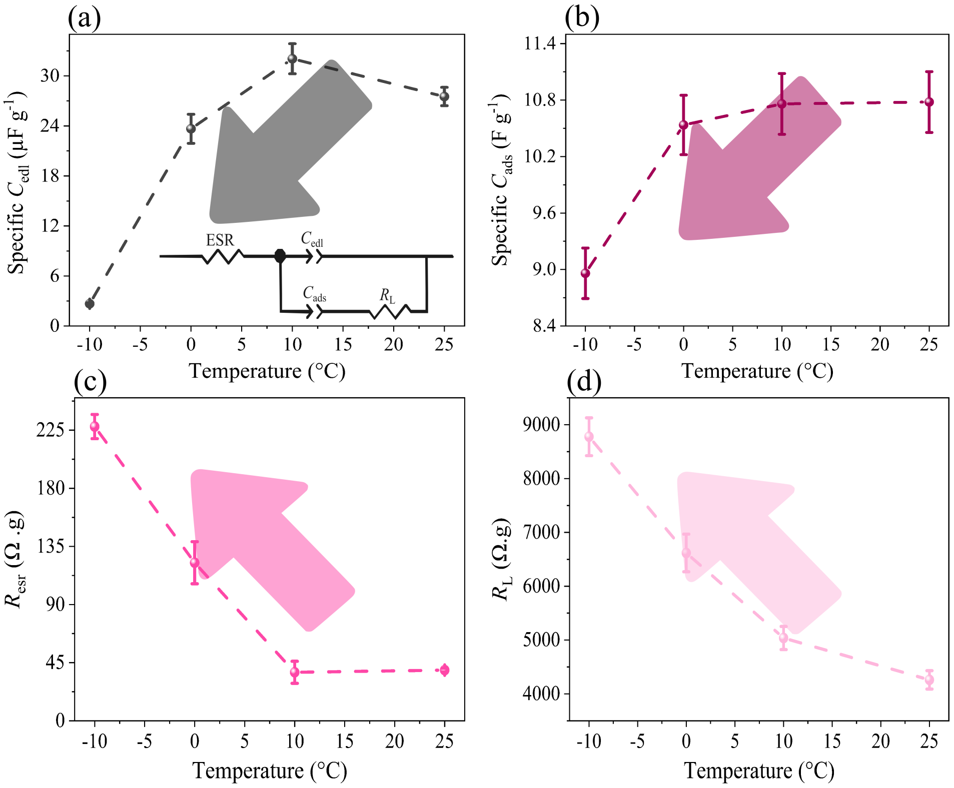

Figure 5.9 – Impedance data obtained from the complex-plane analysis. (a) Electrostatic capacitance (the inset shows the Tilak-Conway's circuit model used in the fitting/simulation procedure). (b) Adsorption pseudocapacitance during a solid-state faradaic reaction. (c) Equivalent series resistance. (d) Leakage or charge-transfer resistance for the faradaic reaction. Figure adapted from [93].

The capacitors (C_{edl} & C_{ads}) were replaced by constant phase elements (CPE, $Z_{cpe} = 1/Y_0(\mathrm{j}\omega)^{\mathrm{n}}$, where $\mathrm{n} \approx 1$) to consider the frequency dispersion phenomenon inherent to all solid electrodes. Afterward, the specific capacitance unities (F g^{-1}) were extracted from the fractal unities of the Y_0 coefficient using the Brug-Sluyters' formula.

Figure 5.9 (a-b) shows the adsorption pseudocapacitance and electrostatic capacitance as a function of the temperature. A similar trend for these parameters was observed with maximum values at 10°C. However, the magnitude verified for C_{ads} is much higher following the concept of pseudocapacitance. At the same time, the values obtained for C_{edl} are in the expected range for carbon-based coin cells. Generally, these data corroborate the previous GCD findings presented in 5.8 (a).

As already discussed in this work, the electrostatic capacitance (C_{edl}) is affected by the electrolyte viscosity that controls the ion migration at the interface. On the contrary, for the adsorption pseudocapacitance (C_{ads}), where the charged species are immobilized during the solid-state faradaic reaction, the observed behavior is due to the influence of temperature on the activation energy barrier for electron transfer. As a result, the surface coverage (Γoxi/red) by the reduced/oxidized oxygenated species is decreased at low temperatures, thus reducing the C_{ads} values (Please see Equation (5.1) and the discussion thereof).

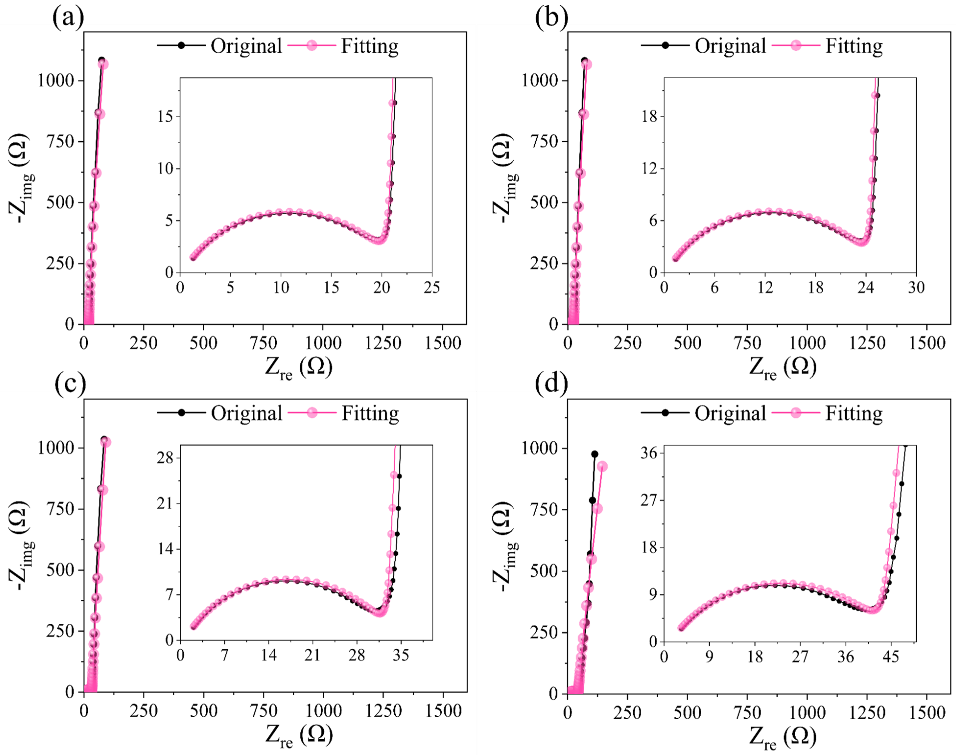

Figure 5.10 – Electrochemical impedance spectroscopy measures and their respective fitting representation. (a) at 25°C, (b) 10°C, (c) 0°C and (d) - 10°C. Figure adapted from [93].

As expected for ionic conductors, [144, 189–193] Figure 5.9 (c) exhibits a decrease of R_{esr} as a function of the temperature (see also Figure 5.10). Finally, Figure 5.9 (d) shows the leakage resistance as a function of the temperature. As seen, R_l values decreased almost exponentially on the temperature. Again, this behavior is due to the influence of temperature on the activation energy for electron transfer, i.e., according to Eyring's equation (Transition State Theory), the population of the redox species involved in a faradaic reaction exponentially increases as a function of the temperature [73, 194]. Thus, low surface coverages (Γoxi/red) referring to the activated-complex structure at reduced temperatures decrease the electron transfer rate at the electrode/electrolyte interface. A comparison between the EIS findings and the fitting quality at all temperatures can be found in Figure 5.10.

5.4 Raman Spectroscopy Analysis

To better understand the behavior of the ClO_4- anion structure and its vibrational modes at several temperatures, we investigated the modification of the Raman bands. Figure 5.11 (a) presents the Raman spectra obtained for a 17-m sodium perchlorate aqueous electrolyte at different temperatures. As seen, the bands slightly changed their position and the Full Width at Half Maximum (FWHM) according to the temperature. Figure 5.11 (b) shows the fitting obtained for the spectra at 25°C and the respective identified bands. The insert shows the data for the characteristic vibrational modes of perchlorate [194]. We fitted the curves to extract properly the FWHM and peak shifts, which are presented in Figure 5.12.

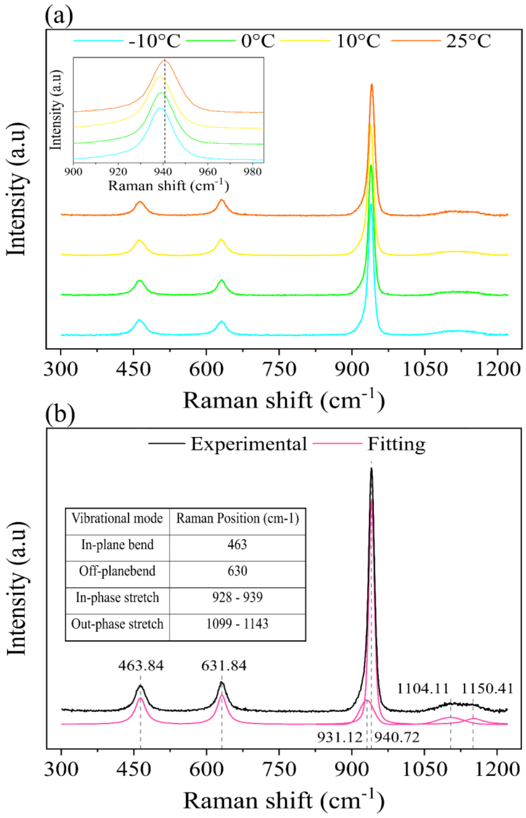

Vibrational mode	Raman Position (cm-1)
In-plane bend	463
Off-planebend	630
In-phase stretch	928 - 939
Out-phase stretch	1099 - 1143

Figure 5.11 – Raman spectra for multiwalled carbon nanotubes (Buckypaper electrodes). (a) Raman spectra at several temperatures. (b) Fitting of the Raman spectra obtained at 25°C. Bands and vibrational modes are highlighted. Figure adapted from [93].

Figure 5.12 (a-d) presents the prominent Raman bands at 939 cm^{-1} and 928 cm^{-1}. These two bands represent the same vibrational mode (fundamental and overtone) and correspond to the in-phase stretching [195]. Figure 5.12 (b and d) evidence that these two bands correspond to a blue shift of 2 cm^{-1} when the temperature falls from 25°C to -10°C, attributed to the water present in the solvation shell of the perchlorate aggregates. The perchlorate ions are closer together to the water molecules as the temperature drops. Figure 5.12 (a and c) highlights the FWHM reduction with the temperature drop. As seen, there is an increase in the organization/crystallinity of the dissolved perchlorate ions. The narrow the FWHM, the higher the material's crystallinity is [196]. In this case, as the temperature drops, Raman bands narrower, evidencing a higher degree of structural order and entropy reduction in the microsystem [197].

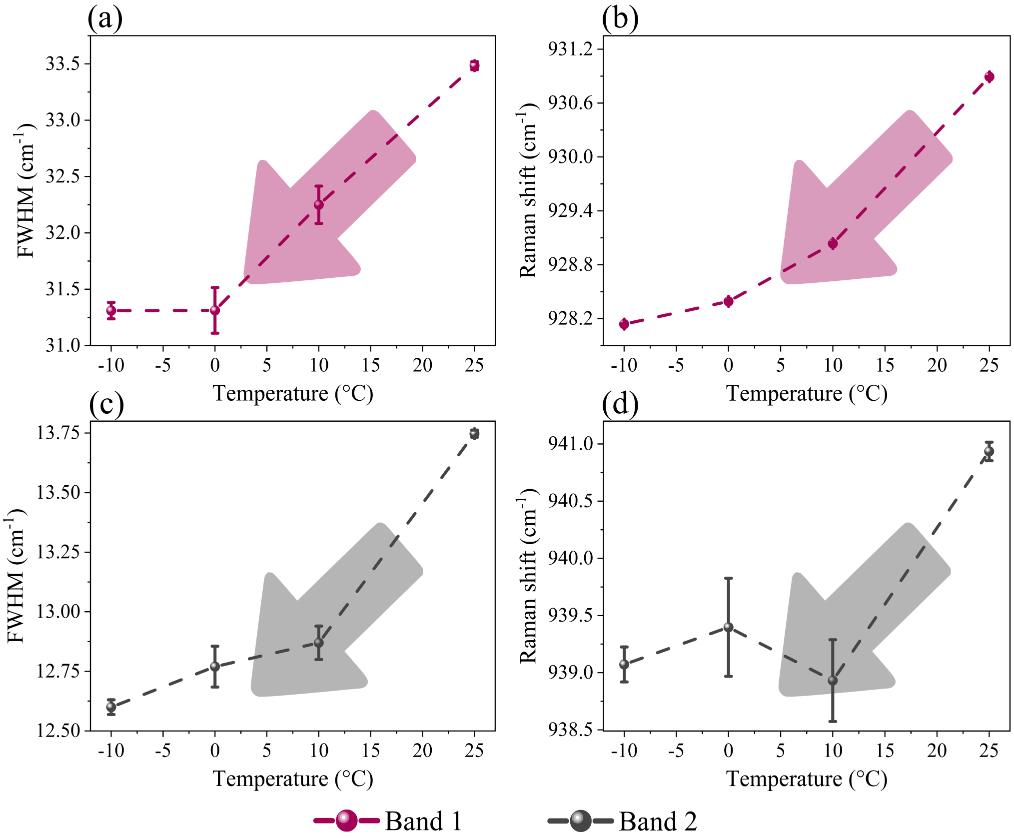

Figure 5.12 – Data extracted from the fitting of the Raman spectra at different temperatures, (a and b) Band 1 represents the band located at 939 cm^{-1} and (c and d) Band 2 located at 928 cm^{-1}. (a and c) The full width at half maximum represents the level of ClO_4- crystallinity. (b and d) The Raman shift of the ClO_4- stretching in-phase movement. Figure adapted from [93].

The in-phase stretching mode and FWHM behavior agree with the electrochemical results already discussed in this work. The lower the in-phase stretching, the narrow is the FWHM. Thus, a larger Gibbs' free energy is required at low temperatures to promote the water-splitting (oxygen evolution at the anode) for a given electric field, providing higher electrochemical stability to the electrolyte and larger WVW. As a result, the electrolyte system seems more compact and organized, i.e., the viscosity rises due to density increase and reduction in molecular vibration. Consequently, ionic mobility is reduced as the viscosity increases. For this reason, it is observed that the capacitance is reduced as the temperature decreases because the electrical double-layer formation is affected by low ionic accessibility into the MWCNT Buckypaper pores.

5.5 Concluding Remarks

This work reports on the electrochemical and Raman behavior of highly concentrated aqueous electrolytes, also known as water-in-salt electrolytes (WISE), using carbon-based buckypaper electrodes housed in symmetric coin cells as a function of the temperature. This work presents for the first time a comprehensive study of the electrochemical stability of electrolytes at reduced temperatures allowing the symmetric coin cells (supercapacitor prototype) to have a larger working voltage window in aqueous media (WVW). It was verified that WVW increases from 1.2 V at 25°C to 1.8 V at -10°C due to a less favorable water decomposition. A reduction in the specific capacitance from 17.4 F g^{-1} at 25°C to 14.4 F g^{-1} at -10°C was also verified. The temperature drop caused a decrease in ionic mobility and increased the electrolyte viscosity, affecting the charge transport in the compact region of the electrical double-layer. After all, the specific energy almost doubled due to its dependency on the voltage square, increasing from 3.5 W kg^{-1} at 25°C up to 6.5 W kg^{-1} at -10°C. These crucial findings highlight the importance of WISEs and low-temperature conditions during the charge-storage process in aqueous-based supercapacitors.

The current study also represents an excellent initial step towards a more flexible aqueous-based electrolyte system to be applied under cold weather conditions. Overall, the studied electrolyte system can permit users to achieve higher specific energy without increasing the occurrence of water-splitting, unwanted faradaic processes, and considerable capacitance losses as a function of the charge-discharge cycles. A great advantage in using the WISE-based systems at reduced temperatures is the possibility of working with non-flammable and environmentally friendly substances allied to an easy manufacturing process. Furthermore, by increasing the specific energy at low temperatures, deep seawater submarines and electric equipment in artic researcher centers, for example, could undergo a long-term operation under different energy and power demands.

6 Concluding Remarks and Future Works

Energy storage devices are fundamental to stimulating transportation electrification and mitigating global climate change. This crucial role increases interest in diverse applications, such as developing energy storage devices that operate at low temperatures and compressed conditions. Although SCs have shown compelling features that make their application a promise, due to the electrostatic nature of the energy storage process, the short distance separating the negative and positive electrodes, the absence of mass transport by diffusion, and compressibility of the electrode. That is different from batteries because they lose a significant part of the stored energy at low temperatures.

This study has focused on evaluating, describing, demonstrating, and discussing electrochemical measurements of symmetric SCs at low temperature and compression. This work presents for the first time a comprehensive study of the electrochemical stability of electrolytes at reduced temperatures and ion's adsorption/desorption in pore's electrodes at compression. It was verified that at low temperature, the WVW increases from 1.2 V at 25°C to 1.8 V at -10°C due to a less favorable water decomposition and the specific energy almost doubled due to its dependency on the voltage square, increasing from 3.5 W kg^{-1} at 25°C up to 6.5 W kg^{-1} at -10°C. In addition, the results showed the presence of a maximum energy storage point that is achieved when the electrode is compressed until the micropores match in dimensions with the electrolyte's hydrated ion size. Besides, the study shows that it is necessary to continuously compress the SC cell during the fabrication process using acceptable compression conditions to achieve high energy density and power density levels.

There are several practical applications of aqueous electrolytes SCs at low temperature and controlled compression, such as in the in-space avionic, astronomical observatories, high altitude aircraft, and the manufacturing industry. The results show that SCs in these areas could improve operating time and deliver the power of the electronic equipment due to low-temperature conditions and controlled compression. Besides Chapter 2 and 3, assessment of the procedures aims to contribute positively to the discussion of standardization and measurement reliability and provides practical, accessible and referred instructions for beginner-level users of such instrumentation.

Our results are encouraging and should be investigated further by combining compression and temperature in the same experimental setup to evaluate these two variables together. In addition, future studies should target and improve some crucial points to improve the results as:

- Set up an experiment that combines temperature change with SC cell compression;

- Increase the experiment's low-temperature range from -10°C to -40°C. To investigate whether it is possible to increase the WVW of the SC;
- Assess whether compression affects the identification of the SC WVW. For it has been seen that compression can affect the rate at which faradaic reactions occur;
- Set up the experiment with a three-electrode cell to investigate what happens during the absorption and desorption of ions at each electrode at compression and low-temperature conditions;
- Evaluate the effect of temperature for other aqueous electrolytes with a higher FPD than sodium perchlorate at 17m;
- To propose a mathematical model to relate the formation of the EDLC with the superionic effect for aqueous electrolyte SCs.

Bibliography

[1] A. Noori, M. F. El-Kady, M. S. Rahmanifar, R. B. Kaner, and M. F. Mousavi, "Towards establishing standard performance metrics for batteries, supercapacitors and beyond," 2019.

[2] M. M. Amaral, R. Venâncio, A. C. Peterlevitz, and H. Zanin, "Recent advances on quasi-solid-state electrolytes for supercapacitors," *Journal of Energy Chemistry*, vol. 67, pp. 697–717, 2022. [Online]. Available: https://www.sciencedirect.com/science/article/pii/S2095495621006148

[3] C. G. Real, R. Vicentini, W. G. Nunes, A. M. Pascon, F. A. Campos, L. M. Da Silva, R. G. Freitas, and H. Zanin, "Analyses of dispersive effects and the distributed capacitance in the time and frequency domains of activated carbon nanofiber electrodes as symmetric supercapacitors," *Electrochimica Acta*, vol. 402, p. 139299, 2022. [Online]. Available: https://www.sciencedirect.com/science/article/pii/S0013468621015899

[4] D. A. D. Silva, M. J. P. C., A. Messias, E. E. Fileti, A. Pascon, D. V. Franco, L. M. D. Silva, and H. G. Zanin, "Effect of conductivity, viscosity, and density of water-in-salt electrolytes on the electrochemical behavior of supercapacitors: molecular dynamics simulations and in situ characterization studies," *Materials Advances*, vol. 3, pp. 611–623, 1 2022. [Online]. Available: https://pubs.rsc.org/en/content/articlehtml/2022/ma/d1ma00890khttps://pubs.rsc.org/en/content/articlelanding/2022/ma/d1ma00890k

[5] A. J. P. Neto, D. A. D. Silva, V. A. Gonçalves, H. Zanin, R. G. Freitas, and E. E. Fileti, "An evaluation of the capacitive behavior of supercapacitors as a function of the radius of cations using simulations with a constant potential method," *Physical Chemistry Chemical Physics*, vol. 24, pp. 3280–3288, 2 2022. [Online]. Available: https://pubs.rsc.org/en/content/articlehtml/2022/cp/d1cp04350ahttps://pubs.rsc.org/en/content/articlelanding/2022/cp/d1cp04350a

[6] R. Vicentini, R. Venâncio, W. Nunes, L. M. D. Silva, and H. Zanin, "New insights on the sodium water-in-salt electrolyte and carbon electrode interface from electrochemistry and operando raman studies," *ACS Applied Materials and Interfaces*, vol. 13, pp. 61 139–61 153, 12 2021. [Online]. Available: https://pubs.acs.org/doi/abs/10.1021/acsami.1c18777

[7] R. Vicentini, R. Beraldo, J. P. Aguiar, F. E. Oliveira, F. C. Rufino, D. R. G. Larrude, L. M. D. Silva, and H. Zanin, "Niobium pentoxide nanoparticles decorated graphene

as electrode material in aqueous-based supercapacitors: Accurate determination of the working voltage window and the analysis of the distributed capacitance in the time domain," *Journal of Energy Storage*, vol. 44, p. 103371, 12 2021.

[8] M. Alexandreli, C. B. Brocchi, D. M. Soares, W. G. Nunes, B. G. Freitas, F. E. de Oliveira, L. E. C. A. Schiavo, A. C. Peterlevitz, L. M. da Silva, and H. Zanin, "Pseudocapacitive behaviour of iron oxides supported on carbon nanofibers as a composite electrode material for aqueous-based supercapacitors," *Journal of Energy Storage*, vol. 42, p. 103052, 10 2021.

[9] R. Vicentini, L. M. D. Silva, D. V. Franco, W. G. Nunes, J. Fiates, G. Doubek, L. F. Franco, R. G. Freitas, C. Fantini, and H. Zanin, "Raman probing carbon and aqueous electrolytes interfaces and molecular dynamics simulations towards understanding electrochemical properties under polarization conditions in supercapacitors," *Journal of Energy Chemistry*, vol. 60, pp. 279–292, 9 2021.

[10] D. M. Soares, Z. Ren, S. B. Mujib, S. Mukherjee, C. G. M. Real, M. Anstine, H. Zanin, and G. Singh, "Additive manufacturing of electrochemical energy storage systems electrodes," *Advanced Energy and Sustainability Research*, vol. 2, p. 2000111, 5 2021. [Online]. Available: https://onlinelibrary.wiley.com/doi/full/10.1002/aesr.202000111https://onlinelibrary.wiley.com/doi/abs/10.1002/aesr.202000111https://onlinelibrary.wiley.com/doi/10.1002/aesr.202000111

[11] D. A. D. Silva, A. J. P. Neto, A. M. Pascon, E. E. Fileti, L. R. Fonseca, and H. G. Zanin, "Combined density functional theory and molecular dynamics simulations to investigate the effects of quantum and double-layer capacitances in functionalized graphene as the electrode material of aqueous-based supercapacitors," *Journal of Physical Chemistry C*, vol. 125, pp. 5518–5524, 3 2021. [Online]. Available: https://pubs.acs.org/doi/abs/10.1021/acs.jpcc.0c11602

[12] B. M. Pires, W. G. Nunes, B. G. Freitas, F. E. R. Oliveira, V. Katic, C. B. Rodella, L. M. D. Silva, and H. Zanin, "Characterization of porous cobalt hexacyanoferrate and activated carbon electrodes under dynamic polarization conditions in a sodium-ion pseudocapacitor," *Journal of Energy Chemistry*, vol. 54, pp. 53–62, 3 2021.

[13] W. G. Nunes, A. N. Miranda, B. Freitas, R. Vicentini, A. C. Oliveira, G. Doubek, R. G. Freitas, L. M. D. Silva, and H. Zanin, "Charge-storage mechanism of highly defective nio nanostructures on carbon nanofibers in electrochemical supercapacitors," *Nanoscale*, vol. 13, pp. 9590–9605, 6 2021. [Online]. Available: https://pubs.rsc.org/en/content/articlehtml/2021/nr/d1nr00065ahttps://pubs.rsc.org/en/content/articlelanding/2021/nr/d1nr00065a

[14] R. Vicentini, W. G. Nunes, L. H. da Costa, L. M. D. Silva, B. Freitas, A. M. Pascon, O. Vilas-Boas, and H. Zanin, "Multi-walled carbon nanotubes and activated carbon composite material as electrodes for electrochemical capacitors," *Journal of Energy Storage*, vol. 33, p. 100738, 1 2021.

[15] W. G. Nunes, R. Vicentini, B. G. Freitas, F. E. Oliveira, A. M. Marque, R. M. Filho, G. Doubek, L. M. D. Silva, and H. Zanin, "Pseudo-capacitive behavior of multi-walled carbon nanotubes decorated with nickel and manganese (hydr)oxides nanoparticles," *Journal of Energy Storage*, vol. 31, p. 101583, 10 2020.

[16] W. G. Nunes, B. M. Pires, F. E. D. Oliveira, A. M. de Marque, L. F. Cremasco, R. Vicentini, G. Doubek, L. M. D. Silva, and H. Zanin, "Study of the aging process of nanostructured porous carbon-based electrodes in electrochemical capacitors filled with aqueous or organic electrolytes," *Journal of Energy Storage*, vol. 28, p. 101249, 4 2020.

[17] D. A. D. Silva, A. J. P. Neto, A. M. Pascon, E. E. Fileti, L. R. Fonseca, and H. G. Zanin, "Exploring doped or vacancy-modified graphene-based electrodes for applications in asymmetric supercapacitors," *Physical Chemistry Chemical Physics*, vol. 22, pp. 3906–3913, 2 2020. [Online]. Available: https://pubs.rsc.org/en/content/articlehtml/2020/cp/c9cp06495hhttps://pubs.rsc.org/en/content/articlelanding/2020/cp/c9cp06495h

[18] R. Vicentini, L. M. D. Silva, E. P. Cecilio, T. A. Alves, W. G. Nunes, and H. Zanin, "How to measure and calculate equivalent series resistance of electric double-layer capacitors," *Molecules 2019, Vol. 24, Page 1452*, vol. 24, p. 1452, 4 2019. [Online]. Available: https://www.mdpi.com/1420-3049/24/8/1452/htmhttps://www.mdpi.com/1420-3049/24/8/1452

[19] J. J. Teles, E. R. Faria, J. H. Santos, L. G. D. Sousa, D. V. Franco, W. G. Nunes, H. Zanin, and L. M. D. Silva, "Supercapacitive properties, anomalous diffusion, and porous behavior of nanostructured mixed metal oxides containing sn, ru, and ir," *Electrochimica Acta*, vol. 295, pp. 302–315, 2 2019.

[20] R. Vicentini, W. G. Nunes, L. H. Costa, L. M. D. Silva, A. Pascon, P. Jackson, G. Doubek, and H. Zanin, "Highly stable nickel-aluminum alloy current collectors and highly defective multi-walled carbon nanotubes active material for neutral aqueous-based electrochemical capacitors," *Journal of Energy Storage*, vol. 23, pp. 116–127, 6 2019.

[21] W. G. Nunes, L. M. D. Silva, R. Vicentini, B. G. Freitas, L. H. Costa, A. M. Pascon, and H. Zanin, "Nickel oxide nanoparticles supported onto oriented multi-walled

carbon nanotube as electrodes for electrochemical capacitors," *Electrochimica Acta*, vol. 298, pp. 468–483, 3 2019.

[22] R. Vicentini, D. M. Soares, W. Nunes, B. Freitas, L. Costa, L. M. D. Silva, and H. Zanin, "Core-niobium pentoxide carbon-shell nanoparticles decorating multiwalled carbon nanotubes as electrode for electrochemical capacitors," *Journal of Power Sources*, vol. 434, p. 226737, 9 2019.

[23] R. Vicentini, W. Nunes, B. G. Freitas, L. M. D. Silva, D. M. Soares, R. Cesar, C. B. Rodella, and H. Zanin, "Niobium pentoxide nanoparticles @ multi-walled carbon nanotubes and activated carbon composite material as electrodes for electrochemical capacitors," *Energy Storage Materials*, vol. 22, pp. 311–322, 11 2019.

[24] D. M. Soares, R. Vicentini, A. C. Peterlevitz, C. B. Rodella, L. M. da Silva, and H. Zanin, "Tungsten oxide and carbide composite synthesized by hot filament chemical deposition as electrodes in aqueous-based electrochemical capacitors," *Journal of Energy Storage*, vol. 26, p. 100905, 12 2019.

[25] W. G. Nunes, R. Vicentini, L. M. D. Silva, L. H. Costa, T. Tadeu, and H. Zanin, "Surface and electrochemical properties of radially oriented multiwalled carbon nanotubes grown on stainless steel mesh," *Journal of The Electrochemical Society*, vol. 165, pp. A3684–A3696, 12 2018. [Online]. Available: https://iopscience.iop.org/article/10.1149/2.022816jeshttps://iopscience.iop.org/article/10.1149/2.022816jes/meta

[26] R. Vicentini, L. H. Costa, W. Nunes, O. V. Boas, D. M. Soares, T. A. Alves, C. Real, C. Bueno, A. C. Peterlevitz, and H. Zanin, "Direct growth of mesoporous carbon on aluminum foil for supercapacitors devices," *Journal of Materials Science: Materials in Electronics*, vol. 29, pp. 10 573–10 582, 6 2018. [Online]. Available: https://link.springer.com/article/10.1007/s10854-018-9121-1

[27] C. G. M. Real, R. Vicentini, W. G. Nunes, O. V. Boas, L. H. Costa, D. M. Soares, and H. Zanin, "Electric double layer capacitors prepared with polyvinyl alcohol and multi-walled carbon nanotubes," *SAE Technical Papers*, 9 2018. [Online]. Available: https://www.sae.org/publications/technical-papers/content/2018-36-0313/

[28] C. G. M. Real, R. Vicentini, W. G. Nunes, O. V. Boas, T. A. Alves, D. M. Soares, and H. Zanin, "Polyacrylonitrile and activated carbon composite for electric double layer capacitors," *SAE Technical Papers*, 9 2018. [Online]. Available: https://www.sae.org/publications/technical-papers/content/2018-36-0310/

[29] R. Vicentini, W. G. Nunes, L. H. Costa, A. Pascon, L. M. D. Silva, M. Baldan, and H. Zanin, "Environmentally friendly functionalization of porous carbon electrodes for

aqueous-based electrochemical capacitors," *IEEE Transactions on Nanotechnology*, vol. 18, pp. 73–82, 2019.

[30] C. Antônio Rufino Júnior, E. R. Sanseverino, P. Gallo, D. Koch, H.-G. Schweiger, and H. Zanin, "Blockchain review for battery supply chain monitoring and battery trading," *Renewable and Sustainable Energy Reviews*, vol. 157, p. 112078, 2022. [Online]. Available: https://www.sciencedirect.com/science/article/pii/S1364032122000089

[31] V. S. Carvalho, A. N. Miranda, W. G. Nunes, L. H. Costa, A. M. Pascon, C. B. Rodella, H. Zanin, and G. Doubek, "Radially ordered carbon nanotubes performance for li-o2 batteries: Pre-treatment influence on capacity and discharge products," *Catalysis Today*, vol. 348, pp. 299–306, 5 2020.

[32] L. M. Da Silva, R. Cesar, C. M. Moreira, J. H. Santos, L. G. De Souza, B. M. Pires, R. Vicentini, W. Nunes, and H. Zanin, "Reviewing the fundamentals of supercapacitors and the difficulties involving the analysis of the electrochemical findings obtained for porous electrode materials," 2020.

[33] M. M. Amaral, M. J. Pinzón C., A. C. Peterlevitz, C. A. Rufino, L. M. Da Silva, and H. Zanin, "Robust, freestanding, and bendable multi-walled carbon nanotube buckypapers as electrode materials for quasi solid-state potassium-ion supercapacitors," *Diamond and Related Materials*, 2021.

[34] J. S. Lawrence, M. C. Ashley, S. Hengst, D. M. Luong-Van, J. W. Storey, H. Yang, X. Zhou, and Z. Zhu, "The PLATO dome a site-testing observatory: Power generation and control systems," *Review of Scientific Instruments*, 2009.

[35] F. Béguin and E. Frackowiak, *Supercapacitors: Materials, Systems, and Applications*. Wiley, 2013.

[36] C. Zhong, Y. Deng, W. Hu, J. Qiao, L. Zhang, and J. Zhang, "A review of electrolyte materials and compositions for electrochemical supercapacitors," 2015.

[37] Y. Rangom, X. Tang, and L. F. Nazar, "Carbon Nanotube-Based Supercapacitors with Excellent ac Line Filtering and Rate Capability via Improved Interfacial Impedance," *ACS Nano*, 2015.

[38] A. Muzaffar, M. B. Ahamed, K. Deshmukh, and J. Thirumalai, "A review on recent advances in hybrid supercapacitors: Design, fabrication and applications," 2019.

[39] T. Mesbahi, P. Bartholomeus, N. Rizoug, R. Sadoun, F. Khenfri, and P. L. Moigne, "Advanced Model of Hybrid Energy Storage System Integrating Lithium-Ion Battery and Supercapacitor for Electric Vehicle Applications," *IEEE Transactions on Industrial Electronics*, 2021.

[40] Q. Zhang, L. Wang, G. Li, and Y. Liu, “A real-time energy management control strategy for battery and supercapacitor hybrid energy storage systems of pure electric vehicles,” *Journal of Energy Storage*, 2020.

[41] C. M. Enang and B. K. Johnson, “Bidirectional dc-dc converter control in battery-supercapacitor hybrid energy storage system,” in *2020 IEEE Power and Energy Society Innovative Smart Grid Technologies Conference, ISGT 2020*, 2020.

[42] W. Sun, Y. Zhang, and F. Yang, “A High-Performance Symmetric Supercapacitor from Porous Activated Carbon under Compression,” *Energy Technology*, 2021.

[43] Y. Sun, Y. Wang, L. Liu, B. Liu, Q. Zhang, D. Wu, H. Zhang, and X. Yan, “Towards the understanding of acetonitrile suppressing salt precipitation mechanism in a water-in-salt electrolyte for low-temperature supercapacitors,” *Journal of Materials Chemistry A*, 2020.

[44] X. Li, J. Rong, and B. Wei, “Electrochemical behavior of single-walled carbon nanotube supercapacitors under compressive stress,” *ACS Nano*, 2010.

[45] K. B. Li, D. W. Shi, Z. Y. Cai, G. L. Zhang, Q. A. Huang, D. Liu, and C. P. Yang, “Studies on the equivalent serial resistance of carbon supercapacitor,” *Electrochimica Acta*, 2015.

[46] C. Masarapu, L. P. Wang, X. Li, and B. Wei, “Tailoring electrode/electrolyte interfacial properties in flexible supercapacitors by applying pressure,” *Advanced Energy Materials*, 2012.

[47] H. Wang, X. Liu, B. Zhang, J. Yang, Z. Zhang, R. Yue, and Z. Wang, “Highly compressible supercapacitor based on carbon nanotubes-reinforced sponge electrode,” *Journal of Alloys and Compounds*, 2019.

[48] L. Sheng, J. Chang, L. Jiang, Z. Jiang, Z. Liu, T. Wei, and Z. Fan, “Multilayer-Folded Graphene Ribbon Film with Ultrahigh Areal Capacitance and High Rate Performance for Compressible Supercapacitors,” *Advanced Functional Materials*, 2018.

[49] G. Ah-Lung, B. Flamme, F. Ghamouss, M. Maréchal, and J. Jacquemin, “Guidelines for designing highly concentrated electrolytes for low temperature applications,” *Chemical Communications*, 2020.

[50] X. Wang, H. Huang, F. Zhou, P. Das, P. Wen, S. Zheng, P. Lu, Y. Yu, and Z. S. Wu, “High-voltage aqueous planar symmetric sodium ion micro-batteries with superior performance at low-temperature of - 40ºc,” *Nano Energy*, 2021.

[51] S. W. Xu, M. C. Zhang, G. Q. Zhang, J. H. Liu, X. Z. Liu, X. Zhang, D. D. Zhao, C. L. Xu, and Y. Q. Zhao, “Temperature-dependent performance of carbon-based supercapacitors with water-in-salt electrolyte,” *Journal of Power Sources*, 2019.

[52] Q. Dou, S. Lei, D. W. Wang, Q. Zhang, D. Xiao, H. Guo, A. Wang, H. Yang, Y. Li, S. Shi, and X. Yan, “Safe and high-rate supercapacitors based on an "acetonitrile/water in salt" hybrid electrolyte,” *Energy and Environmental Science*, 2018.

[53] X. Lu, R. J. Jiménez-Riobóo, D. Leech, M. C. Gutiérrez, M. L. Ferrer, and F. Del Monte, “Aqueous-Eutectic-in-Salt Electrolytes for High-Energy-Density Supercapacitors with an Operational Temperature Window of 100 °c, from-35 to +65 °c,” *ACS Applied Materials and Interfaces*, 2020.

[54] A. González, E. Goikolea, J. A. Barrena, and R. Mysyk, “Review on supercapacitors: Technologies and materials,” 2016.

[55] Poonam, K. Sharma, A. Arora, and S. K. Tripathi, “Review of supercapacitors: Materials and devices,” 2019.

[56] H. Shao, Y. C. Wu, Z. Lin, P. L. Taberna, and P. Simon, “Nanoporous carbon for electrochemical capacitive energy storage,” 2020.

[57] L. G. d. R. Guedes and J. P. A. Dos Santos, “Clustered Social Representation of Active Methodologies in Engineering Courses a case study at Goiás State, Brazil,” *International Journal on Alive Engineering Education*, 2019.

[58] J. Biggs and C. Tang, *Teaching for quality learning at university: What the Student Does.* McGraw-Hill Education, 2013.

[59] J. Biggs, “Enhancing teaching through constructive alignment,” *Higher Education*, 1996.

[60] A. W. Astin, “Student involvement: A developmental theory for higher education,” in *College Student Development and Academic Life: Psychological, Intellectual, Social and Moral Issues*, 2014.

[61] L. Hunt and D. Chalmers, *University teaching in focus: A learning-centred approach.* Routledge, 2021.

[62] F. Castilho, *O Conceito de Universidade no Projeto da UNICAMP*, 1st ed. Editora UNICAMP, 2008.

[63] T. S. Mathis, N. Kurra, X. Wang, D. Pinto, P. Simon, and Y. Gogotsi, “Energy Storage Data Reporting in Perspective—Guidelines for Interpreting the Performance of Electrochemical Energy Storage Systems,” 2019.

[64] P. Simon and Y. Gogotsi, “Materials for electrochemical capacitors,” 2008.

[65] J. R. Miller and P. Simon, “Materials science: Electrochemical capacitors for energy management,” 2008.

[66] P. Simon, Y. Gogotsi, and B. Dunn, “Where do batteries end and supercapacitors begin?” 2014.

[67] D. Pech, M. Brunet, H. Durou, P. Huang, V. Mochalin, Y. Gogotsi, P. L. Taberna, and P. Simon, “Ultrahigh-power micrometre-sized supercapacitors based on onion-like carbon,” *Nature Nanotechnology*, 2010.

[68] M. Salanne, B. Rotenberg, K. Naoi, K. Kaneko, P. L. Taberna, C. P. Grey, B. Dunn, and P. Simon, “Efficient storage mechanisms for building better supercapacitors,” 2016.

[69] Y. Gogotsi and P. Simon, “True performance metrics in electrochemical energy storage,” 2011.

[70] V. Augustyn, J. Come, M. A. Lowe, J. W. Kim, P. L. Taberna, S. H. Tolbert, H. D. Abruña, P. Simon, and B. Dunn, “High-rate electrochemical energy storage through Li + intercalation pseudocapacitance,” *Nature Materials*, 2013.

[71] M. Naguib, J. Halim, J. Lu, K. M. Cook, L. Hultman, Y. Gogotsi, and M. W. Barsoum, “New two-dimensional niobium and vanadium carbides as promising materials for li-ion batteries,” *Journal of the American Chemical Society*, 2013.

[72] M. Alhabeb, K. Maleski, B. Anasori, P. Lelyukh, L. Clark, S. Sin, and Y. Gogotsi, “Guidelines for Synthesis and Processing of Two-Dimensional Titanium Carbide (Ti3C2Tx MXene),” *Chemistry of Materials*, 2017.

[73] M. E. Orazem and B. Tribollet, *Electrochemical Impedance Spectroscopy.* John Wiley & Sons, Inc, 2008.

[74] Z. Yang, J. Tian, Z. Yin, C. Cui, W. Qian, and F. Wei, “Carbon nanotube- and graphene-based nanomaterials and applications in high-voltage supercapacitor: A review,” 2019.

[75] G. Wang, L. Zhang, and J. Zhang, “A review of electrode materials for electrochemical supercapacitors,” *Chemical Society Reviews*, 2012.

[76] X. Bu, L. Su, Q. Dou, S. Lei, and X. Yan, “A low-cost “water-in-salt” electrolyte for a 2.3 V high-rate carbon-based supercapacitor,” *Journal of Materials Chemistry A*, 2019.

[77] W. G. Nunes, B. G. Freitas, R. M. Beraldo, R. M. Filho, L. M. Da Silva, and H. Zanin, "A rational experimental approach to identify correctly the working voltage window of aqueous-based supercapacitors," *Scientific Reports*, 2020.

[78] F. Qu, D. Jiang, Z. Liu, A. Zhang, Y. Zheng, Q. Jia, C. Li, and J. Liu, "Hierarchical polypyrrole/graphene/melamine composite foam for highly compressible all-solid-state supercapacitors," *Electrochimica Acta*, 2020.

[79] G. Gourdin, T. Jiang, P. Smith, and D. Qu, "The effects of cell assembly compression on the performance of carbon electrochemical double-layer capacitor electrodes," *Journal of Power Sources*, 2012.

[80] M. D. Stoller, S. A. Stoller, N. Quarles, J. W. Suk, S. Murali, Y. Zhu, X. Zhu, and R. S. Ruoff, "Using coin cells for ultracapacitor electrode material testing," *Journal of Applied Electrochemistry*, 2011.

[81] Awitdrus, M. Deraman, I. A. Talib, R. Farma, R. Omar, M. M. Ishak, N. H. Basri, and B. N. Dolah, "Effect of compression pressure on the physical and electrochemical properties of activated carbon monoliths electrodes for supercapacitor application," in *Advanced Materials Research*, 2012.

[82] G. Gourdin, A. Meehan, T. Jiang, P. Smith, and D. Qu, "Investigation of the impact of stacking pressure on a double-layer supercapacitor," *Journal of Power Sources*, 2011.

[83] M. D. Stoller and R. S. Ruoff, "Best practice methods for determining an electrode material's performance for ultracapacitors," 2010.

[84] J. Sánchez-González, A. MacÍas-García, M. F. Alexandre-Franco, and V. Gómez-Serrano, "Electrical conductivity of carbon blacks under compression," *Carbon*, 2005.

[85] Z. Niu, W. Zhou, X. Chen, J. Chen, and S. Xie, "Highly Compressible and All-Solid-State Supercapacitors Based on Nanostructured Composite Sponge," *Advanced Materials*, 2015.

[86] Y. Bu, T. Sun, Y. Cai, L. Du, O. Zhuo, L. Yang, Q. Wu, X. Wang, and Z. Hu, "Compressing Carbon Nanocages by Capillarity for Optimizing Porous Structures toward Ultrahigh-Volumetric-Performance Supercapacitors," *Advanced Materials*, 2017.

[87] X. Yang, K. Shi, I. Zhitomirsky, and E. D. Cranston, "Cellulose Nanocrystal Aerogels as Universal 3D Lightweight Substrates for Supercapacitor Materials," *Advanced Materials*, 2015.

[88] J. Yang, X. Ji, L. Liu, Y. Xiang, and Y. Zhu, "One step fabrication of graphene/polypyrrole/Ag composite electrode towards compressible supercapacitor," *Journal of Alloys and Compounds*, 2020.

[89] Q. Wang, Z. G. Qu, Z. Y. Jiang, and W. W. Yang, "Experimental study on the performance of a vanadium redox flow battery with non-uniformly compressed carbon felt electrode," *Applied Energy*, 2018.

[90] P. C. Ghimire, A. Bhattarai, R. Schweiss, G. G. Scherer, N. Wai, and Q. Yan, "A comprehensive study of electrode compression effects in all vanadium redox flow batteries including locally resolved measurements," *Applied Energy*, 2018.

[91] Y. Huang, M. Zhong, F. Shi, X. Liu, Z. Tang, Y. Wang, Y. Huang, H. Hou, X. Xie, and C. Zhi, "An Intrinsically Stretchable and Compressible Supercapacitor Containing a Polyacrylamide Hydrogel Electrolyte," *Angewandte Chemie - International Edition*, 2017.

[92] E. H. Lahrar, A. Belhboub, P. Simon, and C. Merlet, "Ionic liquids under confinement: From systematic variations of the ion and pore sizes towards an understanding of structure and dynamics in complex porous carbons," 2020.

[93] J. P. A. Santos, M. J. Pinzón, Érick A. Santos, R. Vicentini, C. J. Pagan, L. M. Da Silva, and H. Zanin, "Boosting energy-storage capability in carbon-based supercapacitors using low-temperature water-in-salt electrolytes," *Journal of Energy Chemistry*, vol. 70, pp. 521–530, 2022. [Online]. Available: https://www.sciencedirect.com/science/article/pii/S2095495622001243

[94] O. Bohlen, J. Kowal, and D. U. Sauer, "Ageing behaviour of electrochemical double layer capacitors. Part I. Experimental study and ageing model," *Journal of Power Sources*, 2007.

[95] H. El Brouji, O. Briat, J. M. Vinassa, H. Henry, and E. Woirgard, "Analysis of the dynamic behavior changes of supercapacitors during calendar life test under several voltages and temperatures conditions," *Microelectronics Reliability*, 2009.

[96] D. Placko, *Fundamentals of Instrumentation and Measurement.* Wiley, 2010.

[97] ISO 5725-2, "Accuracy (trueness and precision) of measurement methods and results - Part 1: General principles and definitions," 1994.

[98] D. T. Comer and D. J. Comer, "Analog-Signal Electronic Circuits," in *Encyclopedia of Physical Science and Technology*, 2003.

[99] Adam Carlson, "What is the Difference Between Accuracy, Precision, and Resolution?" 2020. [Online]. Available: https://control.com/technical-articles/what-is-the-difference-between-accuracy-precision-and-resolution/

[100] J. G. Webster, *The Measurement, Instrumentation and Sensors Handbook.* CRC Press, 1998.

[101] G. N. Meloni, "Building a microcontroller based potentiostat: A inexpensive and versatile platform for teaching electrochemistry and instrumentation," *Journal of Chemical Education*, 2016.

[102] M. M. Ahmadi and G. A. Jullien, "A wireless-implantable microsystem for continuous blood glucose monitoring," *IEEE Transactions on Biomedical Circuits and Systems*, 2009.

[103] V. Bianchi, A. Boni, S. Fortunati, M. Giannetto, M. Careri, and I. De Munari, "A Wi-Fi Cloud-Based Portable Potentiostat for Electrochemical Biosensors," *IEEE Transactions on Instrumentation and Measurement*, 2020.

[104] T. Arevalo-Ramirez, C. C. Torres, A. C. Rosero, and P. Espinoza-Montero, "Low cost potentiostat: Criteria and considerations for its design and construction," in *Proceedings of the 2016 IEEE ANDESCON, ANDESCON 2016*, 2017.

[105] G. Instruments, "Understanding the Specifications of your Potentiostat," 2021. [Online]. Available: https://www.gamry.com/application-notes/instrumentation/understanding-specs-of-potentiostat/

[106] A. Ainla, M. P. Mousavi, M. N. Tsaloglou, J. Redston, J. G. Bell, M. T. Fernández-Abedul, and G. M. Whitesides, "Open-Source Potentiostat for Wireless Electrochemical Detection with Smartphones," *Analytical Chemistry*, 2018.

[107] H. W. Ott, *Electromagnetic Compatibility Engineering.* Wiley, 2009.

[108] C. R. Paul, *Introduction to Electromagnetic Compatibility: Second Edition.* Wiley, 2006.

[109] B. Freitas, W. G. Nunes, D. M. Soares, F. C. Rufino, C. M. Moreira, L. M. Da Silva, and H. Zanin, "Robust, flexible, freestanding and high surface area activated carbon and multi-walled carbon nanotubes composite material with outstanding electrode properties for aqueous-based supercapacitors," *Materials Advances*, 2021.

[110] R. G. Compton, C. Batchelor-McAuley, and E. J. F. Dickinson, "Voltammetry: Understanding Problems and Solutions," in *Electroanalytical Methods.* Imperial College Press, 2007.

[111] R. G. Compton, E. Laborda, and K. R. Ward, *Understanding voltammetry: Simulation of electrode processes.* Imperial College Press, 2013.

[112] K. Y. Chan, B. Jia, H. Lin, N. Hameed, J. H. Lee, and K. T. Lau, "A critical review on multifunctional composites as structural capacitors for energy storage," 2018.

[113] M. H. Hamsan, M. F. Shukur, S. B. Aziz, Y. M. Yusof, and M. F. Kadir, "Influence of NH 4 Br as an ionic source on the structural/electrical properties of dextran-based biopolymer electrolytes and EDLC application," *Bulletin of Materials Science*, 2020.

[114] J. Ding, W. Hu, E. Paek, and D. Mitlin, "Review of Hybrid Ion Capacitors: From Aqueous to Lithium to Sodium," 2018.

[115] A. Pendashteh, M. S. Rahmanifar, R. B. Kaner, and M. F. Mousavi, "Facile synthesis of nanostructured CuCo2O4 as a novel electrode material for high-rate supercapacitors," *Chemical Communications*, 2014.

[116] B. Anasori, M. R. Lukatskaya, and Y. Gogotsi, "2D metal carbides and nitrides (MXenes) for energy storage," 2017.

[117] H. Wang, H. S. Casalongue, Y. Liang, and H. Dai, "Ni(OH)2 nanoplates grown on graphene as advanced electrochemical pseudocapacitor materials," *Journal of the American Chemical Society*, 2010.

[118] H. Xiao, S. Yao, H. Liu, F. Qu, X. Zhang, and X. Wu, "NiO nanosheet assembles for supercapacitor electrode materials," *Progress in Natural Science: Materials International*, 2016.

[119] Y. Lim, J. Yoon, J. Yun, D. Kim, S. Y. Hong, S. J. Lee, G. Zi, and J. S. Ha, "Biaxially stretchable, integrated array of high performance microsupercapacitors," *ACS Nano*, 2014.

[120] C. qi YI, J. peng ZOU, H. zhi YANG, and X. LENG, "Recent advances in pseudocapacitor electrode materials: Transition metal oxides and nitrides," *Transactions of Nonferrous Metals Society of China (English Edition)*, 2018.

[121] R. Chen, M. Yu, R. P. Sahu, I. K. Puri, and I. Zhitomirsky, "The Development of Pseudocapacitor Electrodes and Devices with High Active Mass Loading," 2020.

[122] A. Afif, S. M. Rahman, A. Tasfiah Azad, J. Zaini, M. A. Islam, and A. K. Azad, "Advanced materials and technologies for hybrid supercapacitors for energy storage – A review," 2019.

[123] T. Christen and M. W. Carlen, "Theory of ragone plots," *Journal of Power Sources*, 2000.

[124] W. G. Pell and B. E. Conway, “Quantitative modeling of factors determining Ragone plots for batteries and electrochemical capacitors,” *Journal of Power Sources*, 1996.

[125] N. Reichbach, M. Mellincovsky, M. M. Peretz, and A. Kuperman, “Long-term wide-temperature supercapacitor ragone plot based on manufacturer datasheet,” *IEEE Transactions on Energy Conversion*, 2016.

[126] R. Vicentini, J. P. Aguiar, R. Beraldo, R. Venâncio, F. Rufino, L. M. Da Silva, and H. Zanin, “Ragone Plots for Electrochemical Double-Layer Capacitors,” *Batteries and Supercaps*, 2021.

[127] E. P. Achterberg, “Laboratory techniques in electroanalytical chemistry,” *TrAC Trends in Analytical Chemistry*, 1996.

[128] Allen J. Bard and L. R. Faulkner, *Electrochemical Methods: Fundamentals and Applications*, 2nd ed. Wiley, 2001.

[129] C. G. Zoski, *Handbook of electrochemistry.* Elsevier Science, 2007.

[130] D. Pletcher, R. Greff, R. Peat, L. M. Peter, and J. Robinson, *Instrumental methods in electrochemistry.* Woodhead Publishing, 2001.

[131] A. Lewandowski, P. Jakobczyk, M. Galinski, and M. Biegun, “Self-discharge of electrochemical double layer capacitors,” *Physical Chemistry Chemical Physics*, 2013.

[132] V. Sunil, B. Pal, I. Izwan Misnon, and R. Jose, “Characterization of supercapacitive charge storage device using electrochemical impedance spectroscopy,” in *Materials Today: Proceedings*, 2020.

[133] B. A. Mei, O. Munteshari, J. Lau, B. Dunn, and L. Pilon, “Physical Interpretations of Nyquist Plots for EDLC Electrodes and Devices,” *Journal of Physical Chemistry C*, 2018.

[134] V. F. Lvovich, *Impedance spectroscopy: Applications to electrochemical and dielectric phenomena.* Wiley, 2015.

[135] E. Barsoukov and J. R. Macdonald, *Impedance Spectroscopy: Theory, Experiment, and Applications.* Wiley, 2005.

[136] A. R. Bredar, A. L. Chown, A. R. Burton, and B. H. Farnum, “Electrochemical Impedance Spectroscopy of Metal Oxide Electrodes for Energy Applications,” 2020.

[137] F. Ciucci, “Modeling electrochemical impedance spectroscopy,” 2019.

[138] H. Krienke, “Modern Aspects of Electrochemistry, No. 31,” *Zeitschrift für Physikalische Chemie*, 1999.

[139] N. Xu and D. J. Riley, “Nonlinear analysis of a classical system: The Faradaic process,” *Electrochimica Acta*, 2013.

[140] R. Pollard and T. Comte, “Determination of Transport Properties for Solid Electrolytes from the Impedance of Thin Layer Cells,” *Journal of The Electrochemical Society*, 1989.

[141] S. M. Park, J. S. Yoo, B. Y. Chang, and E. S. Ahn, “Novel instrumentation in electrochemical impedance spectroscopy and a full description of an electrochemical system,” in *Pure and Applied Chemistry*, 2006.

[142] A. Hammar, P. Venet, R. Lallemand, G. Coquery, and G. Rojat, “Study of accelerated aging of supercapacitors for transport applications,” *IEEE Transactions on Industrial Electronics*, 2010.

[143] C. Maton, N. De Vos, and C. V. Stevens, “Ionic liquid thermal stabilities: Decomposition mechanisms and analysis tools,” *Chemical Society Reviews*, 2013.

[144] B. Shen, R. Guo, J. Lang, L. Liu, L. Liu, and X. Yan, “A high-temperature flexible supercapacitor based on pseudocapacitive behavior of FeOOH in an ionic liquid electrolyte,” *Journal of Materials Chemistry A*, 2016.

[145] C. Masarapu, H. F. Zeng, K. H. Hung, and B. Wei, “Effect of temperature on the capacitance of carbon nanotube supercapacitors,” *ACS Nano*, 2009.

[146] K. Hung, C. Masarapu, T. Ko, and B. Wei, “Wide-temperature range operation supercapacitors from nanostructured activated carbon fabric,” *Journal of Power Sources*, 2009.

[147] C. Yuan, X. Zhang, Q. Wu, and B. Gao, “Effect of temperature on the hybrid supercapacitor based on NiO and activated carbon with alkaline polymer gel electrolyte,” *Solid State Ionics*, 2006.

[148] Q. Abbas, D. Pajak, E. Frackowiak, and F. Béguin, “Effect of binder on the performance of carbon/carbon symmetric capacitors in salt aqueous electrolyte,” *Electrochimica Acta*, 2014.

[149] L. Khezami, A. Ould-Dris, and R. Capart, “Activated carbon from thermo-compressed wood and other lignocellulosic precursors,” *BioResources*, 2007.

[150] P. Ramirez-Vidal, R. L. Canevesi, G. Sdanghi, S. Schaefer, G. Maranzana, A. Celzard, and V. Fierro, “A Step Forward in Understanding the Hydrogen Adsorption and Compression on Activated Carbons,” *ACS Applied Materials and Interfaces*, 2021.

[151] L. Chen, T. Watanabe, H. Kanoh, K. Hata, and T. Ohba, “Cooperative CO2 adsorption promotes high CO2 adsorption density over wide optimal nanopore range,” *Adsorption Science and Technology*, 2018.

[152] P. Y. Yang, S. P. Ju, and S. M. Huang, “Predicted structural and mechanical properties of activated carbon by molecular simulation,” *Computational Materials Science*, 2018.

[153] X. Xu, J. Yang, X. Zhou, S. Jiang, W. Chen, and Z. Liu, “Highly crumpled graphene-like material as compression-resistant electrode material for high energy-power density supercapacitor,” *Chemical Engineering Journal*, 2020.

[154] X. Li and B. Wei, “Supercapacitors based on nanostructured carbon,” 2013.

[155] M. Antonietti, X. Chen, R. Yan, and M. Oschatz, “Storing electricity as chemical energy: Beyond traditional electrochemistry and double-layer compression,” *Energy and Environmental Science*, 2018.

[156] A. C. Forse, J. M. Griffin, C. Merlet, J. Carretero-Gonzalez, A. R. O. Raji, N. M. Trease, and C. P. Grey, “Direct observation of ion dynamics in supercapacitor electrodes using in situ diffusion NMR spectroscopy,” *Nature Energy*, 2017.

[157] A. C. Forse, C. Merlet, J. M. Griffin, and C. P. Grey, “New perspectives on the charging mechanisms of supercapacitors,” *Journal of the American Chemical Society*, 2016.

[158] K. Xu, C. Merlet, Z. Lin, H. Shao, P. L. Taberna, L. Miao, J. Jiang, J. Zhu, and P. Simon, “Effects of functional groups and anion size on the charging mechanisms in layered electrode materials,” *Energy Storage Materials*, 2020.

[159] F. Wang, X. Wu, X. Yuan, Z. Liu, Y. Zhang, L. Fu, Y. Zhu, Q. Zhou, Y. Wu, and W. Huang, “Latest advances in supercapacitors: From new electrode materials to novel device designs,” 2017.

[160] P. Simon and Y. Gogotsi, “Perspectives for electrochemical capacitors and related devices,” 2020.

[161] S. G. Lee, D. H. Jeon, B. M. Kim, J. H. Kang, and C.-J. Kim, “Lattice Boltzmann Simulation for Electrolyte Transport in Porous Electrode of Lithium Ion Batteries,” *Journal of The Electrochemical Society*, 2013.

[162] D. H. Jeon, “Wettability in electrodes and its impact on the performance of lithium-ion batteries,” *Energy Storage Materials*, 2019.

[163] S. G. Lee and D. H. Jeon, “Effect of electrode compression on the wettability of lithium-ion batteries,” *Journal of Power Sources*, 2014.

[164] Y. Marcus, "Thermodynamics of solvation of ions. Part 5. - Gibbs free energy of hydration at 298.15 K," *Journal of the Chemical Society, Faraday Transactions*, 1991.

[165] C. Largeot, C. Portet, J. Chmiola, P. L. Taberna, Y. Gogotsi, and P. Simon, "Relation between the ion size and pore size for an electric double-layer capacitor," *Journal of the American Chemical Society*, 2008.

[166] G. Feng and P. T. Cummings, "Supercapacitor capacitance exhibits oscillatory behavior as a function of nanopore size," *Journal of Physical Chemistry Letters*, 2011.

[167] D. E. Jiang, Z. Jin, and J. Wu, "Oscillation of capacitance inside nanopores," *Nano Letters*, 2011.

[168] G. Feng, R. Qiao, J. Huang, B. G. Sumpter, and V. Meunier, "Atomistic insight on the charging energetics in subnanometer pore supercapacitors," *Journal of Physical Chemistry C*, 2010.

[169] S. Kondrat, N. Georgi, M. V. Fedorov, and A. A. Kornyshev, "A superionic state in nano-porous double-layer capacitors: Insights from Monte Carlo simulations," in *Physical Chemistry Chemical Physics*, 2011.

[170] S. Kondrat and A. Kornyshev, "Corrigendum: Superionic state in double-layer capacitors with nanoporous electrodes," *Journal of Physics: Condensed Matter*, 2013.

[171] Y. Yu, B. Xiong, F. Zeng, R. Xu, F. Yang, J. Kang, M. Xiang, L. Li, X. Sheng, and Z. Hao, "Influences of Compression on the Mechanical Behavior and Electrochemical Performances of Separators for Lithium Ion Batteries," *Industrial and Engineering Chemistry Research*, 2018.

[172] L. Ding, C. Zhang, T. Wu, F. Yang, Y. Cao, and M. Xiang, "The compression behavior, microstructure evolution and properties variation of three kinds of commercial battery separators under compression load," *Journal of Power Sources*, 2020.

[173] Y. Wang, Q. M. Li, and Y. Xing, "Porosity variation of lithium-ion battery separators under uniaxial tension," *International Journal of Mechanical Sciences*, 2020.

[174] R. Vicentini, L. M. Da Silva, E. P. Cecilio, T. A. Alves, W. G. Nunes, and H. Zanin, "How to measure and calculate equivalent series resistance of electric double-layer capacitors," *Molecules*, 2019.

[175] N. S. Nor, M. Deraman, M. Suleman, M. R. Jasni, J. G. Manjunatha, M. A. Othman, and S. A. Shamsudin, "Supercapacitors using binderless activated carbon monoliths

electrodes consisting of a graphite additive and pre-carbonized biomass fibers," *International Journal of Electrochemical Science*, 2017.

[176] X. Yang, J. Lee, L. Yuan, S. R. Chae, V. K. Peterson, A. I. Minett, Y. Yin, and A. T. Harris, "Removal of natural organic matter in water using functionalised carbon nanotube buckypaper," *Carbon*, 2013.

[177] R. Parsons, "Surface electrochemistry, a molecular level approach," *Journal of Electroanalytical Chemistry*, 1994.

[178] K. Fic, M. He, E. J. Berg, P. Novák, and E. Frackowiak, "Comparative operando study of degradation mechanisms in carbon-based electrochemical capacitors with Li2SO4 and LiNO3 electrolytes," *Carbon*, 2017.

[179] R. A. Robinson and R. H. Stokes, *Electrolyte Solutions: Second Revised Edition.* Courier Corporation, 2002.

[180] J. O. Bockris and A. K. N. Reddy, *Modern Electrochemistry 1*, 2nd ed. Kluwer Academic Publishers, 1999.

[181] J. Koryta, J. Dvorak, and A. M. Bond, *Principles of Electrochemistry.* New York: Wiley, 1987.

[182] Y. Shao, J. Li, Y. Li, H. Wang, Q. Zhang, and R. B. Kaner, "Flexible quasi-solid-state planar micro-supercapacitor based on cellular graphene films," *Materials Horizons*, vol. 4, no. 6, pp. 1145–1150, 2017.

[183] T. Papanastasiou, G. Georgiou, and A. Alexandrou, *Viscous Fluid Flow.* McGraw-Hill Higher Education, 1999.

[184] B. Michalak, H. Sommer, D. Mannes, A. Kaestner, T. Brezesinski, and J. Janek, "Gas Evolution in Operating Lithium-Ion Batteries Studied in Situ by Neutron Imaging," *Scientific Reports*, 2015.

[185] Q. D. Nguyen, Y. H. Wu, T. Y. Wu, M. J. Deng, C. H. Yang, and J. K. Chang, "Gravimetric/volumetric capacitances, leakage current, and gas evolution of activated carbon supercapacitors," *Electrochimica Acta*, 2016.

[186] B. E. Conway, V. Birss, and J. Wojtowicz, "The role and utilization of pseudocapacitance for energy storage by supercapacitors," *Journal of Power Sources*, 1997.

[187] B. V. Tilak, C. P. Chen, and S. K. Rangarajan, "A model to characterize the impedance of electrochemical capacitors arising from reactions of the type Oad + n e- {leftwards paired arrows} Rad," *Journal of Electroanalytical Chemistry*, 1992.

[188] S. Sarangapani, B. V. Tilak, and C. Chen, “Materials for Electrochemical Capacitors: Theoretical and Experimental Constraints,” *Journal of The Electrochemical Society*, 1996.

[189] A. J. Roberts, A. F. De Namor, and R. C. Slade, “Low temperature water based electrolytes for MnO2/carbon supercapacitors,” *Physical Chemistry Chemical Physics*, 2013.

[190] A. Bhide, J. Hofmann, A. Katharina Dürr, J. Janek, and P. Adelhelm, “Electrochemical stability of non-aqueous electrolytes for sodium-ion batteries and their compatibility with Na0.7CoO2,” *Physical Chemistry Chemical Physics*, 2014.

[191] R. Kötz, P. W. Ruch, and D. Cericola, “Aging and failure mode of electrochemical double layer capacitors during accelerated constant load tests,” *Journal of Power Sources*, 2010.

[192] J. Menzel, E. Frackowiak, and K. Fic, “Electrochemical capacitor with water-based electrolyte operating at wide temperature range,” *Journal of Power Sources*, 2019.

[193] G. Xiong, A. Kundu, and T. S. Fisher, *Thermal Effects in Supercapacitors.* Springer, 2015.

[194] P. J. Larkin, *Infrared and Raman Spectroscopy: Principles and Spectral Interpretation.* Elsevier Inc, 2017.

[195] A. G. Miller and J. W. Macklin, “Vibrational spectroscopic studies of sodium perchlorate contact ion pair formation in aqueous solution,” *Journal of Physical Chemistry*, 1985.

[196] I. Durickovic, “Using Raman Spectroscopy for Characterization of Aqueous Media and Quantification of Species in Aqueous Solution,” in *Applications of Molecular Spectroscopy to Current Research in the Chemical and Biological Sciences*, 2016.

[197] G. E. Walrafen, “Raman spectral studies of the effects of temperature on water and electrolyte solutions,” *The Journal of Chemical Physics*, 1966.

Appendix

APPENDIX A – Morphological Structure of the Electrodes and Adsorption/Desorption Isotherms for MWCNT.

Here, it is possible to see the morphological structure of the MWCNTs electrode and the nitrogen adsorption/desorption isotherms for MWCNT.

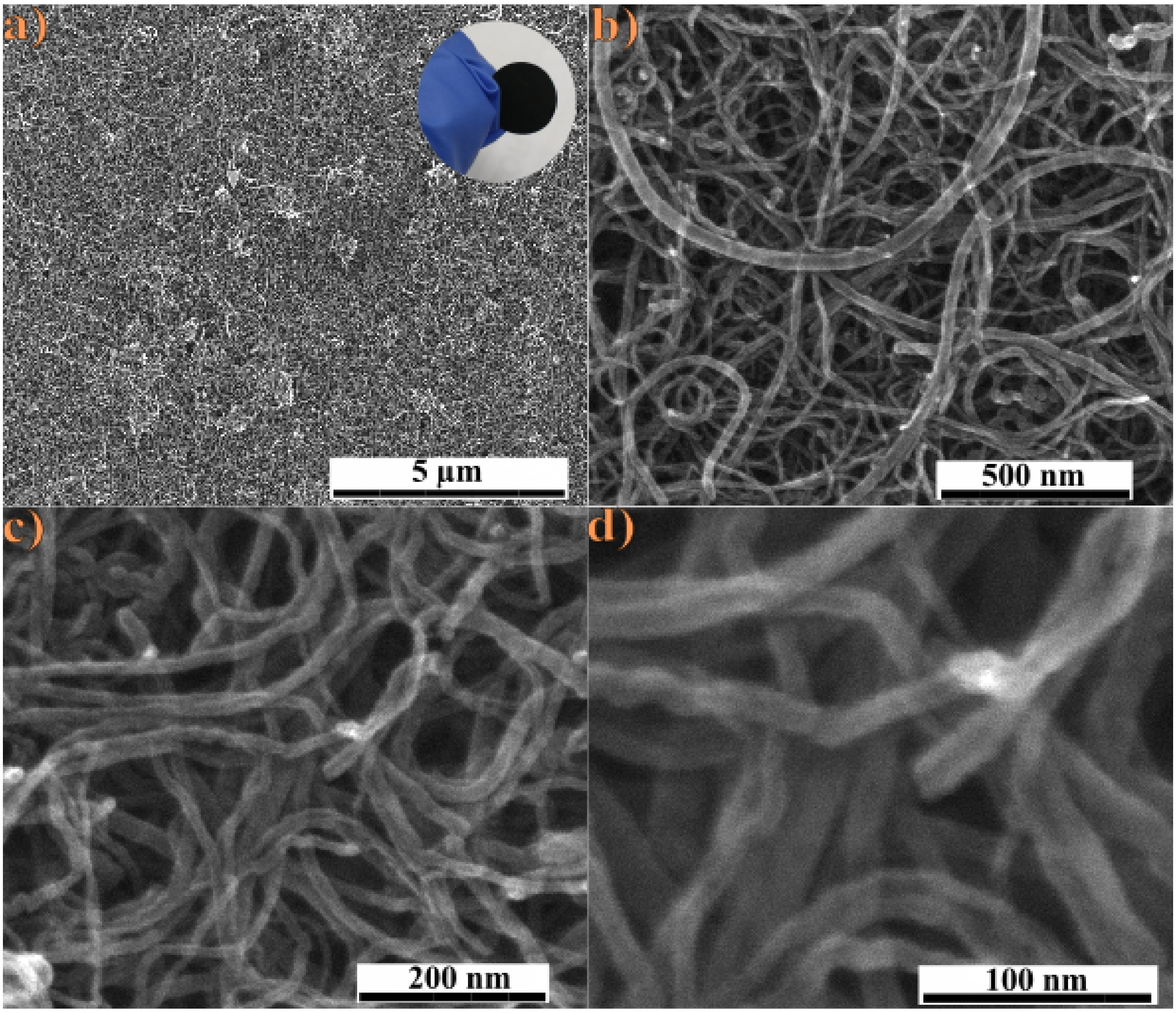

Figure A.1 – Scanning electron micrographs from the buckypaper electrodes composed of multi-walled carbon nanotubes at different magnifications.

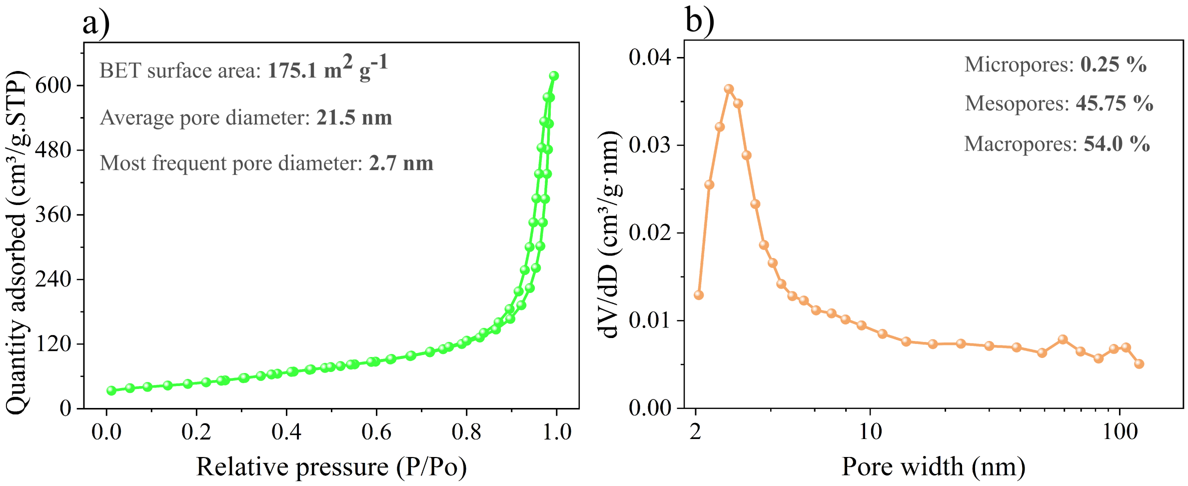

Figure A.2 – Nitrogen adsorption/desorption isotherms for multi-walled carbon nanotubes. (a) Isotherm linear plot. (b) Adsorption Pore Size Distribution Plot (dV/dD).

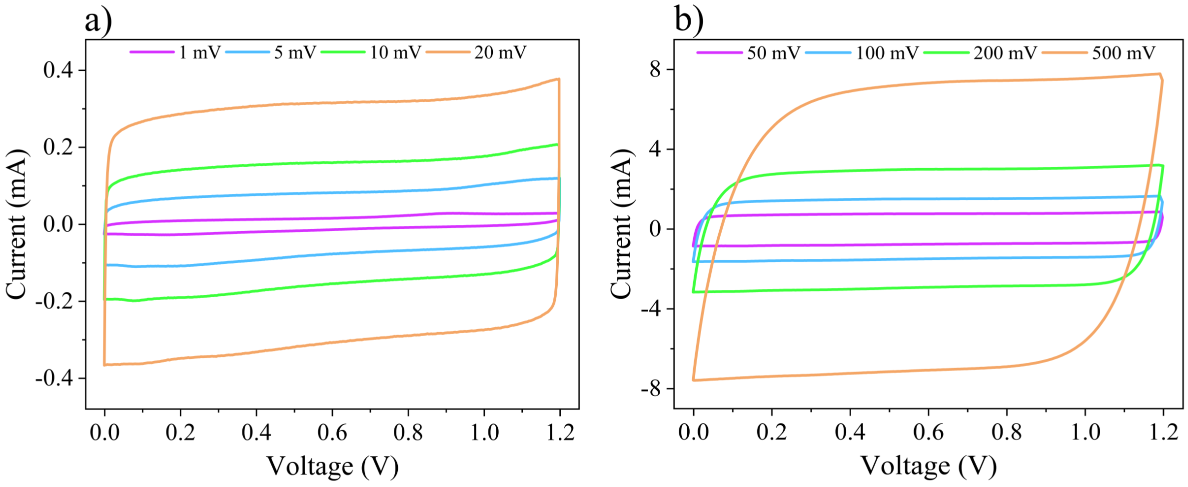

Figure A.3 – CV curves at various scan rates. (a) Curves from 1 to 20 mV s $^{-1}$ (b) Curves from 50 to 500 mV $^{-1}$

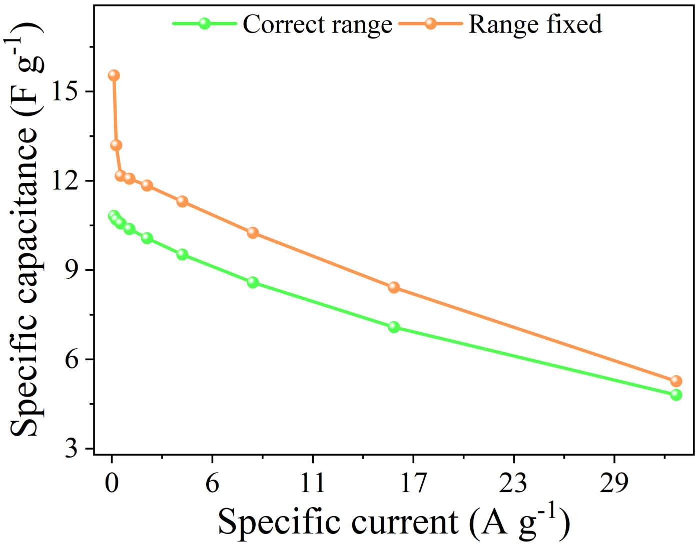

Figure A.4 – The rate capability at various current densities and 1.2 of working voltage window.

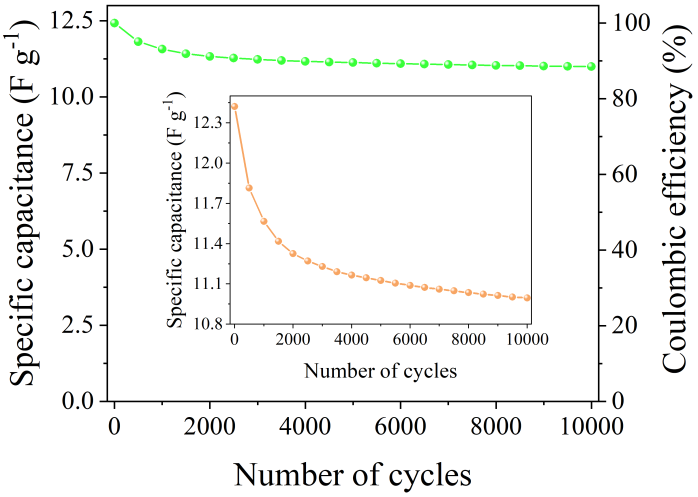

Figure A.5 – Cycling performance and coulombic efficiency of the system at 4 A g^{-1} and 1.2 V.

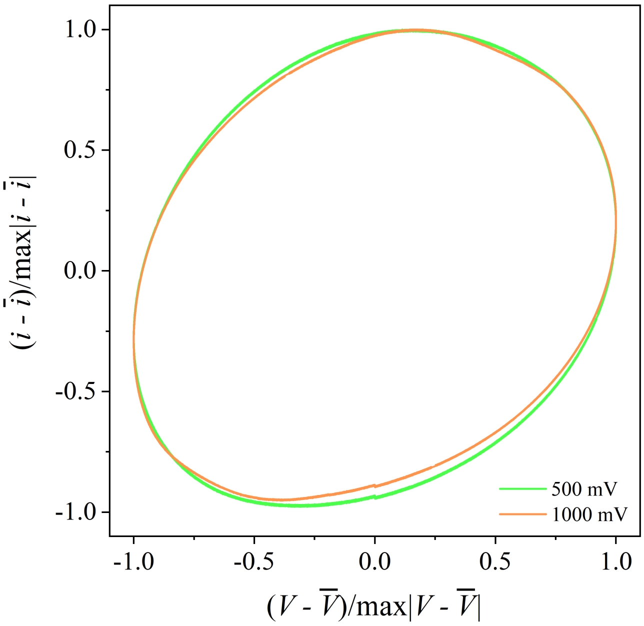

Figure A.6 – Lissajous representation of a signal at 100 mHz, open-circuit voltage, and sinusoidal potential scan of 500 mV and 1000 mV.

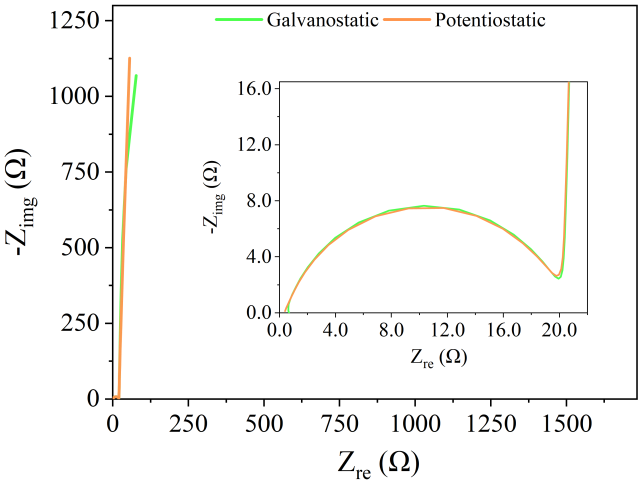

Figure A.7 – EIS measurements at the potentiostatic and galvanostatic mode. Both modes were configurated in the range from 100 kHz to 10 mHz and a steady voltage and current equal to zero. The sinusoidal current in galvanostatic mode was set with 1 mA, and for the potenciostatic mode, 10 mV.

APPENDIX B – Electrochemical Measurements from Compressed Electrodes at 100 PSI

Here, different electrochemical measures are presented. The results are based on the SCs compressed at 100 PSI after the devices have been compressed until 260 PSI.

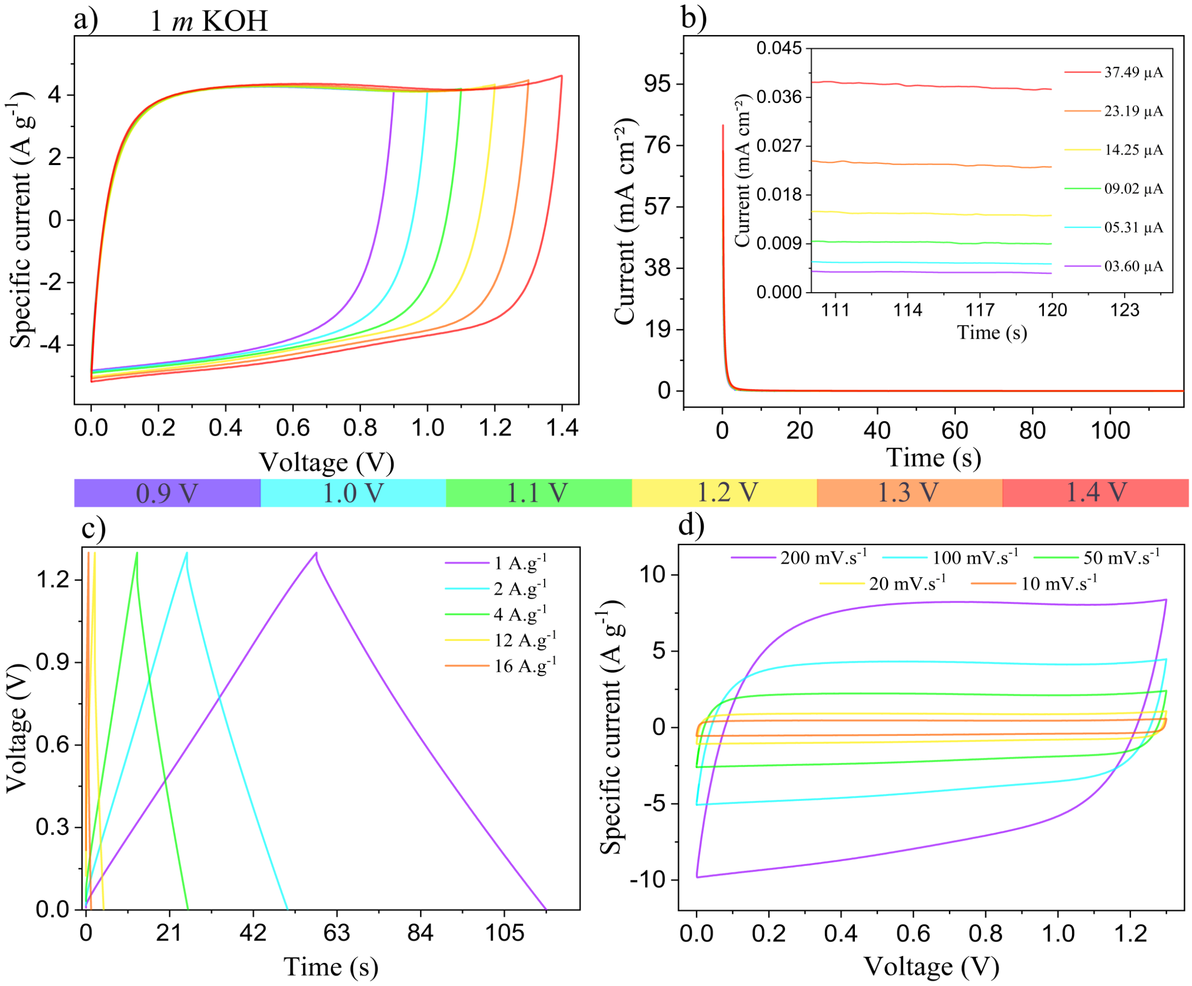

Figure B.1 – Electrochemical measures from 1 molar of KOH electrolyte under 100 PSI of compression. (a) Cyclic voltammetry curves at a scan rate of 100 mV s^{-1}, and (b) chronoamperometry measures of 2 minutes constant voltage for various applied voltage levels. (c) galvanostatic charge-discharge profiles at 1.3 V, and (d) Cyclic voltammetry curves at various scan rates from 10 to 200 mV s^{-1}.

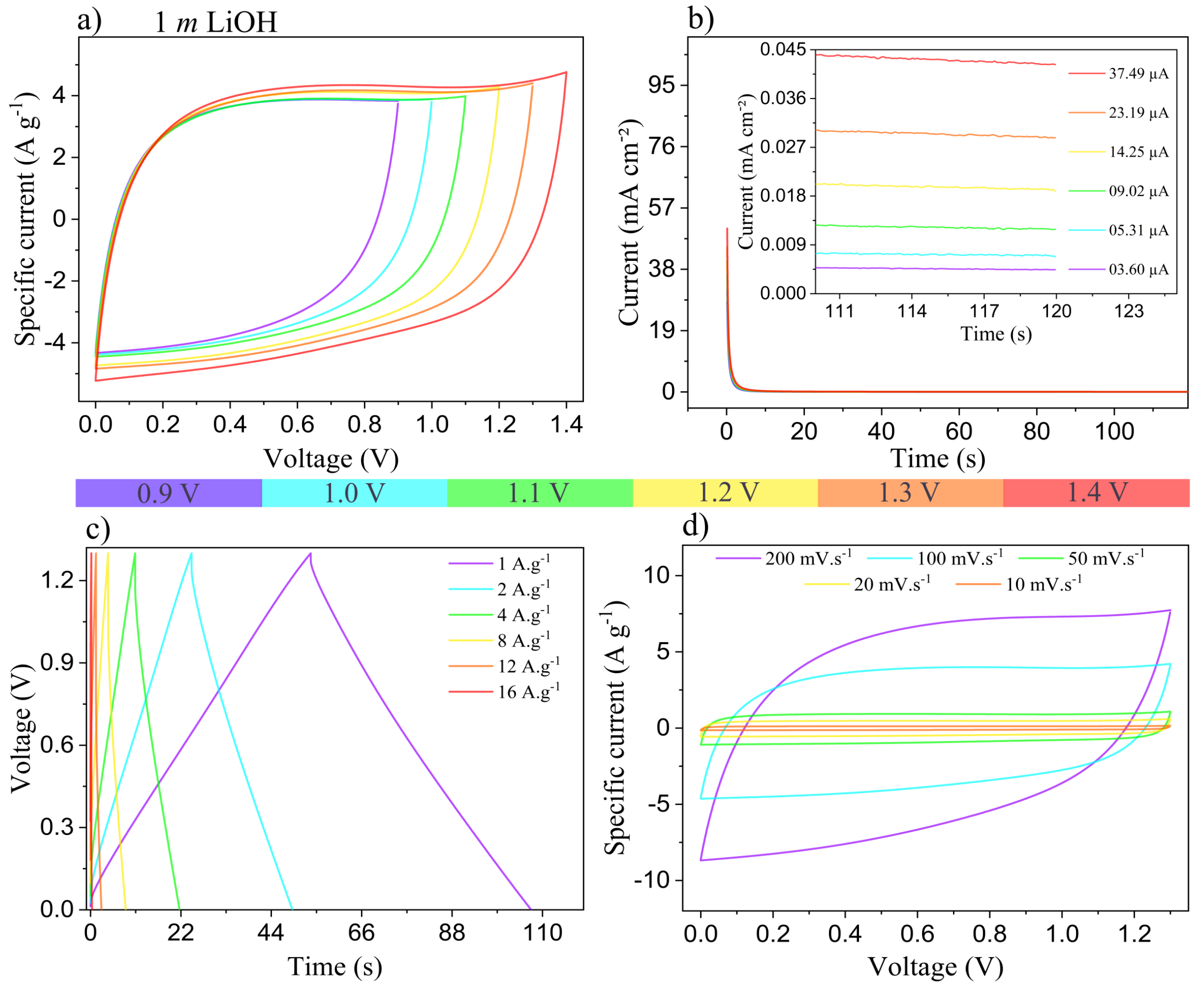

Figure B.2 – Electrochemical measures from 1 molar of LiOH electrolyte under 100 PSI of compression. (a) Cyclic voltammetry curves at a scan rate of 100 mV s^{-1}, and (b) chronoamperometry measures of 2 minutes constant voltage for various applied voltage levels. (c) galvanostatic charge-discharge profiles at 1.3 V, and (d) Cyclic voltammetry curves at various scan rates from 10 to 200 mV s^{-1}.

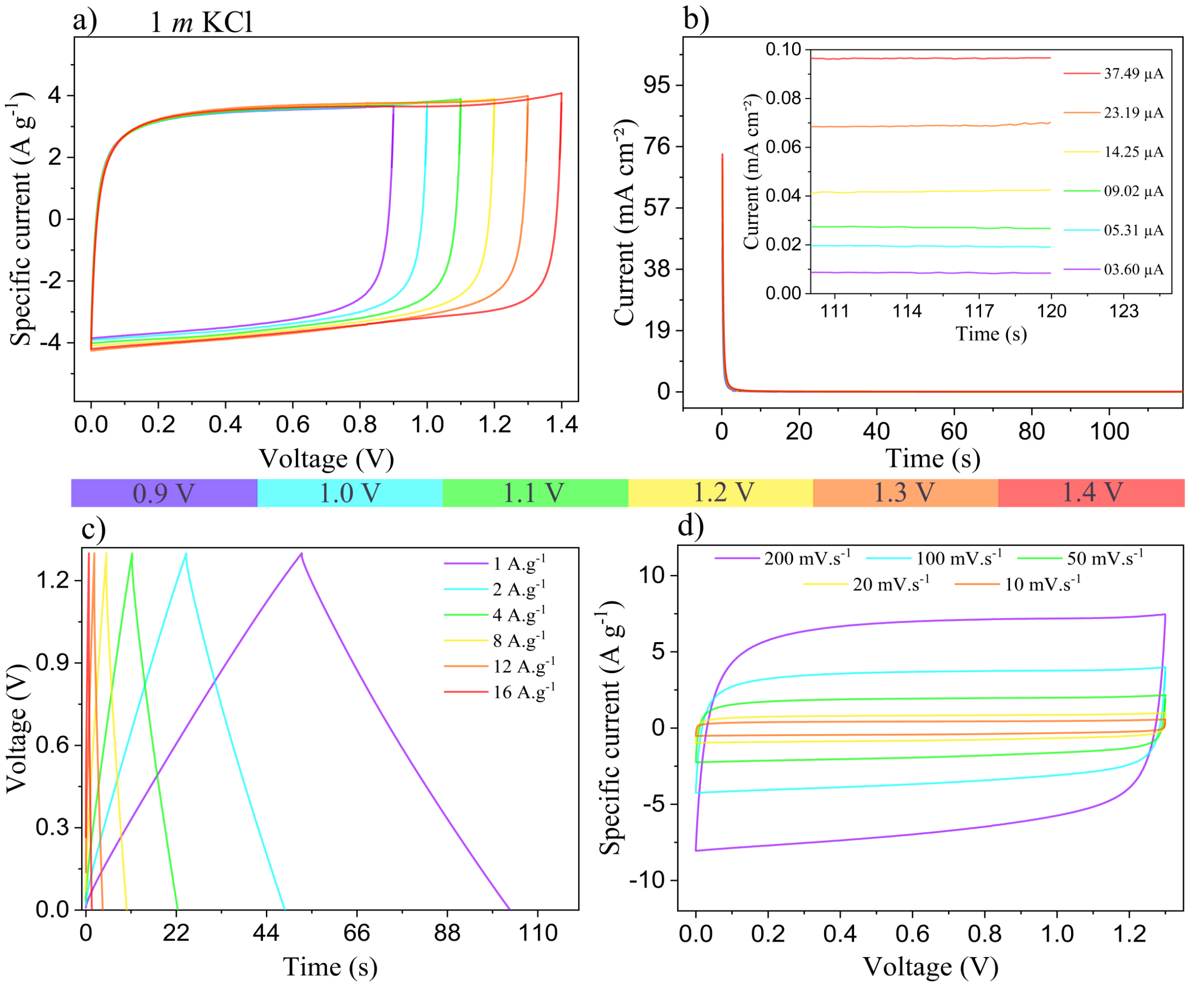

Figure B.3 – Electrochemical measures from 1 molar of KCl electrolyte under 100 PSI of compression. (a) Cyclic voltammetry curves at a scan rate of 100 mV s^{-1}, and (b) chronoamperometry measures of 2 minutes constant voltage for various applied voltage levels. (c) galvanostatic charge-discharge profiles at 1.3 V, and (d) Cyclic voltammetry curves at various scan rates from 10 to 200 mV s^{-1}.

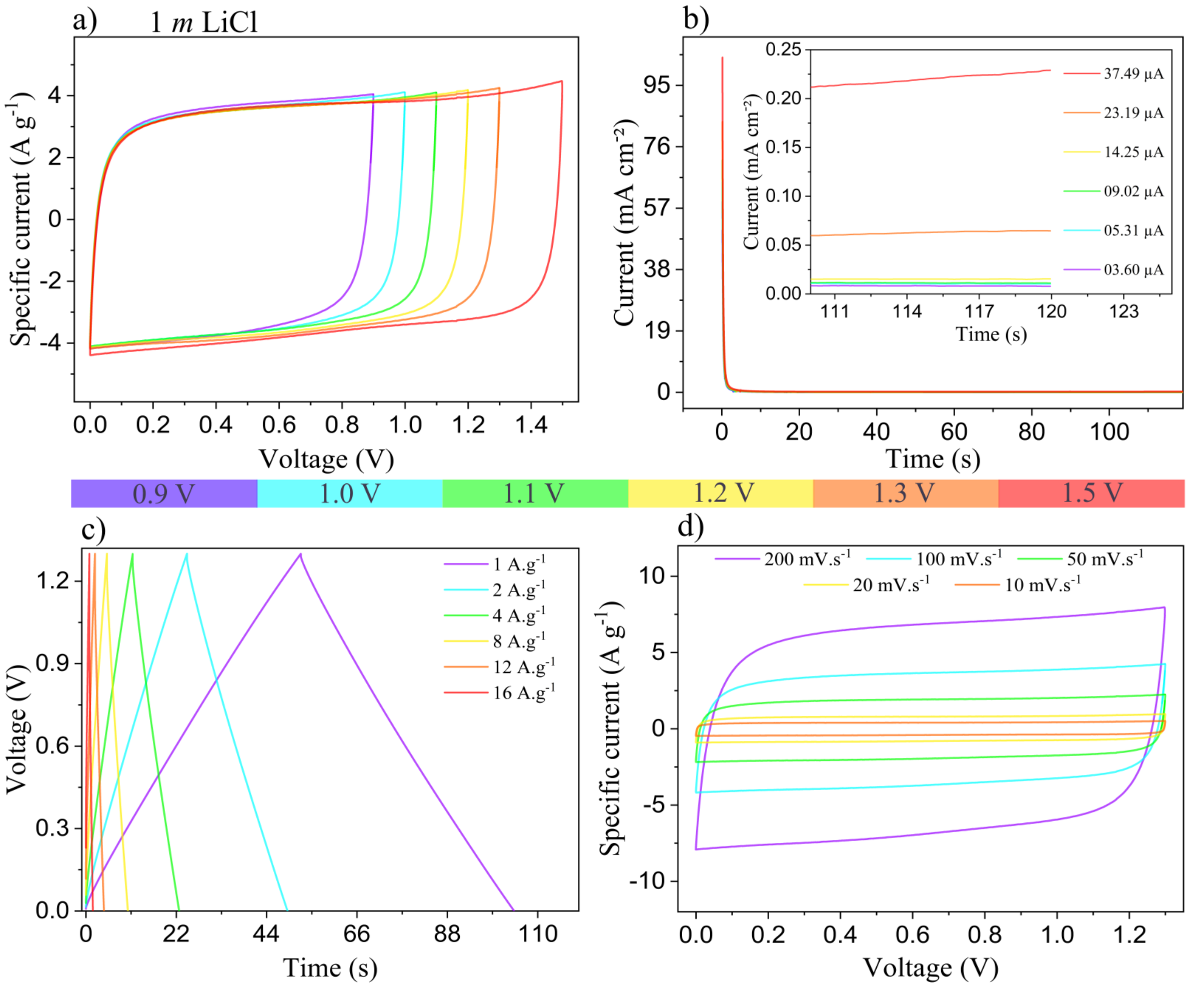

Figure B.4 – Electrochemical measures from 1 molar of LiCl electrolyte under 100 PSI of compression. (a) Cyclic voltammetry curves at a scan rate of 100 mV s^{-1}, and (b) chronoamperometry measures of 2 minutes constant voltage for various applied voltage levels. (c) galvanostatic charge-discharge profiles at 1.3 V, and (d) Cyclic voltammetry curves at various scan rates from 10 to 200 mV s^{-1}.

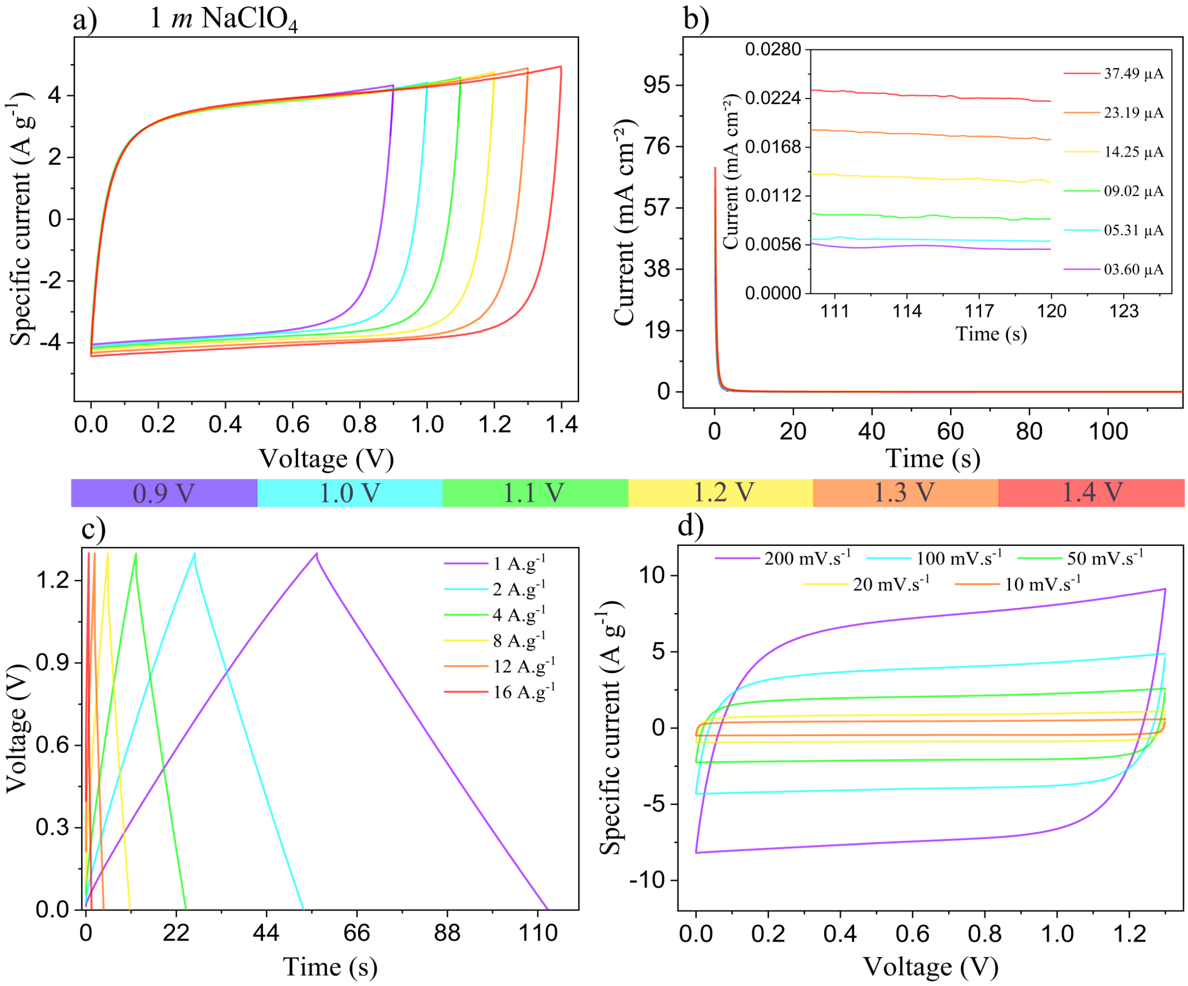

Figure B.5 – Electrochemical measures from 1 molar of $NaClO_4$ electrolyte under 100 PSI of compression. (a) Cyclic voltammetry curves at a scan rate of 100 mV s^{-1}, and (b) chronoamperometry measures of 2 minutes constant voltage for various applied voltage levels. (c) galvanostatic charge-discharge profiles at 1.3 V, and (d) Cyclic voltammetry curves at various scan rates from 10 to 200 mV s^{-1}.